

POLITECNICO DI MILANO



DEPARTMENT OF PHYSICS

DOCTORAL PROGRAMME IN PHYSICS

Investigations of Photo-excited 2D Materials by  
Combined Ultrafast Spectroscopy Techniques

Doctoral Dissertation of:  
Arianna Ceraso

Supervisor:

Dott. Ettore Carpene

Tutor:

Prof. Claudia Dallera

2018 - 2021  
XXXIV cycle

# Contents

List of Figures	iii
List of Tables	xii
Acknowledgements	xiv
Abstract	xv
Introduction	xvii
<b>1 Theoretical Background</b>	<b>1</b>
1.1 General Properties of Semiconductors . . . . .	2
1.2 Photo-induced Phenomena in Black Phosphorus . . . . .	7
1.2.1 Burstein-Moss Shift (BMS) . . . . .	7
1.2.2 Bandgap Renormalization (BGR) . . . . .	9
1.2.3 Surface Photovoltage (SPV) . . . . .	10
1.3 Charge density waves (CDWs) . . . . .	12
1.3.1 Free-electron theory of metals . . . . .	13
1.3.2 CDW in 1D: Peierls model . . . . .	14
1.3.3 CDW in higher dimensions: Fermi surface nesting . . . . .	18
1.4 Conclusions . . . . .	21
<b>2 Experimental Details</b>	<b>22</b>
2.1 General Overview . . . . .	22
2.2 Angle-Resolved Photoemission Spectroscopy (ARPES) . . . . .	23
2.2.1 Photoemission Spectroscopy . . . . .	23
2.2.2 Theory of ARPES . . . . .	25
2.2.3 Three-step Model . . . . .	28
2.2.4 Many-body concepts used in ARPES . . . . .	33
2.3 Time- and Angle-Resolved Photoemission Spectroscopy (TR-ARPES)	34
2.3.1 Experimental setup . . . . .	36
2.3.2 Other TR-ARPES experimental setups . . . . .	43

2.4	Time-Resolved Reflectivity (TRR) . . . . .	44
2.4.1	Introduction . . . . .	44
2.4.2	Experimental setup . . . . .	45
2.5	Conclusions . . . . .	46
<b>3</b>	<b>Electron Dynamics in Black Phosphorus</b>	<b>47</b>
3.1	Introduction . . . . .	47
3.2	Sample Properties . . . . .	48
3.3	TR-ARPES on Pristine BP . . . . .	49
3.4	TR-ARPES on Cs-doped BP . . . . .	53
3.4.1	Spectral Analysis and Fitting . . . . .	60
3.4.2	Electronic and Optical Properties of BP . . . . .	61
3.4.3	The Demer Potential . . . . .	63
3.5	Conclusions . . . . .	66
<b>4</b>	<b>Transition Metal Dichalcogenides</b>	<b>67</b>
4.1	A general overview . . . . .	67
4.1.1	Tantalum-based TMDs . . . . .	68
4.1.2	Preparation and characterization of 1 <i>T</i> -TaSe <sub>2</sub> single crystals . . . . .	72
4.2	Steady-State and Time-Resolved Investigations on 1 <i>T</i> -TaSe <sub>2</sub> . . . . .	75
4.2.1	Full-wavevector ARPES . . . . .	75
4.2.2	TR-ARPES and TRR on 1 <i>T</i> -TaSe <sub>2</sub> . . . . .	77
4.2.3	Temperature dependence of coherent phonons in the CDW phase . . . . .	80
4.2.4	Experimental hints of dimerization in 1 <i>T</i> -TaSe <sub>2</sub> . . . . .	82
4.2.5	DFT calculations with Quantum Espresso . . . . .	88
4.3	Conclusions . . . . .	89
	<b>Conclusion and perspectives</b>	<b>90</b>
	<b>Bibliography</b>	<b>110</b>
	<b>List of publications</b>	<b>111</b>

# List of Figures

1.1	Scheme of the density-of-states of an intrinsic semiconductor at zero temperature. The top of the VB, $E_v$ , and the bottom of the CB, $E_c$ , are separated by a bandgap energy $E_G = E_c - E_v$ . The chemical potential $\mu$ at zero temperature lies at the middle of the bandgap. . . . .	2
1.2	Fermi-Dirac distribution function $f(E)$ at different temperatures: $T = 0$ K (blue curve), $T = 300$ K (green curve) and $T = 600$ K (red curve). At zero temperature, the probability of an electron to occupy an energy level below the Fermi level $E_F$ is equal to 1, while the probability to occupy higher energy levels is equal to 0. At finite temperatures, the distribution gets smeared out because some electrons begin to be thermally excited to energy levels above the chemical potential. Note that the total number of electrons is constant and independent of temperature and that only a small fraction of the total number of electrons can be thermally excited. . . . .	4
1.3	Isotropic and parabolic two-band model semiconductor. The valence band (red) and the conduction band (blue) with the corresponding dispersion relations are shown. The valence band curve has been reported in red to remind its total occupancy by electrons at $T = 0$ K. . . . .	6
1.4	Burstein-Moss effect caused by Pauli blocking. (a) In equilibrium, VB is almost totally occupied and CB empty. By photo-excitation, electrons are promoted to conduction band-edge states, leaving behind holes in VB. (b) After thermalization, the depletion of the VB maximum and the increase of spectral weight in CB are observed. As a consequence, the bandgap enlarges to $E'_g = E_{qFC} - E_{qFV}$ , where $E_{qFC}$ and $E_{qFV}$ are the quasi-Fermi levels for CB and VB, respectively. . . . .	8

1.5	Schematic illustration of the BGR phenomenon. Before optical excitation (left panel), VB is almost fully occupied and CB empty except for the weak thermal carrier distributions; $E_F$ lies within the bandgap. Upon optical excitation (central panel), electrons are excited in the CB and holes are left behind in the VB. These high-mobility charge carriers determine a bandgap shrinkage. The initial bandgap is then restored in time (right panel). . . . .	9
1.6	Schematic diagrams of Cs-induced band bending and SPV effect, taken from Ref. [1]. (a) Surface doping by Cs atoms leads to a downward band bending; $\phi_{BB}$ : band bending potential. (b) After excitation, SPV develops and all energy levels at the surface shift upward, compensating the bending potential. $\phi_{SPV}$ : surface photovoltage. . . . .	11
1.7	Schematic illustration of the Fermi surface and of the Fermi sphere formed by occupied band states in the reciprocal space. At $T = 0$ , each state with wavevector $\mathbf{k}$ such that $k < k_F$ accomodates two electrons with opposite spin. . . . .	14
1.8	Illustration of the Peierls model for a 1D linear chain metal with a half-filled band. (a) In the normal state, the lattice constant is $a$ and the charge density $\rho(r)$ is uniform. Electrons are filled up to the Fermi level $E_F$ . (b) The electron-phonon interactions gives rise to a lattice distortion, the so-called <i>Peierls distortion</i> , leading to a periodic modulation in the charge density. As a result, a charge density wave (CDW) state forms. The opening of a gap $\Delta$ around $E_F$ in the electronic dispersion causes the total energy of the system (the sum of electronic and lattice components) to decrease. . . . .	15
1.9	Excitation of amplitude ( <i>amplitudon</i> ) and phase ( <i>phason</i> ) of a charge density wave in the $q = 0$ limit. Lines indicate changes to the charge density, while red circles are the ions. Arrows show the variations in the ion position. . . . .	18

1.10	Fermi surface nesting for a 1D, 2D and quasi-2D electron gas. (a) In 1D, the Fermi surface of free electrons is composed of two parallel sheets at $\pm k_F$ . A perfect nesting is fulfilled because the single nesting wavevector $\mathbf{q} = 2\mathbf{k}_F$ is able to span the whole Fermi surface. (b) In 2D, the Fermi surface is circular. Because of this shape, only a reduced portion of the Fermi surface is nested by $\mathbf{q}$ , leading to a poor nesting. (c) . In a quasi-2D system, the Fermi surface is elliptical, therefore large parallel portions of the Fermi surface can be nested, thus achieving a moderate nesting. The red arrows in all three cases indicate pairs of states, one occupied and one empty, differing by the wavevector $\mathbf{q} = 2\mathbf{k}_F$ . . . . .	19
1.11	Behaviour of the bare electronic susceptibility and consequential renormalization of phonon dispersion. (a) Plots of the real part of the Lindhard response function for 1D, 2D and 3D free electrons system at zero temperature. (b) Renormalized acoustic phonon dispersion $\omega_{ren}(\mathbf{q})$ for one-, two- and three-dimensional metals at zero temperature. The bare phonon dispersion $\omega_0$ (dashed black line) is also reported for a comparison. . . . .	20
2.1	Scheme of a photoemission experiment. Light with energy $h\nu$ illuminates the sample. As a result of the photoelectric effect, electrons are emitted into the vacuum, collected by a detector and analyzed as a function of their kinetic energy $E_{kin}$ and their polar $\theta$ and azimuthal $\phi$ angles. . . . .	24
2.2	Fundamental of ARPES measurements. (a) Energetics of the photoemission process. Energy conservation holds, that is $ E_B  = h\nu - \phi - E_{kin}$ where $h\nu$ is the photon energy, $\phi$ the work function, $E_B$ the binding energy of the electron inside the sample and $E_{kin}$ is the kinetic energy of the photoelectron; $E_F$ , Fermi level; $E_{vac}$ , vacuum level; $N(E)$ , density of states. (b) Momentum conservation of electrons. The in-plane momentum $k_{  }$ is conserved because of the translational symmetry in the direction parallel to the sample surface and, as a result, $k_{i  } = k_{f  }$ . On the contrary, there is no conservation of the momentum in the direction perpendicular to the surface, namely $k_{i\perp} \neq k_{f\perp}$ . . . . .	26
2.3	Optical transition between the initial ( $i$ ) and final ( $f$ ) states by the absorption of a photon, which carries an energy $h\nu$ and a momentum $\mathbf{k}_{h\nu}$ . Since $\mathbf{k}_{h\nu}$ is negligible, direct vertical transitions occur within the first Brillouin zone in the <i>reduced-zone scheme</i> or equivalently within higher-order BZs in the <i>extended-zone scheme</i> by the reciprocal lattice vector $\mathbf{G}$ , imparted by the crystal potential. . . .	28

2.4	Illustration of three-step model description of the photoemission process (from [2]). The three steps are: 1) the optical excitation of an electron from an initial state, $E_i$ to a final state $E_f$ , by the absorption of a photon with energy $h\nu$ , 2) the excited electron travels towards the sample surface (along the $z$ -axis) and 3) the transmission of the photoelectron through the sample surface. . . . .	29
2.5	The universal curve of inelastic mean free path (IMFP) for electrons as a function of their kinetic energy according to Ref. [3]. . . . .	32
2.6	Illustration of the photoemission process in TR-ARPES. The pump pulse (red) perturbs the electronic distribution of the sample and then, after a time delay $\Delta\tau$ , the probe pulse (blue) causes photoemission. . . . .	35
2.7	Schematic representation of the optical system for the generation of pump (1.82 eV, 30 fs) and probe (6.05 eV, 65 fs) pulses. FF: fundamental frequency, SH: second harmonic, UV: ultraviolet, DUV: deep ultraviolet, VIS: visible, SHG: second harmonic generation stage, NOPA: non-collinear optical parametric amplifier, SFG: sum frequency generation stage, BS: beam splitter. . . . .	37
2.8	Schematic representation of the UHV system, according to Ref. [4]. The setup is made up of three chambers separated by two vacuum valves: the load-lock chamber with a transfer arm (red), the sample preparation chamber including a couple of evaporators, an Ar <sup>+</sup> sputter gun and a LEED system (navy), and the photoemission chamber directly connected with the hemispherical analyzer for the detection (green). . . . .	39
2.9	Photo of our setup. The photoemission chamber and the hemispherical energy analyzer are in the foreground. . . . .	41
2.10	Sketch of the hemispherical energy analyzer used in our TR-ARPES setup for the detection of photoelectrons. A lens system focuses electrons which come from the sample with a large angular distribution. Subsequently, the electrons enter an energy filter by an entrance slit whose aperture determines the energy resolution. Two biased hemispherical electrodes of radii $R_1$ and $R_2$ ( $R_1 < R_2$ ) disperse electrons as a function of their kinetic energy: electrons at the pass energy $E_p$ follow the central trajectory (green), electrons with $E_{kin} < E_p$ move towards the inner hemisphere (red), electrons with $E_{kin} > E_p$ move towards the outer hemisphere (blue). After crossing an exit slit limiting their number, the dispersed electrons go into a CCD detector, which provides an energy-momentum map. . . . .	42

3.1	Atomic and electronic structure of BP from Ref. [1]. (a) BP crystal structure. Each phosphorene layer, normal to the $z$ -axis, is buckled along the $x$ -axis (armchair direction). (b) First Brillouin Zone (BZ) of bulk BP. The direct bandgap is located at the Z-point. (c) Schematic electronic band structure around the Z-point: band dispersions along the three main axes are estimated from the effective masses reported in Ref. [5]. . . . .	49
3.2	(a) ARPES map of bulk BP along the armchair direction at pump-probe delay + 2.4 ps from Ref. [1]. As a consequence of the optical pumping the CB is also populated. (b) Differential spectra at two fixed delays, i.e. + 50 fs and + 2.4 ps, where red indicates enhancement, whereas blue is depletion. The crosses labeled 1 to 4 mark spectral features whose dynamics is reported in panel (c). . . . .	50
3.3	Analysis of the VB dispersion from Ref. [1]. (a) Zoom-in of the VB ARPES map at + 2.4 ps delay. EDCs are normalized to their maxima. The open symbols indicate the fitted band dispersions (see Paragraph 3.4.1). (b) Comparison of VB dispersions at -0.3 ps (circles), 0 ps (squares) and +2.4 ps (triangles) delays. A parabolic fit is indicated by the black dashed line. (c) VB temporal evolution at $k_x = 0 \text{ \AA}^{-1}$ (open squares) and $k_x = 0.044 \text{ \AA}^{-1}$ (solid squares). Lines are found via a phenomenological fit. Green solid circles are obtained by integrating the VB spectral intensities in the rectangular areas of Panel (b). The vertical axis on the right-hand-side shows the relative intensity $I/I_0$ , normalized to $I_0$ at negative delay. The pump fluence is kept at $0.4 \text{ mJ/cm}^2$ . . . . .	51
3.4	Surface photovoltage (SPV) and transient photo-induced effects from Ref. [1]. (a) ARPES maps after 45 s Cs exposure at three pump fluences ( $0 \text{ \mu J/cm}^2$ , $24 \text{ \mu J/cm}^2$ , $485 \text{ \mu J/cm}^2$ ) and negative pump-probe delay of -1 ps. The asymmetric shape of the CB is an effect of the selection rules in the photoemission. The presence of SPV can be recognized by the shift of the spectra. (b) Bottom scale: surface photovoltage ( $\phi_{SPV}$ ) as a function of the photo-excited carrier density ( $n_{eh}$ ); top scale: $\phi_{SPV}$ as a function of the pump fluence ( $F_{pump}$ ). (c) VB maximum (top) and broadening (bottom) of pristine (open squares), and Cs-doped BP (solid circles) as a function of the pump-probe delay. . . . .	54
3.5	Comparison of EDCs at $k_x = 0 \text{ \AA}^{-1}$ in different doping/pumping conditions. . . . .	55



3.6	Scheme of photoemission process for (a) pristine BP, (b) Cs-doped BP and (c) pumped, Cs-doped BP from Ref. [1]. The upper inset in each panel illustrates the expected ARPES spectrum, the lower shows the measured EDCs at $k_{\parallel} = 0 \text{ \AA}^{-1}$ . $E_F$ : Fermi level, $E_{vac}$ : vacuum level, $\phi_{BB}$ : band bending potential, $\phi_{SPV}$ : surface photo-voltage. . . . .	56
3.7	ARPES maps recorded at $-0.5$ ps pump-probe delay (a)-(c) and at $+1.5$ ps delay (d)-(f) for three increasing Cs exposure times (15 s, 30 s and 45 s, top to bottom) from Ref. [1]. The graphs on the right side (g)-(i) show the corresponding EDCs at $0^\circ$ emission angle ( $k_x = 0 \text{ \AA}^{-1}$ ). In all maps and graphs, zero energy is referred to the <i>onset</i> of the VB at positive delay ( $E_{onset(+)}$ ), for comparative purpose. Pump fluence is $0.4 \text{ mJ/cm}^2$ . All measurements at RT. . .	59
3.8	(a) EDCs of the VB of pristine BP at $k_x = 0 \text{ \AA}^{-1}$ for $-250$ fs (black) and $0$ fs (red) pump-probe delays from Ref. [1]. (b) Numerical derivative of the EDCs shown in panel (a): the solid lines are fits (see text). The resulting peaks are reproduced as shaded areas in panel (a), with the associated peak position $E_V$ and $w_{VB}$ . (c) EDC of the CB at $k_x = 0.04 \text{ \AA}^{-1}$ and $+3$ ps delay: the solid line is a gaussian fit centered at $E_C$ . . . . .	61
3.9	(a) ARPES maps and dispersion fits of CB (top) and VB (bottom) at $+2.4$ ps delay from Ref. [1]. (b) Simulation of the VB photoemission spectrum at negative delay (Ref. [1]): the spectral function $a(E)$ is peaked at $E_V - E_F = -0.09$ eV and decays exponentially at larger binding energy. By a convolution with a gaussian profile $g(E)$ (line width $w = 0.1$ eV), it matches the experimental data. . .	62
3.10	(a) Simulation of electrons and holes diffusion after pump irradiation, according to Eqs.(3.1)-(3.3) from Ref. [1]. The colored surface represents $\delta r(z, t) = [\delta p(z, t) - \delta n(z, t)] / n_{eh}$ as a function of delay $t$ and depth $z$ (blue color: $p < n$ , red color $n < p$ ). Charge separation gives rise to a dipole field $E_d$ that compensates diffusion. (b) Surface charge imbalance at $z = 0$ as a function of delay at $300$ K (green solid line) and $1000$ K (orange dashed line) from Ref. [1]. . .	65
4.1	Composition of transition metal dichalcogenides (TMDs). Periodic table where the shaded areas highlight the transition metals and chalcogens which form the compounds $MX_2$ . . . . .	68
4.2	Schematic representation of the $\text{CdI}_2$ -type $1T$ sandwich structure: the transition metal atom (M) with a octahedral coordination is green, chalcogen atoms (X) are dark blue. . . . .	69

4.3	(a) Periodic lattice distortion (PLD) in the Star-of-David (SoD) configuration in real space (exaggerated). Red dots indicate the central Ta atoms, blue dots indicate the 6 Ta nearest neighbors, orange dots indicate the 6 Ta atoms forming the tips of the star, respectively. For reference, Ta atoms without PLD are shown by the gray dots; (b) parameters $r_B$ and $r_C$ characterizing the SoD configuration. Reprinted from Ikeda, T. N., Tsunetsugu, H., and Yonemitsu, K. (2019). Photoinduced Dynamics of Commensurate Charge Density Wave in 1T-TaS <sub>2</sub> Based on Three-Orbital Hubbard Model. <i>Applied Sciences</i> , 9(1), 70. . . . .	70
4.4	Schematic representation of the band structure of 1T-TaSe <sub>2</sub> along the $\Gamma$ KM direction of the Brillouin zone. (a) Normal phase. (b) Commensurate CDW phase, below 473 K. (c) Commensurate CDW and coexisting Mott phase, below about 260 K. . . . .	72
4.5	Image of typical 1T-TaSe <sub>2</sub> single crystals used for our TR-ARPES measurements from Ref. [6]. . . . .	73
4.6	Bulk resistivity measurements performed at the University of Bath (United Kingdom) from Supplemental material of Ref. [6]. (a) Normalized electrical resistance as a function of temperature. In the inset, the low temperature ( $< 15$ K) range is reported. (b) First derivative of resistance, $dR/dT$ . . . . .	74
4.7	LEED pattern from Ref. [6] obtained on a 1T-TaSe <sub>2</sub> single crystal, which was mounted on the sample holder in the photoemission chamber at the temperature of 77 K. This image was acquired before TR-ARPES measurements in order to determine the sample orientation. . . . .	75
4.8	Full-wavevector ARPES ( $h\nu = 21.2$ eV) images of 1T-TaSe <sub>2</sub> at specific binding energies and at 40 K from Supplemental material of Ref. [6]. (a) Electronic structure at $E_B = E_F - 0.5$ eV. The black line indicates the hexagonal BZ, while grey dashed ellipses point out the Ta-5d derived electron pockets. The labelled high-symmetry points are a projection onto the experimental $k_z$ . (b) Electronic structure at $E_B = E_F - 0.3$ eV (c) Electronic structure at the Fermi level $E_F$ . . . . .	76
4.9	Band dispersions through the BZ from Supplemental material of Ref. [6]. The CDW gap opens up at the $\bar{M}$ point as indicated by the red vertical arrow. The Mott gap extends across all $k$ space as marked by the blue vertical arrow. . . . .	76
4.10	ARPES intensity map at 77 K and at negative pump-probe delay measured at Politecnico di Milano by using 6 eV probe photon energy from Ref. [6]. . . . .	77

4.11	Temporal evolution of the valence band in the CDW-Mott phase from Ref. [6]. (a) TR-ARPES spectra at the $\bar{\Gamma}$ point (77 K) acquired by using $1.10 \text{ mJ cm}^{-2}$ pump fluence. (b) Normalized valence band intensity, extracted from the maximum near $E - E_F \approx -0.35 \text{ eV}$ . (c) Shift of the valence band extracted from a constant intensity contour in panel (a), identified by the yellow dashed line. . . . .	78
4.12	Coherent phonon oscillations in the CDW-Mott phase from Ref. [6]. (a) Oscillatory component of the valence band shift measured by TR-ARPES ( $1.16 \text{ mJ cm}^{-2}$ ). (b) Differential reflectivity signal measured by TRR ( $0.11 \text{ mJ cm}^{-2}$ ), where $\Delta R/R$ is the absolute value of the differential reflectivity. The reported data are for $1.84 \text{ eV}$ probe photon energy. (c) Normalized fast Fourier transform (FFT) amplitude of the TR-ARPES and TRR oscillatory components, together with the Raman spectrum for comparison. . . . .	79
4.13	Temperature dependence of coherent phonons in the CDW phase from Ref. [6]. (a) FFT of the transient reflectivity $\Delta R/R$ signal measured by TRR using $0.11 \text{ mJ cm}^{-2}$ fluence in the range 295-478 K. The reported data is for $1.89 \text{ eV}$ probe photon energy. (b) Raman spectra measured over a similar temperature range as panel (a) for comparison. Panels (c) and (d) display the temperature dependence of the integrated peak area for the $2.0 \text{ THz}$ and $2.7 \text{ THz}$ modes in the TRR-FFT and Raman spectra, respectively. . . . .	81
4.14	Temperature-dependent TR-ARPES measurements. (a) ARPES maps of $1T\text{-TaSe}_2$ at $300 \text{ K}$ (on the left) and $85 \text{ K}$ (on the right) before pump arrival ( $-300 \text{ fs}$ ). (b) Comparison of energy dispersion curves extracted from the $\Gamma$ point ( $k_{\parallel} = 0$ ) at $300 \text{ K}$ (black line) and $85 \text{ K}$ (red line). (c) EDCs extracted from $\Gamma$ point at $300$ and $85 \text{ K}$ are reported again; on the right, the temporal evolutions of the band edge ( $E = -0.26 \text{ eV}$ ) are shown. . . . .	83
4.15	(a) DFT simulations of the charge density wave phase. The black curve refers to the one-layer per unit cell case, while the red curve to the two-layer per unit cell one. The two configurations of unit cell are indicated by the black and red arrows with the same criterion. (b) EDCs extracted from $\Gamma$ point at $300$ and $85 \text{ K}$ . . . . .	84

4.16	Temporal evolution of the band edge. (a) Oscillation at 300 K (15 mW pump power): experimental data are indicated by the blue curve, the fitting curve by the red curve. In the inset, the FFT of the signal shows one phonon peak at 2.05 THz, confirming the results of the fit. The phase of this phonon mode is minus cosine. (b) Oscillation at 85 K (12 mW pump power): experimental data are indicated by the blue curve, the fitting curve by the red curve. Also in this case, the FFT of the signal agrees with the fit results, showing two phonon peaks at 2.10 and 2.25 THz with opposite phases.	85
4.17	One-dimensional harmonic lattice model. (a) A Ta-plane where the 13 Ta atoms clusters - stars of David - are shown. They can be divided in the central Ta atom (blue), the 6 Ta nearest neighbors ring (green) and the 6 Ta forming the tips of the stars (red). (b) One-layer per unit cell configuration: the 5 Ta atoms placed along a high symmetry direction are connected by springs, where the $h$ , $l$ and $k$ spring constants are similar to one another. (c) Two-layers per unit cell configuration: the presence of an interlayer coupling is taken into account by adding the $s$ spring constant.	86
4.18	CDW amplitude mode. It consists of a coherent movement of the Ta atoms belonging to the same star of David where the central atom is not moving. Ta and Se atoms are indicated by blue and red circles, respectively. The nn ring involves the 6 nearest neighbours Ta atoms, while the tip ring is composed of the 6 next nearest neighbours Ta atoms. The light blue arrows emphasize their radial motion.	87
4.19	Splitting of the CDW amplitude mode (AM) with slightly different frequencies and opposite phases as a consequence of dimerization. On the left, a snapshot of the in-phase oscillations of two neighboring stars of David (in-phase AM). On the right, a snapshot of the out-of-phase oscillations of two neighboring stars of David (out-of-phase AM). These modes resemble the two phonon modes experimentally observed at 85 K (4.16(b)).	88

# List of Tables

2.1	Yb-laser output characteristics. . . . .	37
3.1	$E_g$ is the estimated bandgap, $E_V - E_F$ is the binding energy of the VB, $n_i$ is the intrinsic carrier density, $p_0$ and $n_0$ are the estimated hole (in VB) and electron (in CB) concentrations at room temperature. . . . .	63

*To my beloved family*

## Acknowledgements

First, I would like to thank several people, whose support was essential during my PhD. I would like to express my deep gratitude to my tutor prof. Claudia Dallera and my supervisor dott. Ettore Carpenè for giving me the opportunity to achieve this PhD at Politecnico di Milano. I am really grateful to them for their precious suggestions, constant support and insightful discussions during the studies, the experiments and the writing of this dissertation.

A very special thank goes to dott. Hamoon Hedayat for guiding and helping me during these years and for being there whenever I needed help: I have no words to express your patience, perseverance, and spirit of sacrifice: thank you for always being there for me!

I would also like to thank Andrea Mazzanti and Argiro Giakoumaki, my office colleagues and friends: you were the first people I met at Politecnico. Thank you for your valuable support, your availability and all your suggestions and advice. You are very good company and I am very happy to have met you.

I would also like to express my sincere appreciation to prof. Federico Bottegoni, Andrea Picone, Franco Ciccacci, Alberto Brambilla and Carlo Zucchetti for their warm encouragement and moral support during my PhD. I am also very grateful to our collaborators prof. Enrico Da Como and Daniel Wolverson from the University of Bath and dott. Charles J. Sayers from our department for our very fruitful discussions about science and the constant collaboration.

My deepest thanks go to my colleagues and special friends Caterina Amendola, Benedetta Talone and Michele Lacerenza who have always supported me even outside working life. Their presence in my life was and still is very important for me! Thank you for making these years I spent at Milan very special and memorable.

Finally, I would like to express all my gratitude to my family for the unconditional love, sacrifice, care and support they have always given me over the past few years. Without you, none of this would have been possible.

# Abstract

This thesis presents the exploration and the understanding of phase transitions and extreme non-equilibrium conditions in two-dimensional (2D) materials such as transition metal dichalcogenides (TMDs) and black phosphorus (BP). In this context, ultrafast spectroscopy is a useful and promising tool to study the origin of complex orders. The mainly employed technique is time- and angle-resolved photoemission spectroscopy (TR-ARPES) which allows revealing dynamics of the electronic band structure of the material under investigation, thanks to its energy and momentum sensitivity. By changing the time delay between two ultra-short pulses, one can study time-dependent processes taking place after the pump-induced non-equilibrium electronic state with sub-picosecond resolution. Besides the femtosecond TR-ARPES, time-resolved reflectivity (TRR) measurements on the aforementioned materials are also performed. Indeed, despite the lack of momentum resolution of the technique, TRR provides a significant understanding about the out-of-equilibrium behavior of the electronic and lattice degrees of freedom, allowing a more extensive knowledge of the material properties.

In the last few years, layered two-dimensional materials, such as graphene and hexagonal boron nitride (h-BN), have received significant attention due to their potential applications in several fields. Graphene, a single layer of graphite, was the first 2D material to be obtained via mechanical exfoliation from bulk graphite in 2004. Because of its attractive properties, the discovery of graphene has stimulated the investigation of other layered 2D materials, which are able to complement the demands related to graphene and can be employed as platforms for exploring new physical and chemical phenomena. Recently, the scientific community has drawn great attention on TMDs, owing to their special electrical, mechanical, and optical properties as well as to their possible technological applications. Among TMDs, the tantalum-based compounds  $\text{TaX}_2$  with  $\text{X} = \text{S}$  or  $\text{Se}$  are of particular interest because they are host to coexisting strongly correlated phases including charge density waves (CDWs) and an unusual metal-insulator transition (MIT). These materials exhibit several CDW phases as incommensurate (ICCDW), nearly-commensurate (NCCDW) and commensurate (CCDW), with transition temperatures over a broad range extending from 75 K up to 473 K. The TMD of our interest is  $1T\text{-TaSe}_2$ . In this sample, the NCCDW phase is not observed and there is just a direct transition from the CCDW to an ICCDW phase at 473 K. At lower temperature, below about 260 K, a surface Mott metal-insulator transition has been observed. TR-ARPES and TRR allowed us to study the interplay between charge density wave (CDW) and Mott phases in  $1T\text{-TaSe}_2$ , revealing that the Mott phase is preferentially linked to the main phonon mode addressed as the CDW amplitude mode.

As regarding BP, we investigated this material by TR-ARPES both in its pristine



condition and after Cs deposition, revealing a rich photo-induced band dynamics. This material exhibits intricate interactions associated with charge, spin, lattice and orbital degrees of freedom whose deeper comprehension is fundamental for optoelectronic, electronic and technological applications. This semiconductor has a tunable bandgap as a function of surface doping by alkali atoms and strain, and exhibits anisotropic electronic and optical properties whose origins are rooted in the puckering of its lattice structure. We found that photo-injected carriers trigger a bandgap renormalization and a concomitant valence band flattening due to Pauli blocking. In the Cs-doped sample, photoexcitation causes a long-lived surface photovoltage that compensates the Cs-induced surface band bending. Therefore, thanks to our investigation, it was possible to disentangle bulk from surface electronic states, to establish the surface localization of the conduction band and to clarify the occurrence of band inversion in bulk samples.

## Introduction

“What could we do with layered structures with just the right layers? What would the properties of materials be if we could really arrange the atoms the way we want them?” The American physicist Richard Feynman asked these questions in his famous lecture entitled *There’s Plenty of Room at the Bottom*. The aim of arranging materials at the atomic scale is very attractive, to such an extent as to be a major goal of materials science even around sixty years after Feynman’s lecture. In this scenario, two-dimensional (2D) materials have recently emerged as an encouraging platform for the invention of novel heterostructures and optoelectronic devices as well as for the understanding of fascinating physical phenomena, such as superconductivity, spin and orbital order or charge density waves (CDWs). The most typical property of 2D materials results from their special van der Waals structure. Bulk crystals are made of single layers vertically stacked by van der Waals forces instead of covalent bonds. This configuration makes it possible to reduce the crystal thickness in the direction normal to the 2D planes. As a consequence, the sample thickness can be decreased to the atomic layer scale with remarkable modifications of the physical properties.

The world’s first two-dimensional material is graphene, whose isolation paved the way for new opportunities in the field of condensed matter physics and materials. At the beginning, research on graphene has drawn attention owing to its special massless Dirac fermion-like electronic structure and the resulting possible applications in electronics. However, limitations arising from the gapless nature of this material leads to the search for other 2D specimens with intermediate bandgaps. In this regard, 2D semiconducting transition metal dichalcogenides (TMDs) have been proven to have bandgaps tunable with respect to the film thickness, ensuring a greater flexibility. These materials exhibiting the form  $\text{MX}_2$  with M a transition metal and X a chalcogen atom (such as S, Se or Te) have been showing promising applications in several research fields as condensed matter physics, electronic devices, chemical sensors and energy storages [7–9]. In addition, since TMDs are host to strongly correlated phases, several theoretical and experimental studies of their possible phase diagrams have been performed, enabling to unravel complex competition between various phases. In order to disclose all the potential of TMDs, great efforts are still continuing.

Besides TMDs, other innovative 2D semiconductors also deserve to be carefully investigated. A well-known example is that of black phosphorus (BP), the most stable allotrope of elemental phosphorus, which was recently reintroduced as a striking semiconductor one hundred years after its first bulk synthesis in 1914. One of the distinctive features of BP is its real-space structure consisting of parallel buckled layers held together by van der Waals forces where the monolayer is called phosphorene. This puckered structure in the real space induces a large

in-plane anisotropy in its electronic, optical and phonon properties, creating opportunities for designing new devices and applications. No less importantly, BP exhibits high carrier mobilities [5] and a tunable bandgap over the entire infrared range, attributing to it a distinctive place between graphene and TMDs [10].

The purpose of this thesis is to investigate BP and a specific tantalum-based TMD, i.e.  $1T$ -TaSe<sub>2</sub>, by two ultrafast spectroscopy techniques, which are time- and angle-resolved photoemission spectroscopy (TR-ARPES) and time-resolved reflectivity (TRR). Due to its capability to directly probe electrons, TR-ARPES provides the dynamics of the electronic band structure of the examined material after optical excitation [11]. As a result, one of the major advantages of this technique is the possibility to control the collapse and recovery of electronic order in strongly correlated systems as well as to study the ultrafast non-equilibrium response of novel materials for future opto-electronic applications. Although TR-ARPES is a powerful tool in the field of ultrafast spectroscopy, in order to have a more complete vision about the out-of-equilibrium state of matter, TRR measurements on the aforementioned samples are also carried out. Even though TRR exploits the same experimental scheme involved in TR-ARPES, i.e. the so-called pump-probe scheme, the dynamics is retrieved in different ways: photoemission spectroscopy is based on the detection of electrons extracted by the sample, while time-resolved optical spectroscopy detects reflected or transmitted photons. Hereafter, the various subjects dealt with in this thesis work are organized as follows.

In Chapter 1, some theoretical fundamentals and prerequisites, which are necessary for a clearer understanding of this dissertation, are presented. In light of the semiconductive nature of the materials under investigation, a brief overview about the general properties of semiconductors is provided. Subsequently, the main physical phenomena, photo-induced in black phosphorus and experimentally observed by our TR-ARPES investigations, are described. The processes we are talking about are Burstein-Moss shift (BMS), bandgap renormalization (BGR) and surface photovoltage (SPV). As we will see, since they simultaneously occur, their recognition and disentanglement is not trivial. The third and last part of Chapter 1 describes the concept of charge density waves (CDWs) in one-dimension with reference to the Peierls model and, then, in higher dimensions. Indeed, the knowledge of the main features of this ground state of matter is fundamental for explaining our TR-ARPES and TRR results regarding  $1T$ -TaSe<sub>2</sub>.

In Chapter 2, the experimental techniques employed in this work are described. Firstly, a theoretical description of the photoemission process is presented. According to quantum mechanics, photoemission should be treated as a one-step process. However, it is commonly discussed within the framework of the three-step model, based on a phenomenological approach. After presenting the three-step model and many-body effects, our TR-ARPES setup, which is composed of an optical appara-

tus for the generation of pump and probe pulses, an ultra-high vacuum system and a detection system, is described. Finally, theoretical and technical details relevant to TRR are provided. As we will see, by measuring the reflectivity variations of the sample, one can retrieve important information about electron dynamics [12], electron-phonon interaction [13] and the atomic motions [14].

Chapter 3 deals with the electron dynamics in BP. After a brief description of the sample properties, the results of the TR-ARPES measurements on BP and their explanation are shown. In view of its application in optoelectronics, the comprehension of the photo-induced effects in BP is pivotal. In addition, it has been shown that surface doping by alkali atoms enables to engineer the BP bandgap [15, 16]. Therefore, we investigate by TR-ARPES this material in both its pristine condition and after Cs deposition. Thanks to our study, we clarify some crucial points about carrier dynamics photo-induced in black phosphorus, confirm the surface localization of the conduction band and shed light on the occurrence of band inversion in bulk BP.

Finally, Chapter 4 reports on the metal-insulator transition (MIT) in  $1T$ -TaSe<sub>2</sub> and its relationship with the CDW phase by concentrating mainly on the strong coherent phonon oscillations in this material observed by using TR-ARPES and TRR up to several picoseconds. Our investigation shows that the Mott phase is preferentially coupled to a special phonon mode, i.e. the CDW amplitude mode, since it determines the electron localization in the CDW phase, and points out the crucial role of the CDW and lattice in stabilizing the Mott insulating phase of  $1T$ -TaSe<sub>2</sub>. Ultimately, we demonstrate that the combination of TR-ARPES and TRR can be used to study the mechanisms driving phase transitions in a wide range of strongly correlated materials.

# Chapter 1

## Theoretical Background

In solid-state physics, many of the characteristics of a material as the electronic and optical properties are determined by its electronic band structure, which describes the ranges of energy that an electron within it may have (“allowed” bands) and the ranges of energy which it may not have (“forbidden” bands). On the basis of the band theory of solids, three classes of materials can be distinguished, i.e., metals, semiconductors and insulators. Metals have free electrons and a partially filled valence band (VB); therefore, they are highly conductive. On the contrary, both semiconductors and insulators have a filled VB and an empty conduction band (CB), separated by a *bandgap*  $E_g$  which is, by definition, the energy difference between the highest occupied level and the lowest unoccupied level. There is no difference between semiconductors and insulators at  $T = 0$  K because they are all nonconducting. However, semiconductors form a class of solids that are insulators at absolute zero temperature but which may become conductive at higher temperatures (below the melting point). These different behaviors arise from the presence of different energy-gap values: even though a sharp distinction between an insulator and a semiconductor is not feasible, by and large the energy gap in most semiconductors goes from few tenths of electronvolts up to a maximum of 2 eV.

Since the knowledge of semiconductor physics is essential to understand the electronic and optical properties of the materials investigated in this work, a brief overview about the general properties and the band structures of semiconductors is presented in the following. A detailed discussion on this topic can be found in Ref. [17, 18].

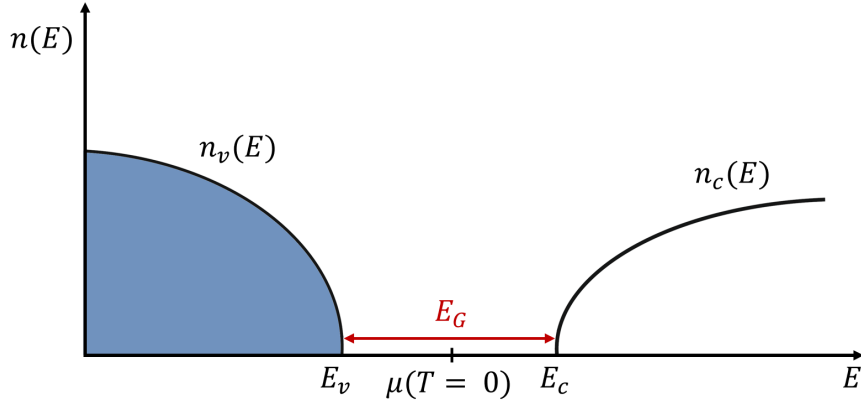


**Figure 1.1.** Scheme of the density-of-states of an intrinsic semiconductor at zero temperature. The top of the VB,  $E_v$ , and the bottom of the CB,  $E_c$ , are separated by a bandgap energy  $E_G = E_c - E_v$ . The chemical potential  $\mu$  at zero temperature lies at the middle of the bandgap.

## 1.1 General Properties of Semiconductors

A semiconductor at zero temperature is characterized by a totally occupied VB and a totally empty CB, where the lowest energy level  $E_c$  of CB and the topmost level  $E_v$  of the VB are separated by the energy gap  $E_g = E_c - E_v$ . In *intrinsic semiconductors*, i.e. an ideal semiconductor free from defects or impurities, no level lies in the energy gap. By contrast, semiconductors which are host to defects, the so-called *extrinsic semiconductor*, have additional impurity levels within the energy gap and show different carrier concentration and transport properties. Hereafter, the main theoretical concepts about the equilibrium carrier distribution in intrinsic semiconductors are illustrated. In an intrinsic semiconductor at zero temperature all the valence states are occupied and all the conduction states are empty as schematically shown in Fig. 1.1, where  $n_v(E)$  and  $n_c(E)$  are the density-of-states per unit volume in VB and CB, respectively, and  $\mu$  is the chemical potential. When the temperature of the semiconductor is increased, a certain number of electrons are *thermally* excited from the VB to the CB, leaving behind holes in the VB. In general, the probability of the occupation of the allowed electron states of energy  $E$  is described by the *Fermi-Dirac* (F-D) distribution which is given by

$$f(E, T) = \frac{1}{e^{(E-\mu)/k_B T} + 1}, \quad (1.1)$$

where  $k_B$  is the Boltzmann constant. At  $T = 0$ , the chemical potential  $\mu$  is equal to the so-called *Fermi level*,  $E_F$  and the F-D distribution is a step function such that all the states with energies  $E < \mu$  are occupied ( $f(E) = 1$ ) and all the

states with energies  $E > \mu$  are empty ( $f(E) = 0$ ) as shown by the blue curve in Fig. 1.2. When the temperature of the system increases, thermal energy excites the electrons (green and red curves in Fig. 1.2). In particular, an electron can thermally absorb an amount of energy of the order of  $k_B T$  (at room temperature  $k_B T \approx 0.025$  eV). However, because of the Pauli exclusion principle, this energy is not equally distributed among all the electrons: if electrons lying well below  $E_F$  absorb energy, they will move to higher levels which are already occupied, thus violating the exclusion principle. As a result, only electrons close to the Fermi level can be excited. Indeed, since the energy levels above  $E_F$  are empty, if those electrons move to higher levels, the exclusion principle is preserved. Therefore, at finite temperature, the F-D deviates from the step function and is broadened by  $\Delta E \propto k_B T$  around  $\mu$ . This is why only electrons with energies in this range can be responsible for electronic transport processes in the material. Note that, in literature, the chemical potential  $\mu$  and the Fermi level  $E_F$  are used interchangeably and this convention is also used throughout this thesis.

Since the conduction, at a certain temperature  $T$ , is caused by electrons in CB levels or holes in VB levels, the most important quantities to be quantified are the density of electrons in the CB,  $n_0(T)$ , and the density of holes (or equivalently the density of missing electrons) in the VB,  $p_0(T)$ , at temperature  $T$ . The number of electrons per unit volume in the CB,  $n_0(T)$ , is given by

$$n_0(T) = \int_{E_c}^{\infty} n_c(E) f(E) dE = \int_{E_c}^{\infty} n_c(E) \frac{1}{e^{(E-\mu)/k_B T} + 1} dE, \quad (1.2)$$

where the subscript 0 is used to indicate quantities at thermal equilibrium. Analogously, the number of holes per unit volume in the VB at temperature  $T$  is expressed as

$$p_0(T) = \int_{-\infty}^{E_v} n_v(E) (1 - f(E)) dE = \int_{-\infty}^{E_v} n_v(E) \frac{1}{e^{(\mu-E)/k_B T} + 1} dE. \quad (1.3)$$

From Eqs. (1.2) and (1.3), the relevance of the chemical potential  $\mu$  in determining  $n_0(T)$  and  $p_0(T)$  is evident. However, simple expressions for  $n_0(T)$  and  $p_0(T)$  can be derived under the following conditions:

$$E_v < \mu(T) < E_c, \quad \text{with} \quad E_c - \mu(T) \gg k_B T \quad \text{and} \quad \mu(T) - E_v \gg k_B T. \quad (1.4)$$

If conditions (1.4) are satisfied, one is dealing with a “*degenerate semiconductor*” (either intrinsic or extrinsic) and the F-D distribution function  $f(E)$  and its complementary distribution function  $[1-f(E)]$  in Eqs. (1.2) and (1.3), respectively, can be simplified with their corresponding Maxwell-Boltzmann distributions:

$$\begin{aligned} \frac{1}{e^{(E-\mu)/k_B T} + 1} &\approx e^{-(E-\mu)/k_B T}, \\ \frac{1}{e^{(\mu-E)/k_B T} + 1} &\approx e^{-(\mu-E)/k_B T}. \end{aligned} \quad (1.5)$$

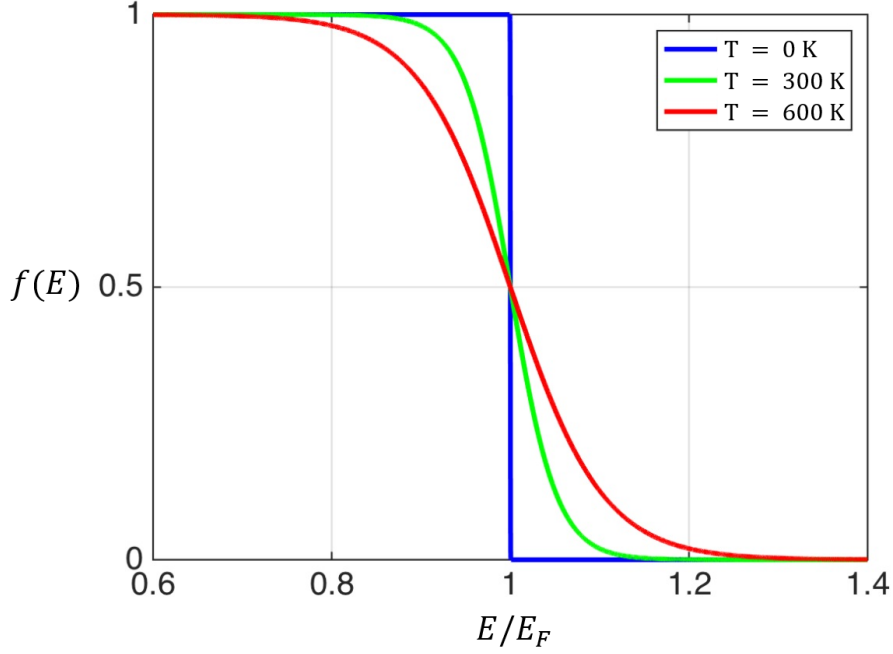


**Figure 1.2.** Fermi-Dirac distribution function  $f(E)$  at different temperatures:  $T = 0$  K (blue curve),  $T = 300$  K (green curve) and  $T = 600$  K (red curve). At zero temperature, the probability of an electron to occupy an energy level below the Fermi level  $E_F$  is equal to 1, while the probability to occupy higher energy levels is equal to 0. At finite temperatures, the distribution gets smeared out because some electrons begin to be thermally excited to energy levels above the chemical potential. Note that the total number of electrons is constant and independent of temperature and that only a small fraction of the total number of electrons can be thermally excited.

As a result, Eqs. (1.2) and (1.3) can be written as

$$n_0(T) = N_c(T)e^{-(E_c-\mu)/k_B T}, \quad (1.6a)$$

$$p_0(T) = N_v(T)e^{-(\mu-E_v)/k_B T}, \quad (1.6b)$$

where

$$N_c(T) \equiv \int_{E_c}^{\infty} n_c(E)e^{-(E-E_c)/k_B T} dE \quad (1.7a)$$

$$N_v(T) \equiv \int_{-\infty}^{E_v} n_v(E)e^{-(E_v-E)/k_B T} dE. \quad (1.7b)$$

which are the *effective conduction band* and *valence band density-of-states*, respectively.



In an intrinsic semiconductor, the number of electrons in the CB is equal to the number of holes left in the VB, i.e.,

$$n_0(T) = p_0(T) \iff N_c(T)e^{-(E_c-\mu)/k_B T} = N_v(T)e^{-(\mu-E_v)/k_B T}. \quad (1.8)$$

From this requirement, an expression for the chemical potential in the *intrinsic case*  $\mu_i(T)$  can be obtained that is,

$$\mu_i(T) = \frac{1}{2}(E_v + E_c) + \frac{1}{2}k_B T \frac{N_v(T)}{N_c(T)}. \quad (1.9)$$

This shows that, as  $T \rightarrow 0$ , the chemical potential  $\mu_i$  is located in the middle of the the energy gap while, at finite temperature, it undergoes a change of the order of  $k_B T$ . By substituting the latter expression for  $\mu_i$  in Eqs. (1.6a) and (1.6b), the *intrinsic concentrations*  $n_i(T)$  and  $p_i(T)$  of electrons and holes are found to be

$$n_i(T) = p_i(T) = \sqrt{N_c(T)N_v(T)}e^{-E_G/2k_B T}. \quad (1.10)$$

Since  $N_c(T)$  and  $N_v(T)$  smoothly depend on the temperature, one can say that the temperature dependence of the intrinsic carrier concentration is principally affected by the exponential dependence on  $E_G$ . Furthermore, notice that while the quantities  $n_0(T)$  and  $p_0(T)$  singularly depend on the chemical potential, their product  $n_0(T)p_0(T)$  does not. Indeed, it is given by

$$n_0(T)p_0(T) = N_c(T)N_v(T)e^{-E_G/k_B T} \equiv n_i^2(T) = p_i^2(T). \quad (1.11)$$

This equation, known as *mass-action law*, implies two important results:

- as the product  $n_0(T)p_0(T)$  does not depend on  $\mu$ , it takes the same value regardless of the impurity concentration in the material;
- at a fixed temperature, knowing the density of one carrier type enables one to obtain the density of the other type of carriers.

It is interesting to explicit the above expressions under the isotropic and parabolic two-band model for semiconductors, according to which valence and conduction band extrema are located at the same point and dispersion energy curves are parabolic as schematically illustrated in Fig. 1.3. For example, the density-of-states per unit volume in the conduction band for  $E \geq E_c$  is given by

$$n_c(E) = \int \frac{2}{(2\pi)^3} \delta(E_c(\mathbf{k}) - E) d\mathbf{k} = \frac{1}{2\pi^2} \left( \frac{2m_c^*}{\hbar^2} \right)^2 (E - E_c)^{1/2}, \quad (1.12)$$

where the parabolic dispersion relation  $E_c(\mathbf{k}) = E_c + \frac{\hbar^2 k^2}{2m_c^*}$  has been substituted and  $m_c^*$  is the *effective mass* of the electrons in CB.

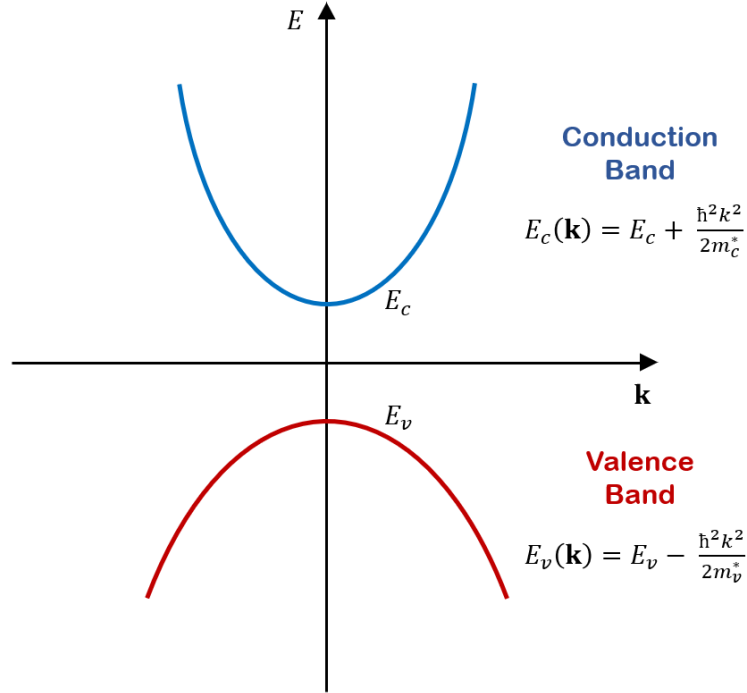


**Figure 1.3.** Isotropic and parabolic two-band model semiconductor. The valence band (red) and the conduction band (blue) with the corresponding dispersion relations are shown. The valence band curve has been reported in red to remind its total occupancy by electrons at  $T = 0$  K.

By putting Eq. (1.12) in Eq. (1.7a), the effective density-of-states in the CB turns out to be

$$N_c(T) = 2.534 \left( \frac{m_c^*}{m} \cdot \frac{T}{300K} \right)^{3/2} \times 10^{19} \text{ cm}^{-3}, \quad (1.13)$$

where  $T$  is to be expressed in degrees Kelvin. By a similar calculation, one finds out that the effective density-of-states in the VB is given by

$$N_v(T) = 2.534 \left( \frac{m_v^*}{m} \cdot \frac{T}{300K} \right)^{3/2} \times 10^{19} \text{ cm}^{-3}, \quad (1.14)$$

where  $m_v^*$  is the effective mass of the holes in VB.

Moreover, within the framework of the isotropic two-band model semiconductor, the chemical potential  $\mu_i(T)$  becomes

$$\mu_i(T) = \frac{1}{2}(E_v + E_c) + \frac{3}{4}k_B T \ln \frac{m_v^*}{m_c^*}. \quad (1.15)$$

According to the last equation, the intrinsic chemical potential lies around the middle of the energy gap. If  $m_v^* = m_c^*$ , it results to be independent of temperature; in all other cases, i.e. when  $m_v^*$  and  $m_c^*$  are different,  $\mu_i(T)$  shifts towards the band edge with lower effective mass by a quantity of the order of  $k_B T$ .

As we will see later, all these results enable us to estimate the order of magnitude of important properties of black phosphorus (BP), one of the materials of our interest; in particular, by measuring its band gap  $E_G$  and VB maximum, an estimation of the equilibrium electron and hole concentrations in BP is achieved, as will be shown in Chapter 3.

## 1.2 Photo-induced Phenomena in Black Phosphorus

Semiconductors under non-equilibrium conditions, e.g. caused by photo-excitation, can be host to several processes, such as interband and intraband absorption, bandgap renormalization (BGR) and Pauli blocking. Even though the equilibrium properties play an important role for the characterization of this class of materials, the investigation of photo-induced out-of-equilibrium phenomena has become increasingly relevant because most optoelectronic devices operate in non-equilibrium conditions. More in detail, in view of the encouraging properties of BP for opto-electronics applications [19–21], the comprehension of its ultrafast out-of-equilibrium response can be useful. For this reason, we have performed a time- and angle-resolved photoemission spectroscopy (TR-ARPES) study on BP both in its pristine state and after Cs deposition, shedding light on open issues about carrier dynamics [22, 23] and revealing meaningful information on its dynamical photo-induced electronic properties. Hereafter, a theoretical description of the two major physical phenomena arising in pristine BP, which are *Burstein-Moss shift* (BMS) and *bandgap renormalization* (BGR), is presented. Subsequently, the effects appearing in Cs-doped BP will be also addressed in order to allow a deep understanding of our experimental results which are shown in Chapter 3.

### 1.2.1 Burstein-Moss Shift (BMS)

The Burstein-Moss shift, also known as the Burstein-Moss effect [24, 25], is the blue shift of the absorption edge caused by *Pauli blocking* (or *band filling*) [26, 27] in semiconductors. It is a well-known phenomenon in chemically doped semiconductors [28, 29] but can be also observed in photo-excited materials [26, 30]. In order to understand the main features of this effect in case of photo-excitation, let us consider the isotropic and parabolic two-band model for semiconductors once again. As shown in Fig. 1.4(a), under equilibrium conditions, the VB is almost

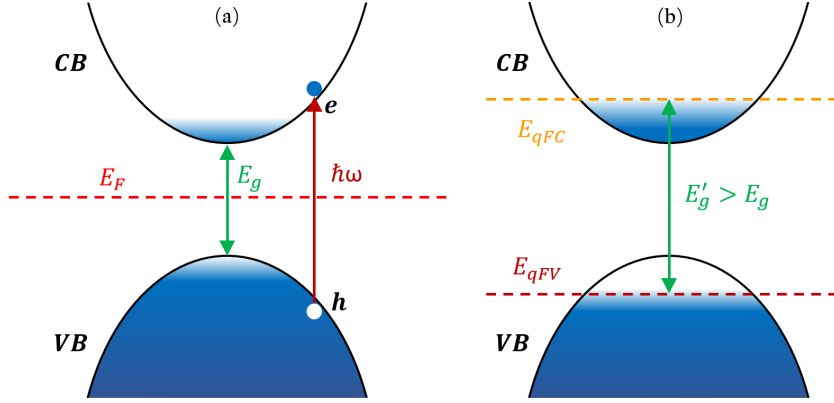


**Figure 1.4.** Burstein-Moss effect caused by Pauli blocking. (a) In equilibrium, VB is almost totally occupied and CB empty. By photo-excitation, electrons are promoted to conduction band-edge states, leaving behind holes in VB. (b) After thermalization, the depletion of the VB maximum and the increase of spectral weight in CB are observed. As a consequence, the bandgap enlarges to  $E'_g = E_{qFC} - E_{qFV}$ , where  $E_{qFC}$  and  $E_{qFV}$  are the quasi-Fermi levels for CB and VB, respectively.

totally occupied, while the CB is empty except for the weak thermal carrier distributions. Under light irradiation, electrons are promoted to the CB leaving holes in the VB. After thermalizing, carriers occupy the corresponding band edges, as depicted in Fig. 1.4(b). As a result, the populations of electrons in the conduction band and valence band are altered and their description occurs by introducing the so-called *quasi-Fermi* levels for CB ( $E_{qFC}$ ) and VB ( $E_{qFV}$ ) [31], both coming from the equilibrium Fermi energy  $E_F$ . Because of this change in the state occupancy, there will be fewer empty electronic states available at the bottom of the CB. As optical transitions to occupied states in CB are not allowed for Pauli's exclusion principle, the absorption edge is shifted to higher energies and the optical bandgap is increased to  $E'_g = E_{qFC} - E_{qFV}$ . For this reason, the Burstein-Moss effect, i.e. the upward shift of the CB edge and the downward shift of the VB edge, is caused by *Pauli blocking* or *band filling*. As we will see in Chapter 3, the recognition of this phenomenon, which takes place in our measurements on pristine BP, has been challenging because it occurs together with another optically induced many-body effect affecting the energy gap value, that is bandgap renormalization (BGR).

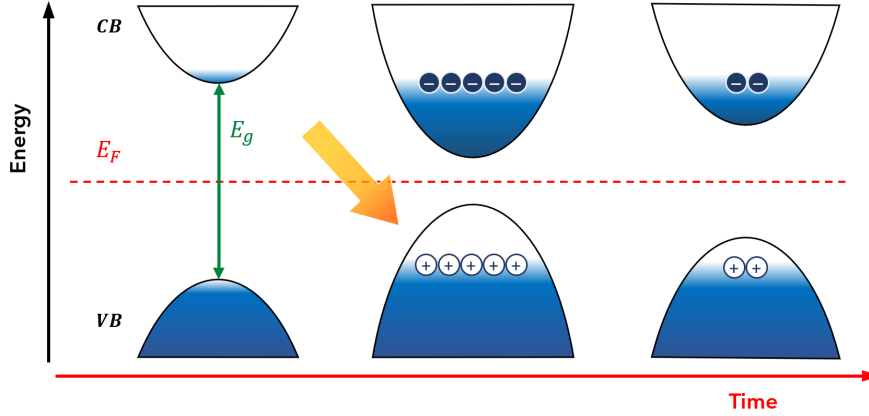


**Figure 1.5.** Schematic illustration of the BGR phenomenon. Before optical excitation (left panel), VB is almost fully occupied and CB empty except for the weak thermal carrier distributions;  $E_F$  lies within the bandgap. Upon optical excitation (central panel), electrons are excited in the CB and holes are left behind in the VB. These high-mobility charge carriers determine a bandgap shrinkage. The initial bandgap is then restored in time (right panel).

### 1.2.2 Bandgap Renormalization (BGR)

Another important many-body effect which can be observed in photo-excited semiconductors is a carrier density-dependent narrowing of the electronic bandgap, a phenomenon referred to as bandgap renormalization. This bandgap shrinkage results from opposite energy shifts of valence and conduction bands and it is caused by many-body exchange-correlation effects [32, 33] arising from the presence of free carriers – electrons in the conduction band and holes in the valence band – generated by optical pumping. A schematic representation of the photo-induced bandgap renormalization mechanism is illustrated in Fig. 1.5.

In pristine BP, it has emerged that BME and BGR can be simultaneously induced by photo-excitation, partially compensating each other. Indeed, according to BME, an increase in carrier density determines the filling of states in CB, thus moving the absorption onset to higher energies; on the contrary, BGR leads to a reduction of the bandgap energy  $E_G$  with increasing carrier density because of electron-ion and electron-electron interactions. The total effect of the occurrence of these two phenomena on the pristine BP band structure and its dynamics will be explained in more detail in Chapter 3.

### 1.2.3 Surface Photovoltage (SPV)

In addition to pristine BP, we also investigated by time- and angle-resolved photoemission spectroscopy (TR-ARPES) *Cs-doped* BP. In brief, surface doping by alkali adsorption leads to a rigid shift of the overall BP band structure down towards higher binding energies when going from the bulk to the surface (Fig. 1.6a). This is the so-called *band bending* [34], which usually refers to the local changes in electronic structure of semiconductors, in particular, in the energy offset close to their surface or interface, due to space charge effects. Cs surface states are ionized donors and, as a consequence, they lie above  $E_F$ . Since alkali atoms are electron donors [35], a *n*-doped surface region forms after doping, causing a downward band bending [36] characterized by a potential  $\phi_{BB}$ : all energy levels bend downwards when moving from bulk to surface (it would be upwards for acceptor surface doping [36]).

Hererafter, we will focus on another photo-induced process revealed by our TR-ARPES investigations on Cs-doped BP, i.e. *surface photovoltage* (SPV) effect, whose occurrence causes a partial or complete compensation of Cs-induced band bending.

The first works on SPV date back to the early 1950s [37–39]. The fundamental element of this phenomenon is the existence of intrinsic or doping-induced surface/interface states which can donate or accept electrons, leading to the creation of a space-charge layer. By solving the Poisson’s equation  $\nabla^2\phi_{BB} \propto p-n-N_D^+-N_A^-$  where  $\phi_{BB}$  is the built-in potential and  $p, n, N_D^+, N_A^-$  the hole, electron, donor and acceptor densities [36], respectively, the arising band bending can be estimated. The absorption of radiation with photon energies greater than the band gap energy determines the generation of additional carriers both at the valence and conduction bands. The electric field in the space-charge layer spatially divides these opposite charge carriers, causing a band flattening. For this reason, it can be said that the photo-injection of electron-hole pairs compensates the Cs-induced band bending and this mechanism is the SPV effect (Fig. 1.6b).

Even though different experimental applications involving SPV have been developed [40], some features related to time-resolved pump-probe photoemission techniques are mainly highlighted in the following.

E. O. Johnson was the first to point out the logarithmic dependence of SPV with photo-injected carrier density [39], and more recently this model was adapted to time-resolved experiments by other authors [41–43]. As reported in Ref. [44], some constraints arise when considering time-resolved photoemission measurements: the duration of the pump and probe pulses limits the time resolution of the pump-probe method. The latter can be improved by reducing the spot radius of the pump beam and increasing the kinetic energy of the electron as much as possible. Nevertheless, constructive information can be obtained by applying this technique [45].

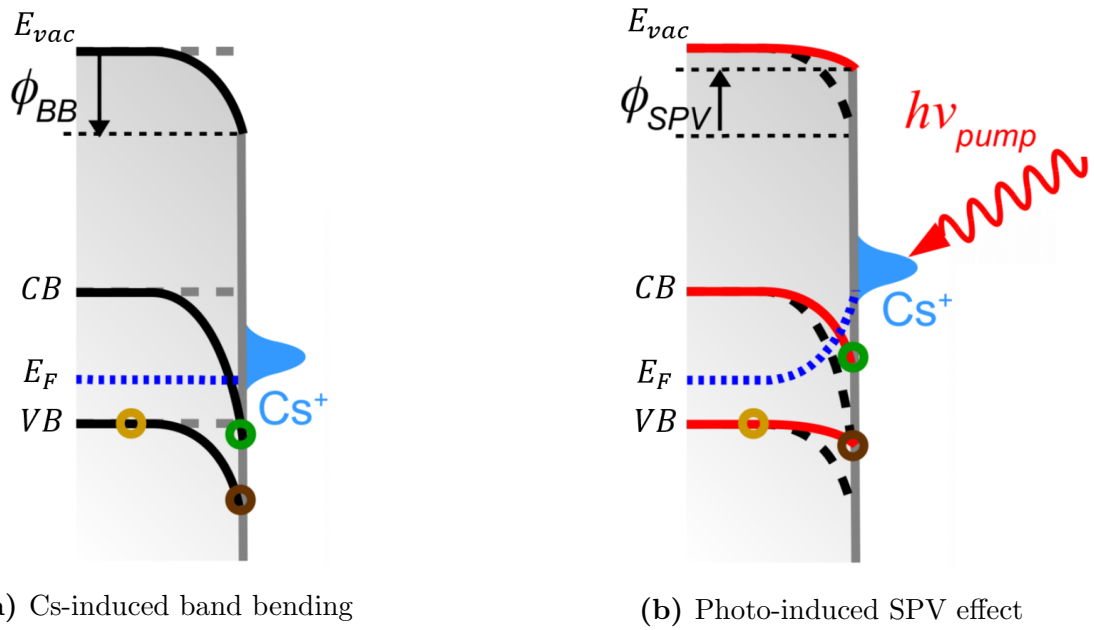


**Figure 1.6.** Schematic diagrams of Cs-induced band bending and SPV effect, taken from Ref. [1]. (a) Surface doping by Cs atoms leads to a downward band bending;  $\phi_{BB}$ : band bending potential. (b) After excitation, SPV develops and all energy levels at the surface shift upward, compensating the bending potential.  $\phi_{SPV}$ : surface photo-voltage.

In particular, it has been shown that [1]:

- by measuring SPV at *negative* pump-probe delay, i.e. when probe photons *precede* the pump pulse, one can get the spatial dependence of the induced electric field (and potential) outside the sample surface [44];
- at positive pump-probe delay, SPV sets in before photoemission and measuring the band energy shifts at these delays enables one to estimate the SPV temporal decay [45].

A more detailed and quantitative description of both cases which will be provided in Chapter 3 where the band structure and charge dynamics of BP are analyzed in-depth.

### 1.3 Charge density waves (CDWs)

Solids with highly anisotropic electronic properties and crystal structure at sufficiently low temperature can undergo a transition to a new ground state called *charge density wave* (CDW). The latter is a static modulation of the electron charge density usually accompanied by a periodic distortion of the underlying lattice. In brief, the electronic energy of the material is lowered as a result of the lattice distortion, the associated strain energy of which is more than counterbalanced by the decrease of the electronic energy. Therefore, if the energy necessary to distort the crystal lattice is less than the gain in electronic energy, the material experiences a phase transition to the CDW ground state. The Sommerfeld model, which is the simplest way to represent the electronic structure of metals, is first presented. Successively, a simple and well established model, which was proposed by Rudolf Peierls [46] in 1955 to describe the fundamental instability in a one-dimensional (1D) linear chain metal, will be reported. According to the Peierls model, one-dimensional equally spaced chain with one electron per ion is unstable at low temperatures due to the electron-electron and electron-phonon interactions, resulting in a CDW. The Peierls' picture was then applied to higher dimensional materials to clarify the occurrence of CDWs based on the concept of Fermi surface nesting (FSN) [47]. Here, some features of the Fermi surface topology and its effects on the formation of CDWs are examined with reference to the behaviour of the electronic susceptibility and the renormalization of phonon dispersion. Even though CDW is an important concept in modern solid state physics, relevant to several physical phenomena [48], the origin of CDW is still under debate, partly because the formation and properties of CDW are highly material dependent. This circumstance has sparked our interest in complex systems, the so-called transition metal dichalcogenides, and in particular in 1T-TaSe<sub>2</sub>, which is host to strongly correlated phases including CDWs.



### 1.3.1 Free-electron theory of metals

An electron moving in a crystal is affected by the presence of the potential energy caused by all the nuclei and all the other electrons. In principle, given a specific material, one should calculate the related crystalline potential, which is not simple to estimate in most cases. However, many of the observed electronic properties of metals, especially of the so-called simple metals, can be explained by the *Sommerfeld* model. The latter is based on a free-electron approach, which consists in neglecting the electron-ion and electron-electron interactions and assuming that the conduction electrons feel an “effective” constant potential. The dispersion energy relation of the CB is assumed to have a parabolic shape, that is

$$E(\mathbf{k}) = E_c + \frac{\hbar^2 k^2}{2m}, \quad (1.16)$$

where  $E_c$  indicates the bottom of the CB. Without loss of generality,  $E_c$  is set to zero in the following.

Another important aspect of the Sommerfeld model is that electrons must follow the F-D statistics and the state occupation probabilities are described by the F-D distribution given by Eq. (1.1) and shown in Fig. 1.2. As explained in Section (1.1), at  $T = 0$  K, the electron system is in its ground state, where the  $N$  free electrons occupy the  $N$  lowest available energy levels up to the  $E_F$ . Since each state can accommodate two electrons with opposite spin according to the Pauli’s exclusion principle, the band is filled from the lowest energy state up to  $N/2$ . Furthermore, in the reciprocal space (the  $\mathbf{k}$ -space), the occupied states of energy  $E(\mathbf{k}) < E_F$  are separated from the empty states of energy  $E(\mathbf{k}) > E_F$  by the so-called *Fermi surface*, which is defined by the equation  $E(\mathbf{k}) = E_F$ . In other words, at  $T = 0$  K, the occupied states form a *Fermi sphere* of radius  $k_F$ , named the *Fermi wavevector*, as depicted in Fig. 1.7.

In order to calculate  $k_F$ , it is imposed that the total number of electrons within the Fermi sphere coincides with the number  $N$  of free electrons in the material:

$$N = \sum_{\mathbf{k}}^{k < k_F} 2 = 2 \frac{V}{(2\pi)^3} \frac{4}{3} \pi k_F^3 = \frac{V}{3\pi^2} k_F^3 \quad \implies \quad k_F^3 = 3\pi^2 n, \quad (1.17)$$

where  $n = N/V$  is the electron density, being  $V$  the volume of the crystal, and the sum over  $\mathbf{k}$  is converted into the corresponding integral times  $V/(2\pi)^3$  [17]. As a result, the Fermi energy for a non-interacting electron system is given by:

$$E_F = \frac{\hbar^2 k_F^2}{2m} = \frac{\hbar^2}{2m} \left( \frac{3\pi^2 N}{V} \right)^{2/3}, \quad (1.18)$$

with  $m$  the electron mass. Therefore, for the system of free electrons confined to a volume  $V$  in the framework of the Sommerfeld model, only electrons at the Fermi

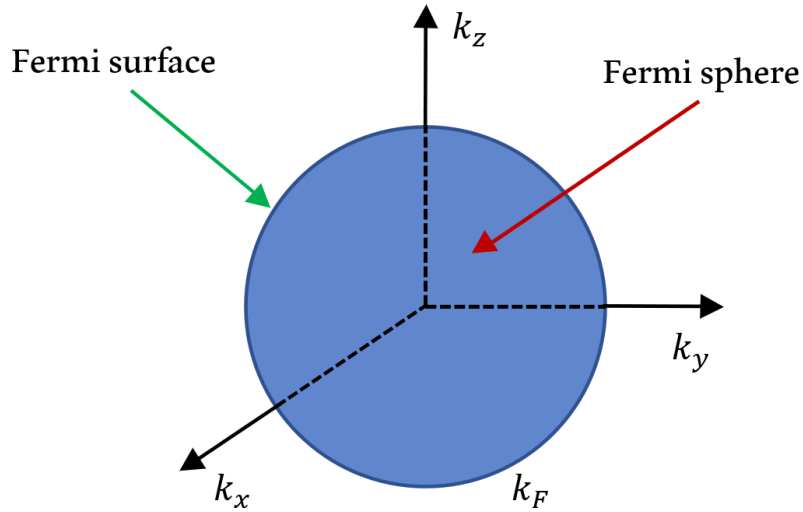


**Figure 1.7.** Schematic illustration of the Fermi surface and of the Fermi sphere formed by occupied band states in the reciprocal space. At  $T = 0$ , each state with wavevector  $\mathbf{k}$  such that  $k < k_F$  accommodates two electrons with opposite spin.

surface or within  $k_B T$  can affect the electronic properties. More generally, the Fermi surface topology of real materials can be more complex depending on the crystal structure, including symmetry and the arrangement of atoms.

### 1.3.2 CDW in 1D: Peierls model

Here, the basic features of the Peierls model are discussed on the base of the description proposed by *Grüner* [49].

Let us consider an ideal one-dimensional chain metal at  $T = 0$ . If electron-electron and electron-phonon interactions are neglected, the ground state of the system and the corresponding free electron energy dispersion result to be as the ones shown in Fig. 1.8(a). The lattice is a periodic linear array of atoms equally spaced by a lattice constant  $a$ ; the electron states are filled up to the Fermi level  $E_F$  associated to the Fermi wavevector  $k_F$  and the charge density  $\rho(r)$  is uniform (black straight line in 1.8(a)). If electron-phonon interactions are taken into account a change in the atomic periodicity of the chain is energetically favorable: the system undergoes a periodic lattice distortion (PLD) as illustrated in Fig. 1.8(b), which is called the *Peierls distortion* [46]. In particular, for a half-filled band, the atomic periodicity becomes  $2a$  and, as a consequence, the charge density results to be modulated

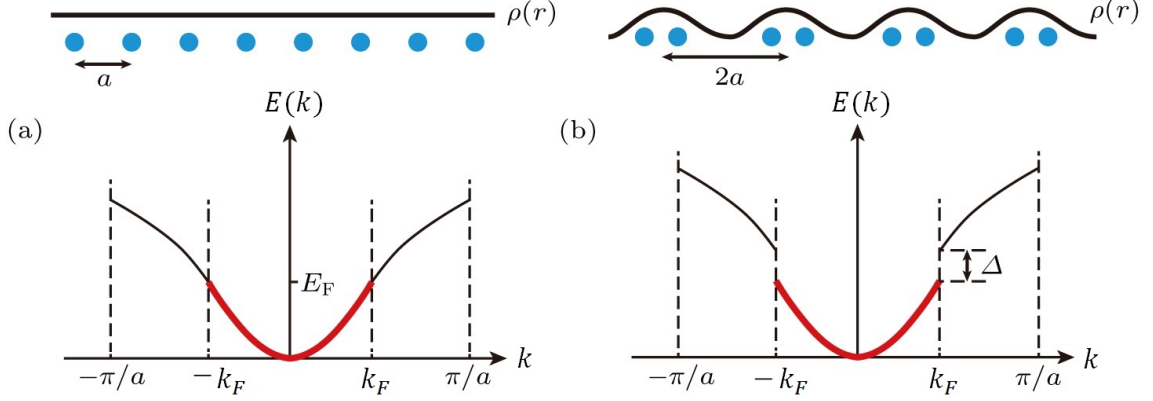


**Figure 1.8.** Illustration of the Peierls model for a 1D linear chain metal with a half-filled band. (a) In the normal state, the lattice constant is  $a$  and the charge density  $\rho(r)$  is uniform. Electrons are filled up to the Fermi level  $E_F$ . (b) The electron-phonon interactions gives rise to a lattice distortion, the so-called *Peierls distortion*, leading to a periodic modulation in the charge density. As a result, a charge density wave (CDW) state forms. The opening of a gap  $\Delta$  around  $E_F$  in the electronic dispersion causes the total energy of the system (the sum of electronic and lattice components) to decrease.

with a period  $\lambda_{CDW}$  related to the Fermi wavevector  $k_F$ :

$$\lambda_{CDW} = \frac{\pi}{k_F}. \quad (1.19)$$

The new real-space unit cell containing two atoms has doubled and, as a result, the k-space BZ has halved. With regards to the single-particle electron dispersion, this distortion causes the opening of a gap  $\Delta$  around the Fermi level  $E_F$  at the new BZ boundary as shown in Fig. 1.8(b). Therefore, there is a metal-to-insulator transition, where the resulting insulator is usually called the *Peierls insulator*. Since the occupied states of the band are lowered below  $E_F$ , the formation of the gap leads to decrease in the electronic energy  $E_{el}$ , which in the case of weak electron-phonon coupling is given by [50]

$$E_{el} = n(E_F) \left[ -\frac{\Delta^2}{2} - \Delta^2 \log \left( \frac{2E_F}{\Delta} \right) \right], \quad (1.20)$$

where  $n(E_F)$  is the electron density at the Fermi level. At the same time, the distortion determines an increase in the elastic energy of the lattice  $E_{lat}$  given by

$$E_{lat} = \frac{n(E_F)\Delta^2}{\lambda}, \quad (1.21)$$

where  $\lambda$  is the dimensionless electron-phonon coupling constant. As a result, the total change in energy of the system is the sum of the two terms in Eqs. (1.20) and (1.21):

$$E_{tot} = E_{el} + E_{lat} = n(E_F) \left[ -\frac{\Delta^2}{2} - \Delta^2 \log \left( \frac{2E_F}{\Delta} \right) + \frac{\Delta^2}{\lambda} \right]. \quad (1.22)$$

By minimizing the latter quantity, for  $\lambda \ll 1$ , one obtains that the gap is given by

$$\Delta = 2E_F e^{-1/\lambda}, \quad (1.23)$$

and that the energy difference between the normal state  $E_{normal}$  and the CDW state  $E_{CDW}$  is equal to

$$E_{con} = E_{normal} - E_{CDW} = \frac{1}{2} n(E_F) \Delta^2. \quad (1.24)$$

This difference is the so-called condensation energy and its positive sign reveals that the energy of the CDW ground state  $E_{CDW}$  in 1D is lower than the one of the normal state  $E_{normal}$ .

The alteration of the electron dispersion causes a modulation of the charge density  $\rho(x)$ , which proves to be a periodic function of the position  $x$  given by

$$\begin{aligned} \rho(x) &= \rho_0 + \frac{\Delta \rho_0}{\hbar v_F k_F \lambda} \cos(2k_F x + \varphi) \\ &= \rho_0 + \rho_1 \cos(2k_F x + \varphi), \end{aligned} \quad (1.25)$$

where  $v_F = \frac{\hbar}{m} k_F$  is the Fermi velocity and  $\rho_0$  is the electron density of the metal in the absence of electron-phonon interaction which is equal to  $\rho_0 = \frac{\pi}{k_F}$  in one dimension. Furthermore,  $\rho_1$  and  $\phi$  are the amplitude and phase of this periodic charge modulation, respectively.

The consequence of electron-phonon interactions is the formation of a collective mode composed of electron-hole pairs involving the wave vector  $q = 2k_F$ . This collective mode is associated with the electron density modulation described by Eq. (1.25) and the corresponding condensate is called the charge density wave (CDW). As in superconductors or other condensates, the CDW state can be characterized in terms of a complex order parameter

$$\Delta = |\Delta| e^{i\phi}. \quad (1.26)$$

The amplitude  $|\Delta|$  is related to the single-particle CDW gap, indicated only as  $\Delta$  previously;  $\phi$  is the phase of the collective mode, analogous to phase  $\varphi$  in Eq. (1.25).

Let us now consider the same one-dimensional chain metal at finite temperature. In this case, electrons can be thermally excited across the gap: these transitions lead to a screening of the electron-phonon interaction which causes a lowering of the amplitude of the CDW gap and of the extent of the lattice distortion. Therefore, at  $T > 0$ , the transition to the CDW state can still occur and it results to be a second-order phase transition which takes place at the critical temperature  $T_{CDW}$  known as the Peierls temperature [49]. Within the framework of the mean-field theory, where the one-dimensional fluctuations are neglected, the temperature dependence of the order parameter  $|\Delta(T)|$  is given by [50]

$$|\Delta(T)| \propto |\Delta(0)| \left(1 - \frac{T}{T_{CDW}^{MF}}\right)^{1/2}, \quad (1.27)$$

where  $|\Delta(0)|$  is the zero temperature gap and  $T_{CDW}^{MF}$  is the mean-field CDW transition temperature. Above  $T_{CDW}^{MF}$  the system is a metal, while it becomes an insulator below  $T_{CDW}^{MF}$  according to Eq.(1.27).

Another important feature of the CDW states is that they can be classified according to their *commensurability* with the underlying periodic lattice: if the period of the CDW modulation is a multiple of the lattice constant  $a$ , i.e. if  $\lambda_{CDW} = (m/n)a$  where  $m$  and  $n$  are integers, the CDW is indicated as *commensurate* (CCDW); on the contrary, if the periodicity of the charge density is not compatible with that one of the underlying lattice, one speaks about *incommensurate* CDW (ICCDW). As we will see, the transition metal dichalcogenide  $1T$ -TaSe<sub>2</sub> exists in the incommensurate CDW phase below 600 K and in the commensurate CDW phase below 473 K [51].

### Collective excitations of charge density waves

As previously seen in Section 1.3.2, the spatial modulation of electron charge density and the lattice displacement of the CDW state can be described by the complex order parameter  $\Delta = |\Delta|e^{i\phi}$  (see Eq. (1.26)). As expected for a complex order parameter, both phase ( $\phi$ ) and amplitude ( $|\Delta|$ ) excitations can occur. These two different types of collective excitations of a CDW are shown in Fig. 1.9 for the  $q = 0$  case. A collective oscillation of the CDW phase  $\phi$ , commonly referred to as a *phason*, in the  $q = 0$  limit corresponds to the translational motion of the condensate (Fig. 1.9(b)). On the contrary, for an amplitude excitation, or directly an *amplitudon*, there is no displacement of the charge density with respect to the ions but only a change in the charge density wave amplitude throughout the lattice (Fig. 1.9(a)).

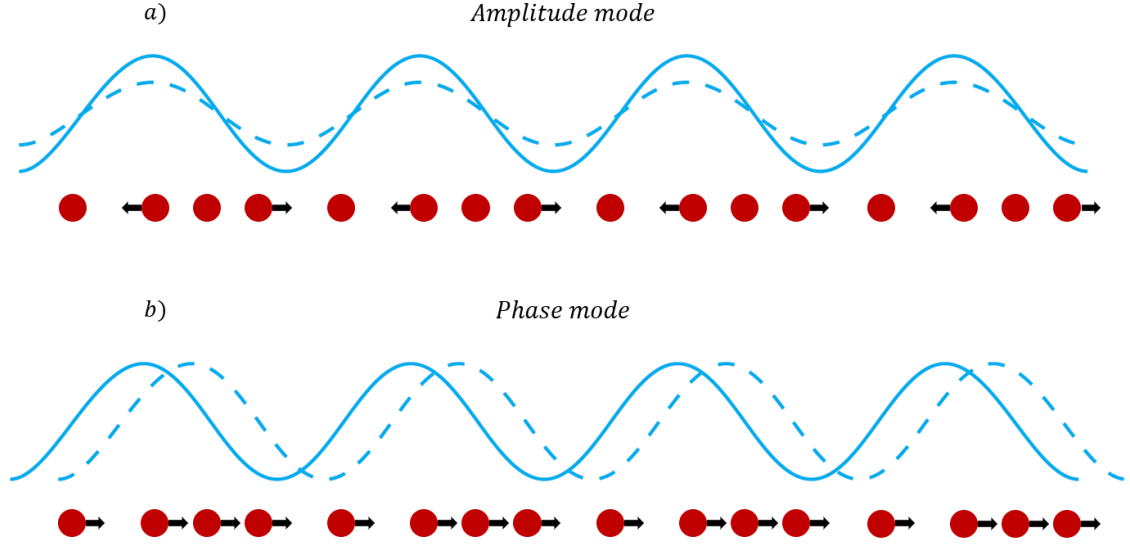


**Figure 1.9.** Excitation of amplitude (*amplitudon*) and phase (*phason*) of a charge density wave in the  $q = 0$  limit. Lines indicate changes to the charge density, while red circles are the ions. Arrows show the variations in the ion position.

### 1.3.3 CDW in higher dimensions: Fermi surface nesting

The extension of the Peierls picture to higher dimensional systems can be achieved by analyzing the Fermi surface topology because the shape of the Fermi surface can have a remarkable effect on physical properties of a material via its influence on electron screening. The standard way to deal with higher dimensional electron gases consists in evaluating the *electronic susceptibility*  $\chi(\mathbf{q}, \omega)$ , which quantifies the response of the electrons to a perturbation of wavevector  $\mathbf{q}$  and frequency  $\omega$ , and then to study its zero energy value, i.e.  $\chi(\mathbf{q}, \omega = 0)$ , to establish if a Peierls transition can be driven by the electron response.

For simplicity, let us consider again an ideal 1D chain of atoms as in Section 1.3.2. The corresponding ideal 1D Fermi surface consists of two parallel sheets at  $\pm k_F$  as shown in Fig. 1.10(a), where electronic states in opposite sheets can be connected by a single wavevector  $\mathbf{q} = 2\mathbf{k}_F$ , spanning the Fermi contours. In the free electron model, electron-electron correlations are neglected and the response function  $\chi(\mathbf{q}, \omega)$  can be estimated by means of Lindhard approximation. The resulting Lindhard susceptibility function is given by

$$\chi^0(\mathbf{q}, \omega) = \sum_k \frac{f(E_{\mathbf{k}}) - f(E_{\mathbf{k}+\mathbf{q}})}{E_{\mathbf{k}} - E_{\mathbf{k}+\mathbf{q}} - \hbar\omega - i\delta} |M(\mathbf{q})|^2. \quad (1.28)$$

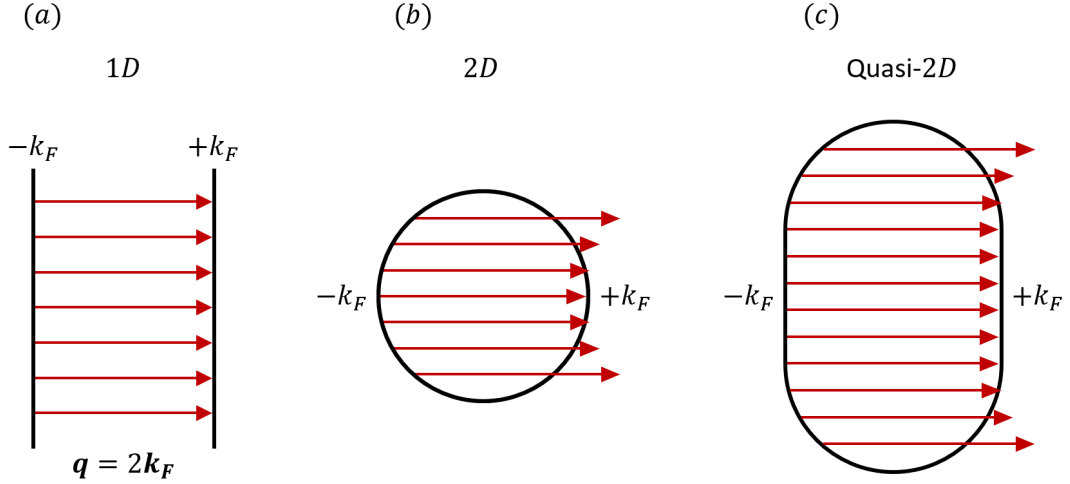


**Figure 1.10.** Fermi surface nesting for a 1D, 2D and quasi-2D electron gas. (a) In 1D, the Fermi surface of free electrons is composed of two parallel sheets at  $\pm k_F$ . A perfect nesting is fulfilled because the single nesting wavevector  $\mathbf{q} = 2\mathbf{k}_F$  is able to span the whole Fermi surface. (b) In 2D, the Fermi surface is circular. Because of this shape, only a reduced portion of the Fermi surface is nested by  $\mathbf{q}$ , leading to a poor nesting. (c) . In a quasi-2D system, the Fermi surface is elliptical, therefore large parallel portions of the Fermi surface can be nested, thus achieving a moderate nesting. The red arrows in all three cases indicate pairs of states, one occupied and one empty, differing by the wavevector  $\mathbf{q} = 2\mathbf{k}_F$ .

Here,  $f(E_{\mathbf{k}})$  and  $f(E_{\mathbf{k}+\mathbf{q}})$  are the F-D distributions for energies  $E_{\mathbf{k}}$  and  $E_{\mathbf{k}+\mathbf{q}}$ , respectively, with  $\mathbf{k}$  the original wavevector and  $\mathbf{k}+\mathbf{q}$  the perturbed one and  $M(\mathbf{q})$  is a matrix element which takes into account the impact of the perturbation on the electrons wavefunctions.

As all the complex functions, also the electronic susceptibility  $\chi^0(\mathbf{q}, \omega)$  has a real part  $\text{Re}[\chi^0(\mathbf{q}, \omega)]$  and an imaginary part  $\text{Im}[\chi^0(\mathbf{q}, \omega)]$  such that  $\chi^0(\mathbf{q}, \omega) = \text{Re}[\chi^0(\mathbf{q}, \omega)] + i \text{Im}[\chi^0(\mathbf{q}, \omega)]$ , where the real part determines the stability of the system [47]. For the case of zero energy transfer limit (or static limit),  $\omega = 0$ , and  $\text{Im}[\chi^0(\mathbf{q}, 0)] = 0$ . The corresponding real part  $\text{Re}[\chi^0(\mathbf{q}, 0)]$  for a free electron system in 1D, 2D and 3D is plotted in Fig. 1.11(a) [50]. Notice that  $\text{Re}[\chi^0(\mathbf{q}, 0)]$  shows a logarithmic divergence at  $\mathbf{q} = 2\mathbf{k}_F$  in 1D. The electronic states contributing most to this divergence in the susceptibility are the pairs of states with the same energy and momenta differing by  $\mathbf{q} = 2\mathbf{k}_F$ . From a physical point of view, this result means that a 1D linear chain metal is unstable at zero temperature, in agreement with the conclusion of the Peierls model. This Fermi surface instability is known as *Fermi surface nesting* and, specifically, the special topology of the 1D

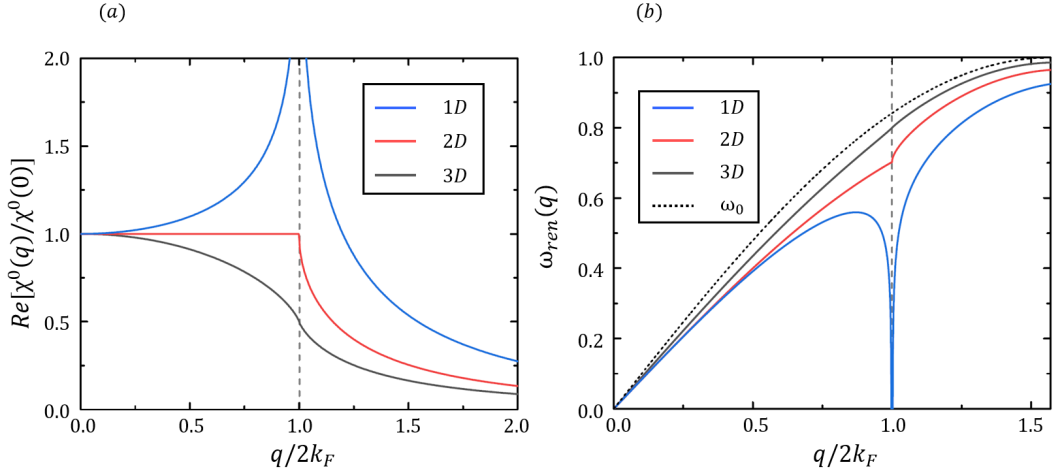


**Figure 1.11.** Behaviour of the bare electronic susceptibility and consequential renormalization of phonon dispersion. (a) Plots of the real part of the Lindhard response function for 1D, 2D and 3D free electrons system at zero temperature. (b) Renormalized acoustic phonon dispersion  $\omega_{ren}(\mathbf{q})$  for one-, two- and three-dimensional metals at zero temperature. The bare phonon dispersion  $\omega_0$  (dashed black line) is also reported for a comparison.

Fermi surface enables segments of the Fermi surface to be linked upon translation by a single vector  $\mathbf{q} = 2\mathbf{k}_F$ , thus achieving a perfect nesting.

By taking into account the electron-phonon interactions, Kohn [52] pointed out that the divergent behaviour of the electronic susceptibility causes the phonon dispersion to undergo a relevant renormalization. Because of the divergence of  $\chi^0(\mathbf{q}, 0)$  near  $\mathbf{q} = 2\mathbf{k}_F$ , there is a remarkable reduction of the phonon frequencies at the wavevectors close to  $2\mathbf{k}_F$  and, in particular, the phonon mode in 1D at  $\mathbf{q} = 2\mathbf{k}_F$  is renormalized to have zero frequency. This is the so-called *phonon softening* and the renormalization of the phonon energy due to electron-phonon interactions is known as the *Kohn anomaly* [53]. The renormalized phonon dispersion arising from this interaction results to be

$$[\omega_{ren}(\mathbf{q})]^2 = [\omega_0(\mathbf{q})]^2 + 2[\omega_0(\mathbf{q})]^2 g^2 \text{Re}[\chi(\mathbf{q}, \omega)], \quad (1.29)$$

where  $\omega_0(\mathbf{q})$  are the bare phonon frequencies, i.e. the normal mode frequencies in the absence of electron-phonon interactions,  $g$  is the electron-phonon coupling constant and  $\text{Re}[\chi(\mathbf{q}, \omega)]$  is here the real part of the interacting susceptibility. As a first approximation, the renormalized phonon frequencies in Eq. (1.29) can be estimated by considering the bare electronic susceptibility instead of the interacting one and the resulting  $\omega_{ren}(\mathbf{q})$  in 1D, 2D and 3D at zero temperature are illustrated in Fig. 1.11(b).



As regards the 2D Fermi surface illustrated in Fig. 1.10(b), here only a small portion of the Fermi surface can be spanned by  $\mathbf{q} = 2\mathbf{k}_F$ , leading to a poor nesting. Generally, the Fermi surface topology determines the nesting conditions. For example, as shown in Fig. 1.10(c), the Fermi surface of a quasi-2D system is elliptical and, as a result, extended parallel portions of the Fermi surface can be linked by  $\mathbf{q} = 2\mathbf{k}_F$ , giving rise to a moderate nesting. A greater degree of Fermi surface nesting implies a greater number of states removed from the Fermi surface and, hence, involved in the transition. Therefore, Fermi surface topologies which can undergo a strong nesting are expected to give rise to a CDW state by Fermi surface nesting.

Until now, only ideal cases have been discussed because the treatment of real materials results to be more challenging [54]. Firstly, the static limit (i.e.  $\omega \rightarrow 0$ ) cannot be always applied. As a consequence, both the real and imaginary parts of the electronic susceptibility must be considered in the study of Fermi surface nesting and a Peierls phase transition can be achieved if there is a peak in the imaginary part of the Lindhard response function at the Fermi surface nesting vector  $\mathbf{q}$  as well as in the real part.

## 1.4 Conclusions

In this Chapter a theoretical background was presented. After summarizing the general properties of semiconductors, a description of some out-of-equilibrium phenomena, which can be photo-induced in these materials, was provided. More in detail, we illustrated the Burstein-Moss shift, bandgap renormalization and surface photovoltage which are observed by our investigations on pristine and Cs-doped black phosphorus. Subsequently, a description of the charge density wave (CDW) ground state was presented. The first part dealt with the Peierls model for the one-dimensional case while, in the second one, the CDW in higher dimensions was addressed. This theoretical overview is fundamental for a clear comprehension and explanation of the findings about the transition metal dichalcogenide 1T-TaSe<sub>2</sub> reported in Chapter 4.

# Chapter 2

## Experimental Details

### 2.1 General Overview

Disclosing the collective behaviour of electronic degrees of freedom in solids has always been a matter of great interest for the scientific community due to the central role played by electronic interactions in many interesting phenomena of condensed matter physics. The most powerful method for probing the electronic structure of solids is arguably angle-resolved photoemission spectroscopy (ARPES). The remarkable advantage of this technique is its ability to map directly the band structures of solid materials by probing simultaneously energy and momentum of electrons. In the past decade, ARPES has experienced a significant progress, including the development of spin-resolved ARPES [55, 56], spatially-resolved ARPES [57, 58], soft-X-ray ARPES [59, 60] and time-resolved ARPES [61, 62]. The latter, extensively used in this work, consists in exciting the material under investigation with an intense ultrashort laser pulse and then measuring ARPES spectra in the time domain by a second UV pulse, allowing one to study ultrafast electronic dynamics and to probe the unoccupied states above the Fermi level ( $E_F$ ). In contrast to static ARPES, which enables one only to resolve the occupied electronic states, time-resolved ARPES, usually named time- and angle-resolved photoemission spectroscopy (TR-ARPES), gives access to both occupied and unoccupied electronic states. Furthermore, thanks to the advancement of electron spectrometers [63], synchrotrons [64–67] and laser light sources [61, 68–70], there has been a considerable improvement in energy and momentum resolution [70, 71]. These technological advances enable to unravel fine features of electronic states (e.g., energy gap in superconductors) with high precision, as well as retrieve information on many-body interactions in strongly-correlated materials.

Another powerful experimental technique, which is widely employed for the investigation of electronic and vibrational dynamics is time-resolved optical spectroscopy.

Even though it exploits the same experimental scheme involved in TR-ARPES, i.e. the so-called *pump-probe* scheme, the dynamics is retrieved in different ways: photoemission spectroscopy is based on the detection of electrons extracted by the sample, while time-resolved optical spectroscopy detects reflected or transmitted photons. In this work, time-resolved reflectivity (TRR) experiments, which consist in measuring the photo-induced variations of sample reflectivity, were performed. Despite the lack of momentum resolution of the technique, TRR enables one to achieve a significant understanding about the out-of-equilibrium behaviour of the electronic and lattice degrees of freedom, allowing an extensive knowledge of the material properties.

This second chapter reports on the experimental techniques used in this work and is organized as follows. In Section 2.2 a theoretical overview about angle-resolved photoemission spectroscopy is presented along with an illustration of the three-step model and many-body effects. In Section 2.3, a general introduction to time- and angle-resolved photoemission spectroscopy is provided and subsequently our TR-ARPES setup is outlined in detail. Ultimately, Section 2.4 briefly describes the TRR setup.

## 2.2 Angle-Resolved Photoemission Spectroscopy (ARPES)

Nowadays, photoemission spectroscopy is considered as one of the most powerful experimental techniques to analyse the electronic structure and the chemical state of solids, surfaces and molecules. Since the electronic structure can affect several properties of matter, this technique plays an essential role in the characterization of emerging materials as well as in the investigation of unknown electronic phenomena.

### 2.2.1 Photoemission Spectroscopy

The expression *photoemission spectroscopy* (PES) is used to indicate all techniques based on the photoelectric effect, such as ultraviolet photoelectron spectroscopy (UPS), X-ray photoelectron spectroscopy (XPS) and angle-resolved photoelectron spectroscopy (ARPES). Originally observed by Hertz in 1887, this effect was explained in 1905 by Einstein, who stated that, in certain circumstances, light can behave as quanta of electromagnetic energy called *photons*. When a light beam of frequency  $\nu$  impinges on a sample, one can think that a stream of photons with energy  $h\nu$  interacts with the electrons of the material: an electron can absorb a photon and escape from the sample with a maximum kinetic energy  $h\nu - \phi$  where  $\phi$  is the material *work function*, i.e., a measure of the potential barrier at the

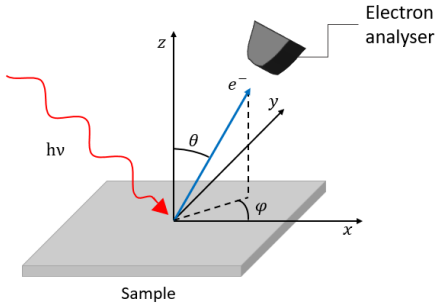


**Figure 2.1.** Scheme of a photoemission experiment. Light with energy  $h\nu$  illuminates the sample. As a result of the photoelectric effect, electrons are emitted into the vacuum, collected by a detector and analyzed as a function of their kinetic energy  $E_{kin}$  and their polar  $\theta$  and azimuthal  $\phi$  angles.

surface that does not allow the valence electrons to escape (generally  $\phi \approx 4\text{-}5$  eV for metals). The ejected electrons travel from the sample to an energy analyzer, which records their kinetic energies, and then to a detector, where the number of photoelectrons at different kinetic energies is counted. A simplified illustration of this process is shown in Fig. 2.1.

By exploiting the photoelectric effect, a material sensitive and non-damaging probe is given by PES, which enables scientists to examine the chemical composition of a solid by X-ray photoelectron spectroscopy (XPS) [72] as well as the electronic structure of matter by ultraviolet photoelectron spectroscopy (UPS) [73] or angle-resolved photoemission spectroscopy (ARPES) [74]. Among all its possible applications, ARPES method, on which our measurements are based, will be described in the following.

ARPES technique is a spectroscopic method to investigate the momentum-dependent electronic band structure of solids. A quantitative interpretation of the experimental data provided by ARPES is usually conducted within the *independent electron approximation* (i.e., the electron-electron interaction in the crystal is neglected) and under the *sudden approximation* (i.e., the response of the system to the formation of photoholes is supposed instantaneous and the interaction between the escaping photoelectron and the system is ignored). From a quantum-mechanical point of view, photoemission should be treated as a one-step process, that is an optical transition between initial and final states coinciding with  $N$ -electron wave functions: the initial state should be an  $N$ -electron eigenstate of the semi-infinite medium, whereas the final state an eigenstate of the ionized ( $N - 1$ )-electron semi-infinite medium (the latter must involve a propagating plane-wave component for taking into account the photoelectron moving in vacuum). Furthermore, according to this approach, the following total energy and momentum conservation laws for the incoming photon and the  $N$ -electron system must be respected:

$$E_f^N - E_i^N = h\nu, \quad (2.1)$$

$$\mathbf{k}_f^N - \mathbf{k}_i^N = \mathbf{k}_{h\nu}. \quad (2.2)$$

The indexes  $i$  and  $f$  denote the initial and final state, respectively, while  $\mathbf{k}_{h\nu}$  is the wave-vector of the impinging photon with energy  $h\nu$ . Despite the greater rigorousness of this theory, photoemission data are commonly discussed within the framework of the *three-step model*, which has been shown to well describe the underlying physics of the photoemission process though it is a purely phenomenological approach. For this reason, a more extensive description of photoemission spectroscopy in the context of the three-step model as well as its application for the investigation of the electronic structure of solids will be provided in the following.

### 2.2.2 Theory of ARPES

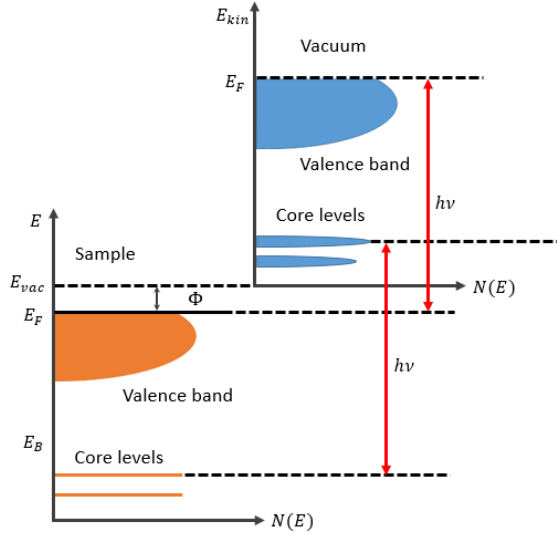
In ARPES experiments, both the energy and the emission angles of photo-emitted electrons are measured: the most important feature of the technique is that energy and momentum conservation laws must hold. As a consequence, experimental maps of electronic band structure can be directly revealed by this technique, which has been successfully used to investigate a wide class of materials [74–76]. The energetics of the photoemission process is shown in Fig. 2.2a, whereas for its geometry one refers to Fig. 2.1. The sample, which has to be properly aligned before the measurement, is irradiated by a photon beam. If the energy of the absorbed photons is greater than the work function of the material, photoemission occurs and the emitted electrons escape into vacuum. An electron energy analyser – in our case an *electrostatic hemispherical analyser* – with a finite acceptance angle collects the photoelectrons after having dispersed them according to their kinetic energy. In this way, one can measure the kinetic energy  $E_{kin}$  of the photoelectrons for a given emission angle. Once the kinetic energy is known, one can determine the modulus of the photoelectron wave-vector in vacuum  $\mathbf{k}_f$  which is given by  $k_f = \sqrt{(2mE_{kin})}/\hbar$ ; in addition, the knowledge of the polar ( $\vartheta$ ) and azimuthal ( $\varphi$ ) emission angles provides access to its components parallel and perpendicular to the sample surface, i.e.  $\mathbf{k}_{f||} = \mathbf{k}_{f,x} + \mathbf{k}_{f,y}$  and  $\mathbf{k}_{f\perp} = \mathbf{k}_{f,z}$ , respectively, where

$$k_{f,x} = \frac{1}{\hbar} \sqrt{2mE_{kin}} \sin \theta \cos \varphi, \quad (2.3)$$

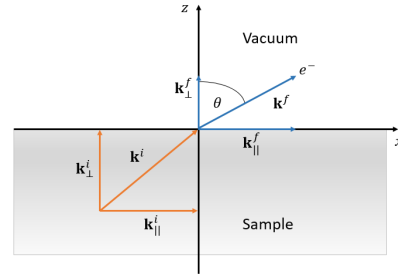
$$k_{f,y} = \frac{1}{\hbar} \sqrt{2mE_{kin}} \sin \theta \sin \varphi, \quad (2.4)$$

$$k_{f,z} = \frac{1}{\hbar} \sqrt{2mE_{kin}} \cos \theta. \quad (2.5)$$

As already mentioned before, the power of the technique lies in the fact that energy and momentum of the electrons inside the sample are directly connected to those of the photoelectrons by the conservation of energy and momentum parallel to the sample surface (see Fig. 2.2b). Within the independent electron approxi-



(a) Energy diagram



(b) Conservation of parallel momentum  $k_{||}$

**Figure 2.2.** Fundamental of ARPES measurements. (a) Energetics of the photoemission process. Energy conservation holds, that is  $|E_B| = h\nu - \phi - E_{kin}$  where  $h\nu$  is the photon energy,  $\phi$  the work function,  $E_B$  the binding energy of the electron inside the sample and  $E_{kin}$  is the kinetic energy of the photoelectron;  $E_F$ , Fermi level;  $E_{vac}$ , vacuum level;  $N(E)$ , density of states. (b) Momentum conservation of electrons. The in-plane momentum  $k_{||}$  is conserved because of the translational symmetry in the direction parallel to the sample surface and, as a result,  $k_{i||} = k_{f||}$ . On the contrary, there is no conservation of the momentum in the direction perpendicular to the surface, namely  $k_{i\perp} \neq k_{f\perp}$ .

mation, the following relations must hold:

$$|E_B| = h\nu - \phi_{sample} - E_{kin} \quad (2.6)$$

$$\hbar k_{i\parallel} = \hbar k_{f\parallel} = \sqrt{2mE_{kin}} \sin \theta \quad (2.7)$$

Eq. (2.6) represents the energy conservation law, which is illustrated in Fig. 2.2a:  $E_{kin}$  is the kinetic energy of a photoelectron,  $h\nu$  is the photon energy,  $|E_B|$  is the modulus the binding energy ( $E_B < 0$ ) of the electron inside the sample and  $\phi_{sample}$  is the work function of the material with respect to the Fermi level  $E_F = 0$  eV, that in a metal is the energy needed for an electron to go from the highest occupied level  $E_F$  to the vacuum level  $E_{vac}$ . Notice that the energy of electrons inside the sample – before the photoemission process takes place – is  $E_{kin} = h\nu - |E_B|$ .

Eq. (2.7) expresses the in-plane momentum conservation:  $k_{i\parallel}$  and  $k_{f\parallel}$  are the modulus of the components parallel to the surface of the crystal momentum and the external wave-vector, respectively, and  $m$  is the free-electron mass. By matching the bulk Bloch eigenstate, describing the excited electrons inside the material, to a free-electron plane wave, which is the state of the photoemitted electron in vacuum, one can formally achieve the transmission of the photoelectron through the sample surface; by taking into account the translational symmetry on the surface plane (i.e., the  $x$ - $y$  plane), the conservation law, reported in Eq. (2.6) and illustrated in Fig. 2.2b, can be derived. Noticeably, the photon momentum is neglected in Eq. (2.7) because photons with energies lower than few tens of eV, which are normally employed in ARPES experiments, carry a momentum which is much smaller than the momentum of photoelectrons (e.g., at  $h\nu = 10$  eV,  $k \approx 0.005 \text{ \AA}^{-1}$ ). Therefore, the optical transition between the initial and final states can be treated as a direct vertical transition within the first BZ in the *reduced-zone scheme* ( $\mathbf{k}_f - \mathbf{k}_i = 0$ ) as depicted in Fig. 2.3. However, the same optical transition can be equivalently considered in the *extended-zone scheme* ( $\mathbf{k}_f - \mathbf{k}_i = \mathbf{G}$ ) as a transition between points of the reciprocal space connected by a reciprocal-lattice vector  $\mathbf{G}$ , given by the crystal potential [77]. Finally, the conservation laws in Eqs. (2.6) and (2.7) are valid when the relaxation time of the electron-hole pairs is much longer than the time required for the photoelectrons to escape into the vacuum, which is of the order of several tens of attoseconds [78].

A different argument applies to the perpendicular component of the wave vector  $\mathbf{k}_\perp$ , which is not conserved passing from the sample into the vacuum because the surface of the material breaks the translation symmetry in this direction ( $\mathbf{k}_{i\perp} \neq \mathbf{k}_{f\perp}$ ). For this reason, one cannot completely determine the total momentum of the electron inside the sample  $\mathbf{k}_i$ . As a result, by typical ARPES investigations one can map out an electronic dispersion relation  $E(\mathbf{k}_\parallel)$  along a well-defined direction in the reduced two-dimensional (2D) Brillouin Zone (BZ),

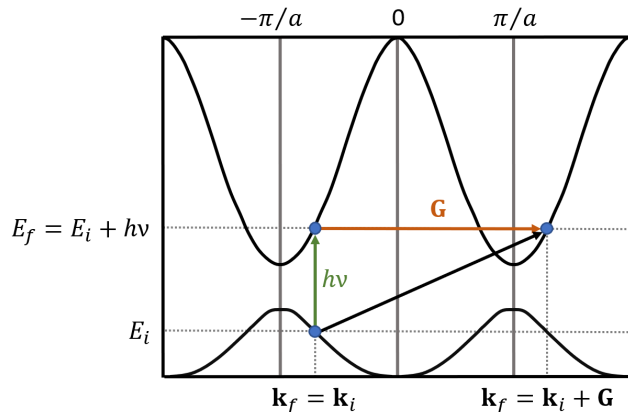


**Figure 2.3.** Optical transition between the initial ( $i$ ) and final ( $f$ ) states by the absorption of a photon, which carries an energy  $h\nu$  and a momentum  $\mathbf{k}_{h\nu}$ . Since  $\mathbf{k}_{h\nu}$  is negligible, direct vertical transitions occur within the first Brillouin zone in the *reduced-zone scheme* or equivalently within higher-order BZs in the *extended-zone scheme* by the reciprocal lattice vector  $\mathbf{G}$ , imparted by the crystal potential.

which is the result of the projection of the three-dimensional (3D) BZ on the surface. Generally, the dependence on  $\mathbf{k}_\perp$  cannot be neglected; however,  $\mathbf{k}_\perp$  is less important in low-dimensional systems with an anisotropic electronic structure and a negligible dispersion along the direction normal to the surface (i.e., along the  $z$  axis). Alternatively,  $\mathbf{k}_{i\perp}$  can be obtained by invoking for the final states the *free-electron approximation*, which is valid for high photon energy ( $\approx 10^2$  eV) [74] and according to which one can express  $\mathbf{k}_{i\perp}$  as

$$\mathbf{k}_{i\perp} = \sqrt{2m(E_{kin} \cos^2 \theta + V_0)}/\hbar. \quad (2.8)$$

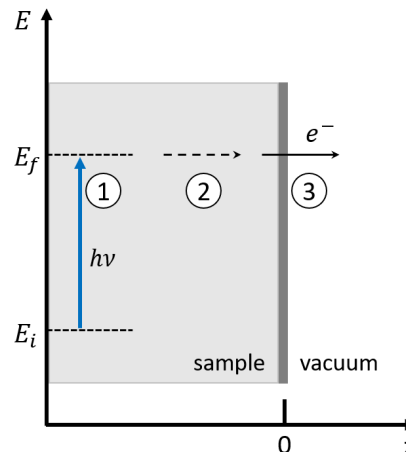
The constant  $V_0$  is a volumetric average of the electrostatic potential in a solid-state material and it is called the *inner potential*. By performing photon energy-dependent measurements and then fitting the experimental periodicity along the  $\mathbf{k}_\perp$  direction, one can determine  $V_0$ . Once  $V_0$  is known,  $\mathbf{k}_{i\perp}$  can be extracted.

### 2.2.3 Three-step Model

An accurate theoretical description of the photoemission needs a full quantum-mechanical approach with the so-called *one-step model*. As discussed in Subsection 2.2.1, the main feature of this model is that it handles photon absorption, electron emission and detection as a single coherent process, describing bulk, surface and evanescent states within a single Hamiltonian. Although the one-step model is more rigorous, ARPES data are usually discussed within the simpler framework



**Figure 2.4.** Illustration of three-step model description of the photoemission process (from [2]). The three steps are: 1) the optical excitation of an electron from an initial state,  $E_i$  to a final state  $E_f$ , by the absorption of a photon with energy  $h\nu$ , 2) the excited electron travels towards the sample surface (along the  $z$ -axis) and 3) the transmission of the photoelectron through the sample surface.



of the *three-step model*. The latter is a phenomenological model developed by Berglund and Spicer [79] in 1964 which divides the photoemission event into three consecutive processes [36]:

1. optical excitation of an electron in the bulk;
2. propagation of the electron to the surface;
3. emission of the electron from the sample into the vacuum.

Fig. 2.4 shows a representation of the photoemission process according to the three-step model. Step 1) is directly related to the electronic structure of the material. Step 2) depends on scattering processes, such as electron-electron scattering or scattering by defects which can modify the electron momentum and energy affecting the sensitivity of the technique. More in detail, the migration of electrons to the surface is influenced by their mean free path as well as their kinetic energy. Lastly, step 3) is connected to the transmission probability of the excited electrons across the surface, which in turn is determined by the electron energy and the work function of the specimen. As a result, the total photoemission intensity arises from the product of three quantities: the total probability for the optical transition, the probability of migration towards the surface and the probability of transmission through the surface.

As concerning step 1), the transition probability  $w_{if}$  for an optical excitation from an initial state  $\psi_i^N$  to a final state  $\psi_f^N$  for an  $N$ -electron system can be approximated by the Fermi's golden rule:

$$w_{if} = \frac{2\pi}{\hbar} |\langle \psi_f^N | H_{int} | \psi_i^N \rangle|^2 \delta(E_f^N - E_i^N - h\nu), \quad (2.9)$$

where  $H_{int}$  is the light-matter interaction Hamiltonian, while  $E_i^N = E_i^{N-1} - E_B^{\mathbf{k}}$  and  $E_f^N = E_f^{N-1} + E_{kin}$  are the energies of the  $N$ -particle system before and after the excitation, respectively ( $E_B^{\mathbf{k}}$  is the binding energy of the photoelectron with kinetic energy  $E_{kin}$  and momentum  $\mathbf{k}$ ). Under the electric dipole approximation and in the linear optical regime, the light-matter interaction is described as a perturbation given by

$$H_{int} = -\frac{e}{2mc}(\mathbf{A} \cdot \mathbf{p} + \mathbf{p} \cdot \mathbf{A}) = -\frac{e}{mc}\mathbf{A} \cdot \mathbf{p} \quad (2.10)$$

Here,  $\mathbf{p}$  is the electronic momentum operator,  $\mathbf{A}$  is the electromagnetic vector potential, which depends on the photon polarization and energy.

Let us now evaluate the transition probability  $w_{if}$ . In many-body calculations of photoemission spectra for a system of interacting electrons, the *sudden approximation* is generally invoked. The wave functions in Eq. (2.9) can be written as the product of a  $(N-1)$ -electron wave function  $\psi^{N-1}$  related to the electronic system after the excitation of one electron, and the wave-function of the photoemitted electron  $\phi^{\mathbf{k}}$ . Moreover, for Pauli principle to be satisfied, the product of these two wave-functions needs to be antisymmetrized by applying the antisymmetric operator  $A$ , i.e., the  $N$ -electron initial and final states can be written as

$$\psi_i^N = A\phi_i^{\mathbf{k}}\psi_i^{N-1} \text{ and } \psi_f^N = A\phi_f^{\mathbf{k}}\psi_f^{N-1}, \quad (2.11)$$

respectively. At this point, it is important to note that the sudden approximation is strictly appropriate only for photoelectrons with high kinetic energy. This is due to the fact that the time required by low kinetic energy photoelectrons to escape into vacuum, as in our case, is longer than the system response time. In this context, the so-called *adiabatic limit*, it is no longer possible to factorize the original  $N$ -electron wave function into two independent terms and electron-electron interaction and screening effects should be taken into account. Nevertheless, to the lowest order, the main aspects of the photoemission process are well explained in the framework of the sudden approximation, even for slower photoelectrons.

Given the factorization of the total wave functions  $\psi^N$  as indicated in Eq. (2.11), the matrix element in Eq. (2.9) can be calculated as the product of two terms, namely as  $\langle \psi_f^N | H_{int} | \psi_i^N \rangle = M_{f,i}^{\mathbf{k}} \cdot c_{m,i}$  where  $M_{f,i}^{\mathbf{k}} = \langle \phi_f^{\mathbf{k}} | H_{int} | \phi_i^{\mathbf{k}} \rangle$  is the one-electron dipole matrix element, while  $c_{m,i} = \langle \psi_m^{N-1} | \psi_i^{N-1} \rangle$  is the overlap integral between the initial state wave function of the  $(N-1)$ -electron system and one of its possible final states [74]. Hence, the total photoemission intensity as a function of  $E_{kin}$  at a fixed momentum  $\mathbf{k}$ , which is given by  $I(\mathbf{k}, E_{kin}) = \sum_{f,i} w_{fi}$ , results to be proportional to the quantity [74]:

$$\sum_{f,i} |M_{f,i}^{\mathbf{k}}|^2 \sum_m |c_{m,i}|^2 \delta(E_{kin} + E_m^{N-1} - E_i^N - h\nu), \quad (2.12)$$

Here, the final energy of the system  $E_f^N$  is expressed as the sum of the kinetic energy of the photoelectron in the solid  $E_{kin}$  and the energy of the system left behind  $E_m^{N-1}$ .

Depending on the values of  $M_{f,i}^{\mathbf{k}}$  and  $c_{m,i}$ , different ARPES spectra can be obtained. As an example, if  $|c_{m,i}|^2$  (the probability that, after the excitation of an electron from the state  $i$ , the remaining  $(N - 1)$ -electron system goes to the final excited state  $m$ ) is different from zero (and equal to 1) only for one particular state  $m = m_0$ , the corresponding ARPES spectra will be described by a delta function. A very different case is that one of a strongly correlated system: for such a material, there will be no zero  $|c_{m,i}|^2$  for several  $m$  and, as a result, ARPES spectra will be more complex [74].

Eq. (2.12) must be multiplied by the terms related to step 2) and step 3), namely the probabilities of propagation towards the surface and transmission across the surface. During their migration to the surface, the excited electrons can undergo scattering processes which do not allow all electrons to reach the surface. Electrons scattered during the propagation towards the surface, which are disregarded by the model, give rise to secondary electrons which generate a background in photoemission spectra.

### Inelastic mean free path and sensitivity

In performing an ARPES experiment, an important parameter to take into account is the probe photon energy because it plays a leading role in setting the technique sensitivity. More precisely, the probe photon energy determines the kinetic energy of electrons in the solid, which in turn influences the so-called *inelastic mean free path* (IMFP)  $\lambda$ . The IMFP is defined as the mean distance, measured along the trajectory, that an electron with a given energy travels between inelastic collisions within a substance. As accurately described in [3], the IMFP of electrons in solids as a function of their kinetic energy seems to obey a *universal curve*, which is shown in Fig. 2.5. After the absorption of a photon, the excited electron migrates towards the sample surface and, successively, it will be emitted into the vacuum. While travelling to the surface, inelastic scattering processes between the excited electron and sample impurities or other electrons can occur. Once arrived to the surface, the inelastically scattered electrons will give rise to a background in photoemission spectra and, as a result, there will be a “secondary spectrum” overlapped to the “primary spectrum” of the photoelectron distribution. However, from a theoretical point of view, in the three-step model only primary electrons, which reach the surface without losing their kinetic energy, are considered. As concerning electrons photoemitted by 6 eV probe photons, such as those employed in our ARPES experiments, they can propagate without undergoing inelastic scattering events along a distance of about 10 nm. Indeed, primary electrons will lose their energy

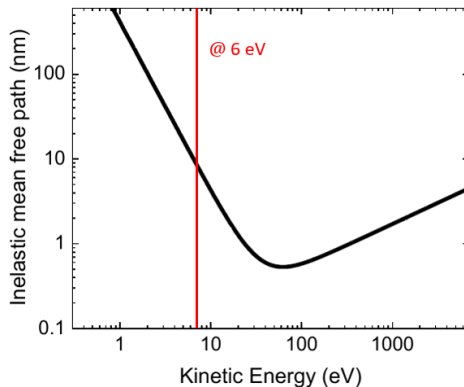


**Figure 2.5.** The universal curve of inelastic mean free path (IMFP) for electrons as a function of their kinetic energy according to Ref. [3].

when crossing the sample-vacuum interface due to the work function  $\phi$ , hence, as long as they are inside the medium, their kinetic energy is given by  $E_{kin} = h\nu - |E_B|$ . In particular, photoelectrons at the Fermi level ( $E_B = 0$  eV) will have a kinetic energy equal to the photon energy and, as a result, their IMFP will be  $\approx 10$  nm as highlighted by a red vertical line in Fig. 2.5. Therefore, one can conclude that 6 eV photons allow one to probe a sample thickness of about 10 nm, resulting in a substantial bulk sensitivity of our ARPES technique.

Another reason why our probe photon energy is set at 6 eV is that by using lower photon energies it is possible to reach higher energy and momentum resolution. From Eq. (2.7) and by considering the finite acceptance angle of the electron analyser  $\Delta\theta$ , one finds out that the momentum resolution can be expressed as:

$$\Delta\mathbf{k}_{\parallel} \approx \sqrt{2mE_{kin}/\hbar^2} \cdot \cos\theta \cdot \Delta\theta, \quad (2.13)$$

where the finite energy resolution was neglected. Lower photon energy implies lower  $E_{kin}$ , which in turn determines  $\Delta\mathbf{k}_{\parallel}$ .

Another advantage of working at low photon energy is that the photon momentum  $k_{ph} = 2\pi/\lambda$  can be neglected in Eq. (2.7). As an example, let us consider an ARPES measurement on bulk Al sample. This material is characterized by a fcc crystallographic structure and its lattice parameter is around 0.40 nm, implying a BZ size of  $\frac{4\pi}{a} \approx 3.1 \text{ \AA}^{-1}$ ; on the other hand, our 6 eV UV beam used for photoelectron generation carries a momentum of  $\approx 0.003 \text{ \AA}^{-1}$ , which corresponds to  $\approx 0.1 \%$  of the Al BZ width. Therefore, the photon momentum is negligible and only vertical transitions are involved. This means that the initial and final states have the same crystal momentum. Nevertheless, our future plan is to realize a high-energy ARPES setup that requires some effort and expense in order to investigate

bulk states of strongly correlated systems.

## 2.2.4 Many-body concepts used in ARPES

The most commonly used method to deal with photoemission on solids, and in particular on strongly-correlated materials with many  $|c_{m,i}|^2$  in Eq. (2.12) different from zero, is the *Green's function formalism*, developed within quantum field theory. This formalism is not only notably useful to resolve many-body problems but also allows one to retrieve all the relevant information about the investigated system. First of all, let us consider the one-particle spectral function for the direct photoemission  $A(\mathbf{k}, E_B)$  (i.e., the one-electron removal process) which is a fundamental quantity in many-body physics providing energy and momentum space information about the occupied and unoccupied single-particle states. It is possible to demonstrate that this function can be expressed as [74]:

$$A(\mathbf{k}, E_B) = \sum_m |\langle \psi_m^{N-1} | c_{\mathbf{k}}^- | \psi_i^N \rangle|^2 \delta(E_B - E_m^{N-1} + E_i^N), \quad (2.14)$$

where  $E_B$  is the binding energy of an electron with respect to the Fermi level and  $c_{\mathbf{k}}^- = c_{\mathbf{k}\sigma}^-$  is the annihilation operator for an electron with momentum  $\mathbf{k}$  and spin  $\sigma$ . The spectral function  $A(\mathbf{k}, E_B)$  is related to the imaginary part of the Fourier transform of the time-ordered one-electron Green's function  $G(t - t')$ , which is the probability amplitude that an electron excited in a Bloch state with momentum  $\mathbf{k}$  at zero time will remain in that state after a time  $|t - t'|$  [74], namely  $A(\mathbf{k}, E_B) = (1/\pi) \text{Im}[G(\mathbf{k}, E_B)]$ . From the one-particle spectral function  $A(\mathbf{k}, E_B)$  one can extract information about the quasi-particle self-energy which is affected by the band structure and correlation effects. The concept of quasi-particle, one of the most important in condensed matter physics, allows one to simplify quantum mechanical many-body problems: it consists in treating electrons and associated excitations as a single entity. In particular, when referring to quasi-particles, the expression “dressed-particles” is also used in order to indicate explicitly that they are particles “dressed” by interactions (electron-electron, electron-phonon, ...). Under the framework of the sudden approximation and within the three-step model, the photoemission intensity detected in an ARPES experiment can be expressed as

$$I(\mathbf{k}, E_B) = I_0(\mathbf{k}, \nu) f(E_B, T) A(\mathbf{k}, E_B). \quad (2.15)$$

Here,  $I_0(\mathbf{k}, \nu)$  is proportional to the squared matrix element  $|M_{f,i}^{\mathbf{k}}|^2$  and depends both on the electron momentum and the properties of the photon as frequency and polarization.  $f(E_B, T)$  is the Fermi-Dirac distribution ( $f(\omega) = (e^{\hbar\omega/k_B T} + 1)^{-1}$ ) which takes into account finite-temperature effects [74, 80].

In order to involve the effects of electron-electron correlations, the electron *proper*

*self-energy*  $\Sigma(\mathbf{k}, E_B) = \Sigma'(\mathbf{k}, E_B) + i\Sigma''(\mathbf{k}, E_B)$  is introduced. Let us now consider an electron with band energy  $\epsilon_{\mathbf{k}}$  and momentum  $\mathbf{k}$  which propagates in a many-body system: the real part  $\Sigma'(\mathbf{k}, E_B)$  accounts for the energy renormalization, namely the variations of the measured electron band energy with respect to the non-interacting energy dispersion  $\epsilon_{\mathbf{k}}$ , while the imaginary part  $\Sigma''(\mathbf{k}, E_B)$  contains information about lifetime of quasi-particles. The expressions of the Green's and spectral functions in relation to the self-energy are

$$G(\mathbf{k}, E_B) = \frac{1}{E_B - \epsilon_{\mathbf{k}} - \Sigma(\mathbf{k}, E_B)} \quad (2.16)$$

$$A(\mathbf{k}, E_B) = -\frac{1}{\pi} \frac{\Sigma''(\mathbf{k}, E_B)}{[E_B - \epsilon_{\mathbf{k}} - \Sigma'(\mathbf{k}, E_B)]^2 + [\Sigma''(\mathbf{k}, E_B)]^2}. \quad (2.17)$$

A procedure commonly employed to infer the self-energy information from ARPES data is founded on the momentum distribution curves (MDCs), which are curves obtained by cutting the photoemission map (binding energy vs momentum) at constant energies. This approach consists in assuming a negligible momentum dependence of the self-energy ( $\Sigma(\mathbf{k}, E_B) \rightarrow \Sigma(E_B)$ ): under this hypothesis, one can demonstrate that the shape of a MDC is Lorentzian and the interacting spectral function, for a fixed energy  $E_B = \bar{E}_B$ , becomes:

$$A_{\bar{E}_B}(\mathbf{k}) \propto \frac{\Delta k_p}{(k - k_p)^2 + (\Delta k_p)^2}. \quad (2.18)$$

Here,  $\Delta k_p$  is the half-width at the half maximum of the Lorentzian and  $k_p$  is the Lorentzian peak position. The width of the Lorentzian is proved to be related to  $\Sigma''(\mathbf{k}, E_B)$  and it is inversely proportional to the dressed-electron life-time. To be more quantitative, the real and imaginary parts of the self-energy can be expressed in terms of the group velocity for non-interacting electrons at  $k_p$ , i.e.,

$$\Sigma'(\mathbf{k}, E_B) = \bar{E}_B - \epsilon_{k_p}, \quad (2.19)$$

$$\Sigma''(\mathbf{k}, E_B) = -\hbar \Delta k_p v_{k_p}. \quad (2.20)$$

## 2.3 Time- and Angle-Resolved Photoemission Spectroscopy (TR-ARPES)

Angle-resolved photoemission spectroscopy enables one to acquire energy and momentum information about the electronic band structure of a material in thermal equilibrium. Nevertheless, ARPES is still limited by a few factors: *i*) the measurable electronic states are only those initially occupied; *ii*) it does not provide a

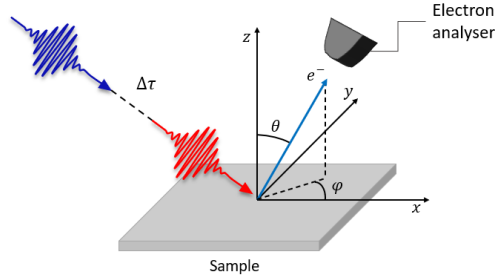


**Figure 2.6.** Illustration of the photoemission process in TR-ARPES. The pump pulse (red) perturbs the electronic distribution of the sample and then, after a time delay  $\Delta\tau$ , the probe pulse (blue) causes photoemission.

direct access to the electronic dynamics at the timescale of elementary electronic processes. These impediments can be overcome by incorporating pump-probe techniques, where the sample under investigation is shined by two femtosecond light pulses in short succession. One of these, designated as the “pump”, in general infrared in frequency, drives the material into a non-equilibrium state without producing photoemitted electrons. The other one, called “probe”, is a time-delayed pulse that supplies a photon energy typically within the ultraviolet ( $\approx 6$  eV) or extreme-ultraviolet ( $\approx 10$ -60 eV) frequency range for the photoemission process. Several research groups have been working on time- and angle-resolved photoemission spectroscopy (usually indicated by time-resolved ARPES, tr-ARPES or pump-probe ARPES) which has paved the way for the study of electronic dynamics and different non-equilibrium phenomena of various materials as unconventional superconductors, *e.g.* cuprates [81–83], charge density wave systems [6, 84, 85], topological insulators [86, 87], transition metal dichalcogenides [88, 89] and other solid-state systems [90].

A typical time-resolved ARPES (TR-ARPES) experiment is schematically depicted in Fig. 2.6. By changing the time delay between the two ultrashort pulses, one can study the time-dependent processes taking place during the relaxation of the sample from the pump-induced non-equilibrium electronic state with sub-picosecond resolution. Therefore, TR-ARPES enables mapping the transient changes of the electronic structure as a function of electron kinetic energy, electron momentum and time-delay between pump and probe pulses, extending standard ARPES.

### 2.3.1 Experimental setup

The TR-ARPES apparatus used in this work is a table-top setup based on an Ytterbium (Yb) laser source where ultrashort visible pump pulses (30 fs, 1.82 eV) and ultraviolet probe pulses (80 fs, 6.05 eV) are generated by means of non-collinear optical parametric amplification (NOPA) and sum-frequency generation (SFG) [61]. This Yb laser-based experimental system has emerged as an innovative time-resolved photoemission setup among the various TR-ARPES apparatuses which traditionally employ a high-repetition rate cw-pumped, regeneratively amplified Ti:sapphire laser [91, 92]. In the last decade, Yb-doped gain media have proved to be appropriate materials for femtosecond laser systems because of their promising characteristics. Indeed, they present (*i*) long excited states lifetimes, which enable direct diode pumping and the achievement of high repetition rates and (*ii*) low quantum defect, leading to potentially very high power efficiency with low thermal loads, thus guaranteeing a remarkable long-term reliability. The high stability of the Yb-based source along with the use of high repetition rate (100 kHz) enables one to reach elevated signal-to-noise ratio without running into space-charge effects and a shorter acquisition times compared to the ones required in low repetition rate systems [93]. Furthermore, the experimental setup is characterized by a large tunability of the pump pulse in the interval (1.45 - 2) eV and enables the energy-momentum data collection with a temporal and energy resolution of 85 fs and 30 meV, respectively.

The following sections will describe the different parts of the experimental setup, i.e., the optical apparatus for the generation of pump and probe pulses, the ultra-high vacuum (UHV) system and the detection system.

#### A. Optical setup

The laser source of the experimental setup is a regeneratively amplified Yb:KGW system (*Pharos, Light Conversion*) producing a pulse train with an average output power of 10 W (pulse energy stability < 0.5% rms/24 h) and a repetition rate set at 100 kHz (in principle, it can be tuned from 10 kHz to 350 kHz). Each pulse is centered around 1028 nm (1.20 eV) and has a duration of about 290 fs. The resulting energy of the single pulse is 60  $\mu$ J, which is high enough to trigger the nonlinear optical processes required to produce the deep ultraviolet (DUV) probe pulses for photoemission measurements. Table 2.1 summarizes the output characteristics of the Yb-laser source. A scheme of the optical setup for the generation of pump and probe pulses is illustrated in Fig. 2.7. First of all, part of the fundamental frequency (FF) beam is used to power a broadband non-collinear optical amplifier (NOPA) generating pulses centred at 680 nm (1.82 eV) with a duration of 23 fs. The seed of the NOPA system is a white light super-continuum



Central wavelength	$1028 \pm 5$ nm
Average power	10 W
Repetition rate	10-350 kHz
Pulse duration	290 fs
Output pulse stability	< 0.5% rms/24 h

**Table 2.1.** Yb-laser output characteristics.

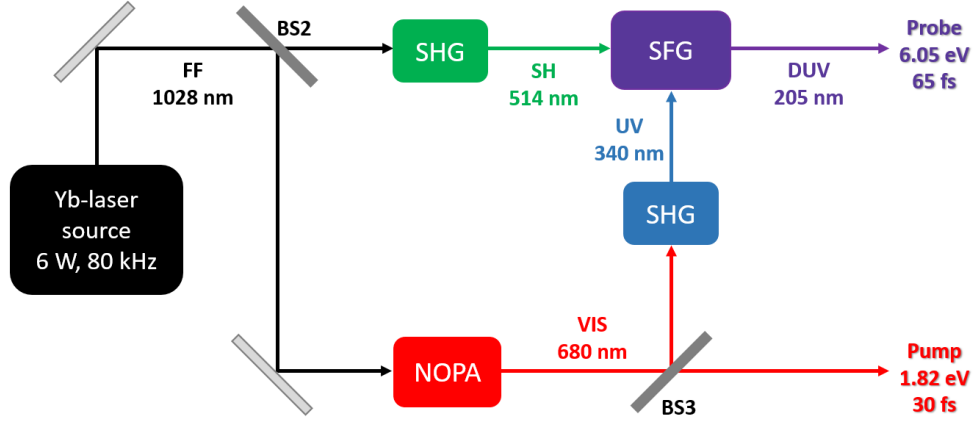


**Figure 2.7.** Schematic representation of the optical system for the generation of pump (1.82 eV, 30 fs) and probe (6.05 eV, 65 fs) pulses. FF: fundamental frequency, SH: second harmonic, UV: ultraviolet, DUV: deep ultraviolet, VIS: visible, SHG: second harmonic generation stage, NOPA: non-collinear optical parametric amplifier, SFG: sum frequency generation stage, BS: beam splitter.

(WLS) generated by a YAG plate, while its pump is given by the second harmonic of the FF, obtained via a  $\beta$ -barium-borate (BBO) crystal. A fraction of this output is directly employed as the pump beam for the TR-ARPES measurements by passing through a dielectric beam-splitter which causes a broadening of the pulse duration up to  $\sim 30$  fs. The residual light takes part to the generation of the DUV probe pulses. For this purpose, the 680-nm pulses are frequency doubled and the resulting 340-nm (3.65 eV) pulsed beam is then combined with the 514-nm (2.4 eV) second harmonic (SH) of the FF beam via sum frequency generation (SFG), thus obtaining the DUV probe pulses centred at 205 nm (6.05 eV) with a nominal duration of 65 fs. Further details on pump and probe pulse generation in TARPES can be found in Ref. [61].

## Additional technical aspects

A typical TR-ARPES experiment consists in using two time-delayed ultra-short pulses in order to investigate the temporal evolution of the electronic population. The relative arrival of pump and probe pulses is controlled by a motorized delay stage with a minimum feasible step size of 3.33 fs, which is much lower than the temporal resolution.

Photoemission measurements occurs in a vacuum chamber with a base pressure of  $\approx 10^{-10}$  mbar (UHV regime) which is crucial for preserving the quality of the sample surface. Pump and probe pulses arrive at the sample placed in the chamber by passing through a 2-mm thick  $\text{MgF}_2$  plate. The latter is characterized by high transmission values at the 680 nm pump wavelength and low dispersion from visible to DUV spectral interval: the resulting temporal width of the DUV probe pulse is estimated to be 75 fs, while the one of the visible pump less than 30 fs. These probe and pump pulse durations determine a pump-probe cross-correlation of about 85 fs full width half maximum (FWHM) [61]. Both the pump and the probe beams are focused on the specimen by a 500-mm focal-length UV-enhanced aluminium concave mirror with the aim of preventing chromatic aberrations and temporal broadening and they impinge on the sample at an angle of  $45^\circ$ .

As concerning the TR-ARPES pump-probe signal, it can be improved by ensuring that the DUV probe investigates a homogeneously excited area of the material. To this purpose, the pump spot size is set to be twice the probe one ( $100 \mu\text{m}$  vs  $50 \mu\text{m}$ ) by means of properly designed telescopes along the optical path of the beams. This configuration is achieved by means of 3:2 and 5:1 telescopes and it guarantees the TR-ARPES signal optimization.

Another important quantity that has to be carefully controlled is the number of photoelectrons extracted from the sample per pulse: electrons propagating in vacuum towards the detection system will repel each other due to their mutual Coulomb interaction and, if the consequential electron cloud is too dense, space-charge effects as broadening and shift of photoemission spectra occur, thus reducing the performance of the technique. In order to prevent such effects, the intensity of the DUV probe beam must be properly monitored. Concurrently, the pump fluence is adjusted by a variable attenuator and ranges from tens of  $\mu\text{J}/\text{cm}^2$  up to  $\text{mJ}/\text{cm}^2$  according to the sample under investigation. Multi-photon excitations are carefully avoided.

## B. Sample conditions and vacuum system

As discussed above, at 6 eV photon energy ARPES is particularly bulk sensitive. However, the condition of the sample surface is crucial: oxidation, defects and contamination can strongly alter the photoemission yield and also induce multi

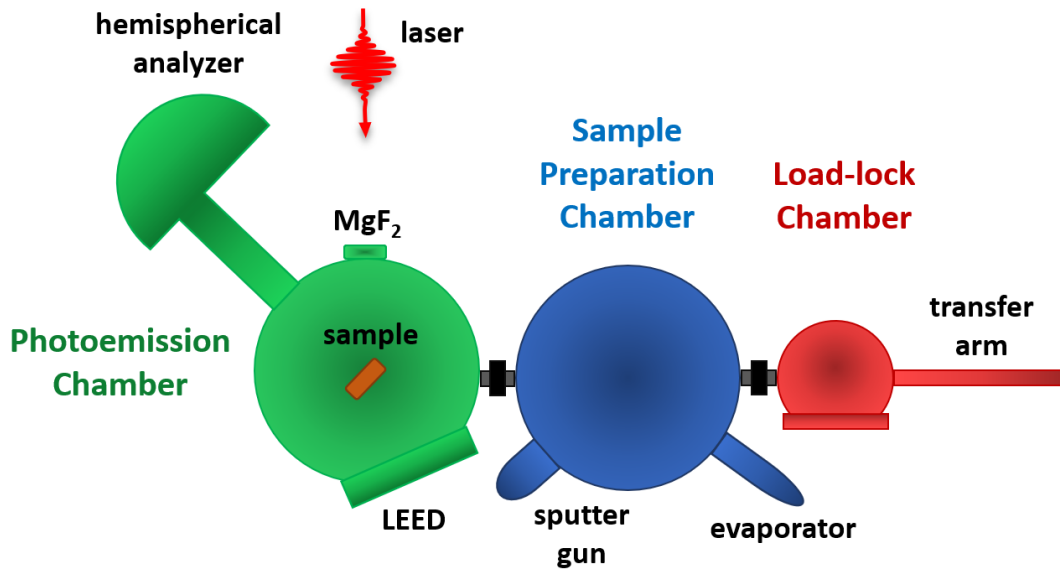


**Figure 2.8.** Schematic representation of the UHV system, according to Ref. [4]. The setup is made up of three chambers separated by two vacuum valves: the load-lock chamber with a transfer arm (red), the sample preparation chamber including a couple of evaporators, an  $\text{Ar}^+$  sputter gun and a LEED system (navy), and the photoemission chamber directly connected with the hemispherical analyzer for the detection (green).

photon processes from the pump. For this reason, PES measurements are always carried out in UHV conditions and samples are cleaved *in-situ* before each measurement in order to analyze an uncontaminated surface. Finally, the samples are attached to a sample holder by means of conductive silver paint and they can be subject to a bias voltage.

An illustration of the UHV system is schematically depicted in Fig. 2.8. The latter is formed by three chambers divided by two vacuum valves:

- the *load-lock chamber* is a vacuum chamber used for loading the sample under investigation from ambient pressure conditions into the main vacuum chamber where photoemission will take place. The sample enters the chamber via a fast entry port and is moved from one chamber to the other by a transfer arm;
- the *sample preparation chamber* includes evaporation cells which enable the process of thin film deposition, a low energy electron diffraction (LEED) system, which documents *in-situ* the long range ordering and the crystallo-

graphic structure of the sample an  $\text{Ar}^+$  sputter gun. Since the temperature of the sample holder can be increased up to 1000 K, there is also the possibility to carry out sputtering-annealing cycles; inside the preparation chamber, Cs deposition is also carried out with a SAES Getters dispenser. In order to keep a pressure of  $\sim 10^{-9}$  mbar during Cs deposition, the current through the dispenser ( $\sim 5$  A) is suitably modified.

- the *photoemission chamber*, where the sample is placed during the TR-ARPES measurements. It is made up of  $\mu$ -metal in order to shield the region where the extracted electrons propagate from external magnetic fields. Inside the photoemission chamber a low energy electron diffraction (LEED) system, which documents *in-situ* the long range ordering and the crystallographic structure of the sample, is also present. The sample holder is fixed on the cold head of a cryostat by which measurements in the temperature range from 10 K to 500 K can be executed. As regarding the manipulation of the sample, translations along the three  $x$ ,  $y$  and  $z$  axes, tilt and rotation can be performed in order to adjust the sample position in relation to the pump/probe direction.

Each chamber is pumped independently by turbomolecular pumps and during the sample preparation and measurement the pressure is maintained in the  $10^{-10}$  mbar range.

### C. Detection system

The photoelectron spectrometer used in this work for detecting and analysing the electrons extracted from the sample is a *hemispherical energy analyzer*. Fig. 2.9 shows a photo of our setup where the photoemission chamber and the hemispherical energy analyzer are clearly visible. The main task of this instrument is to disperse photoelectrons as a function of their kinetic energy, allowing angle resolved analysis. A typical hemispherical analyzer is schematically shown in 2.10. The device consists of two concentric hemispherical electrodes of radii  $R_1$  (the inner hemisphere) and  $R_2$  (the outer hemisphere), with a mean radius  $R_0=(R_1+R_2)/2$  and set at appropriate potentials. The operation of the analyzer can be summarized as follows:

1. electrons coming from the sample surface with a wide angular distribution enter a lens system;
2. the lens system focuses photoelectrons in order that they are able to reach an energy filter;

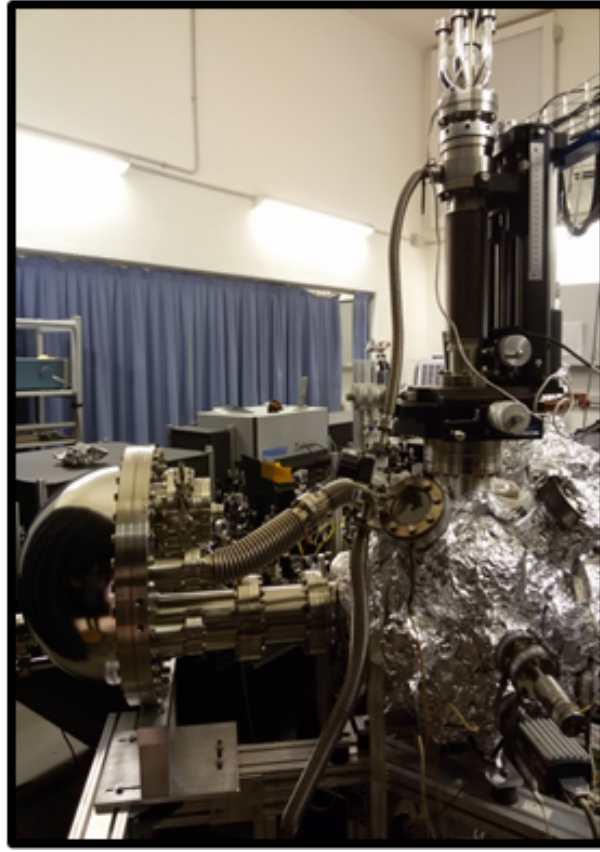


**Figure 2.9.** Photo of our setup. The photoemission chamber and the hemispherical energy analyzer are in the foreground.

3. the entrance slit, placed before the energy filter, allows only the passage of a part of the electrons, determining the energy resolution. Wider slits imply higher intensity but lower energy resolution, while narrower slits entail fewer electrons but higher resolution;
4. the two biased hemispherical electrodes shall ensure that only electrons with energies around the so-called *pass energy*,  $E_p$  [94], move through the filter. In this way, electrons are dispersed depending on their energies: low energy electrons (red) will shift towards the inner hemisphere, electrons at  $E_p$  will follow the trajectory (green) at the centre of the filter and high energy electrons (blue) will move towards the outer hemisphere;
5. at the output, there is another slit which further constrains the number of electrons;
6. electrons that pass through the exit slit are detected by a microchannel plate

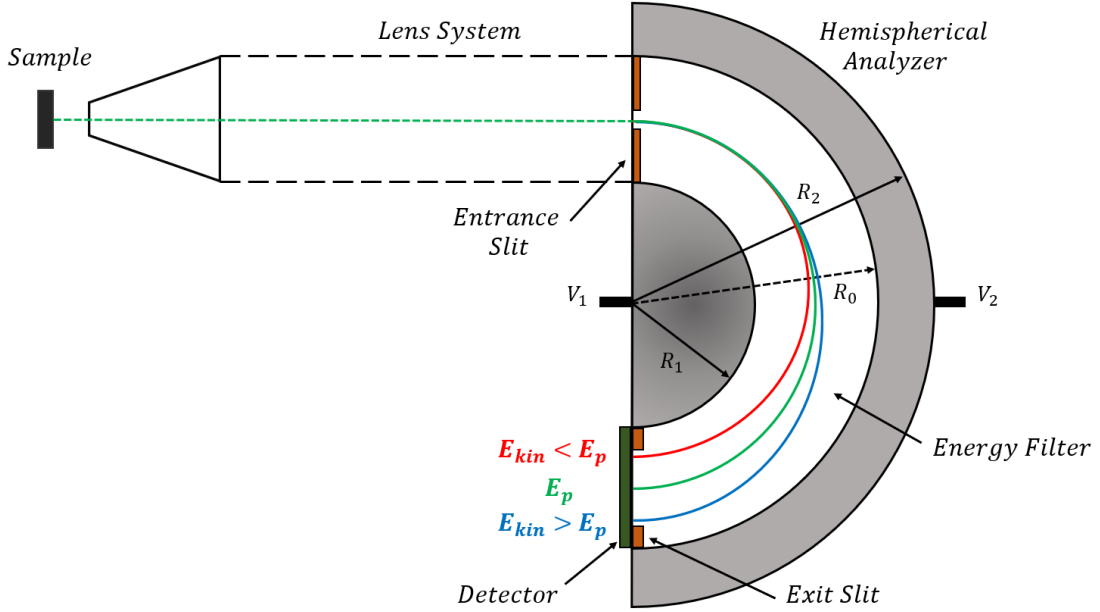


**Figure 2.10.** Sketch of the hemispherical energy analyzer used in our TR-ARPES setup for the detection of photoelectrons. A lens system focuses electrons which come from the sample with a large angular distribution. Subsequently, the electrons enter an energy filter by an entrance slit whose aperture determines the energy resolution. Two biased hemispherical electrodes of radii  $R_1$  and  $R_2$  ( $R_1 < R_2$ ) disperse electrons as a function of their kinetic energy: electrons at the pass energy  $E_p$  follow the central trajectory (green), electrons with  $E_{kin} < E_p$  move towards the inner hemisphere (red), electrons with  $E_{kin} > E_p$  move towards the outer hemisphere (blue). After crossing an exit slit limiting their number, the dispersed electrons go into a CCD detector, which provides an energy-momentum map.

(MCP), which is followed by a Charge-Coupled Device (CCD).

If  $V_1$  and  $V_2$  are the electric potential applied to the inner and outer hemispheres, respectively, where  $V_1 > V_2$ , one can demonstrate that the radial dependence of the potential  $V(r)$  in the area contained between the two hemispheres is given by:

$$V(r) = - \left[ \frac{V_2 - V_1}{R_2 - R_1} \right] \cdot \frac{R_1 R_2}{r} + Const. \quad (2.21)$$

The electric field related to this potential in the same region points from the center outwards along radial direction and has the following expression:

$$|\mathbf{E}(r)| = - \left[ \frac{V_2 - V_1}{R_2 - R_1} \right] \cdot \frac{R_1 R_2}{r^2}, \quad (2.22)$$

which gives rise to the centripetal force  $-e\mathbf{E}(r)$ . For an established electrical field gradient, only electrons with kinetic energies in a certain energy range can move through the entire deflection angle from the entrance slit to the exit plane. In particular, electrons which arrive normal to the entrance slit and following the central circular trajectory, have the pass energy  $E_p$  given by:

$$E_p = -q \cdot k \cdot \Delta V, \quad (2.23)$$

where  $q$  is the electron charge,  $\Delta V$  is the voltage applied to the hemispherical surfaces and  $k$  is the calibration constant:

$$k = \frac{R_1 R_2}{2R_0(R_2 - R_1)}. \quad (2.24)$$

In our work, we use a *SPECS PHOIBOS 100* 2D hemispherical analyzer operating with a 2D CCD detector which simultaneously records the kinetic energy and the angular dependence of photoelectrons up to  $\pm 15^\circ$  acceptance angle. In comparison to other detectors, such as the time-of-light (ToF) spectrometer [4], the hemispherical analyzer offers the possibility to acquire multiple emission angles avoiding long experiment times because the whole electron dispersion can be measured in a single scan at each pump-probe time delay.

### 2.3.2 Other TR-ARPES experimental setups

Besides ours, there are also other TR-ARPES setups which are based on different instruments [91]. First of all, there exist setups based on solid-state lasers, which generate pulsed UV radiation by exploiting second-harmonic generation (SHG) and/or sum-frequency generation (SFG) processes in nonlinear media [4, 92, 95]. These systems, at the *smallest scale*, exhibit several advantages as lower costs for operating and maintenance, higher momentum resolution and the possibility to study carefully the electron dynamics around the  $\Gamma$  point of the first Brillouin zone (BZ). The main drawback of these TR-ARPES investigations originates from the transparency of the employed crystal, which determines the highest photon energy obtainable. For instance, the greatest photon energy reachable via SHG in a  $\beta$ -barium borate (BBO) crystal is 6.05 eV because of its absorption edge of 6.56 eV [70]. Therefore, as can be deduced by inspecting Eqs. (2.6) and (2.7), the interval of accessible momentum values in the reciprocal space is restricted. Since for several materials the dynamics of electrons located near the edge of the BZ, inaccessible using this method, plays an important role, there has been a growing request for TR-ARPES setups with probe photon energies greater than  $h\nu = 7$  eV [70, 96]. This demand has led to the development of a second class of TR-ARPES systems based on high-harmonic generation (HHG), which give the

ability to study the entire BZ. HHG is a nonlinear process which usually occurs by focusing an ultrafast laser light with intensities of the order of  $10^{14}$  W/cm<sup>2</sup> or higher into an atomic gas [97]: under these conditions, a small fraction of the laser power can be converted into higher harmonics, covering a wavelength range from the vacuum ultraviolet to the soft X-ray region. The required high pulse powers are achieved by using low repetition rate sources at price of lower signal-to noise ratios [98, 99]. Therefore, the crucial point is to put together high photon energy with high photoemission count rates and narrow bandwidth, required to reach a high energy resolution without altering the temporal one and, recently, only a few research groups as the ones of Peli et al. [100], Berntsen et al. [101], He et al. [102] and Zong et al. [103] have been working on these experimental improvements. Besides these examples of table-top setups, there are TR-ARPES setups which includes instruments at the largest scale. They are free-electron lasers (FELs) which enable the generation of femtosecond pulses in an energy range extending from 10 eV to 1000 eV. In comparison with smaller-scale systems, TR-ARPES via FEL sources can achieve not only variable photon energy and mutable pulse duration but also a Fourier transform-limited energy resolution and a large interval of momenta.

## 2.4 Time-Resolved Reflectivity (TRR)

Time-resolved reflectivity (TRR) is a technique used to determine non-equilibrium properties of correlated electron systems by the measurement of time-dependent quantities [104, 105]. As all the time-resolved spectroscopy techniques, TRR also exploits the *pump-probe scheme*, whereby the material under investigation is excited by the pump pulse and its subsequent temporal evolution is tracked by the time-delayed probe pulse. In TRR the information about the non-equilibrium dynamics is obtained by collecting the reflected photons and by measuring the change in the reflected probe intensity over the absolute value, i.e.  $\Delta R/R$ . The power of the technique is due to the fact that the reflectivity variations of the sample are related to its electronic properties in the pump-induced excited state and to its subsequent relaxation to the ground state, which is mediated by different interactions and processes.

### 2.4.1 Introduction

TRR records photo-induced changes of the sample reflectivity ( $\Delta R$ ) which are the result of the variation of real and imaginary parts of dielectric function  $\epsilon(\omega) =$



$\epsilon'(\omega) + i\epsilon''(\omega)$  [106], where  $\omega$  is the frequency of the probe. In addition to  $\epsilon(\omega)$ ,  $R(\omega)$  depends on the experimental geometry and the beam polarization which are held constant during the measurements. As a consequence of pump-induced modifications, there is a variation of the dielectric function and, in turn, of the TRR signal. Supposing a linear response and invoking a simple first-order perturbation approach, the transient reflectivity signal  $\Delta R(t)$  can be expressed in terms of the pump-induced modifications of carrier density in excited bands ( $n_e$ ), the electronic temperature ( $T_e$ ) and lattice coordinate ( $q$ ), through the dielectric function, as follows [107, 108]:

$$\Delta R(t) = \frac{\partial R}{\partial \epsilon} \frac{\partial \epsilon}{\partial n_e} n_e(t) + \frac{\partial R}{\partial \epsilon} \frac{\partial \epsilon}{\partial T_e} T_e(t) + \frac{\partial R}{\partial \epsilon} \frac{\partial \epsilon}{\partial q} q(t). \quad (2.25)$$

In order to estimate  $\Delta R(t)$ , it is necessary to know the function  $\epsilon(n_e, T_e, q)$ , which is generally unknown. However, according to Eq. (2.25), by means of TRR experiments, it is possible to retrieve important information about electron dynamics [12, 109], electron-phonon coupling strength [13, 110] and the atomic motions [14].

## 2.4.2 Experimental setup

The TRR experimental setup used for this work is described in detail in Ref. [104]. Here, we summarize its main features. The laser source is a Ti:sapphire laser (*Libra, Coherent*) delivering pulses at 2 kHz repetition rate with 790 nm center wavelength and 100 fs duration. The laser beam is used to pump two independent non-collinear parametric amplifiers (NOPAs) which produce the pump and probe beams. Both NOPAs are pumped by the second harmonic of the Ti:sapphire laser generated by a 1 mm-thick lithium triborate crystal (LBO). The signal of each NOPA is a white light continuum generated in 1 mm-thick sapphire crystal. Pump and signal are focused on a 1-mm-thick  $\beta$ -barium borate (BBO) crystal where the parametric gain is reached with an internal angle  $\alpha$  equal to  $3.82^\circ$ . Each NOPA generates pulses with a 500-720 nm spectral range and are compressed to  $\approx 20$  fs by means of chirp mirrors. A spherical mirror is used to focus both pump and probe beams on the sample in order to avoid additional chirping. A mechanical delay line is employed to change the time delay between pump and probe and the pulse train of the pump is modulated at 1 kHz by a mechanical chopper. As concerning the detection, the reflected probe pulses are detected by a Si photodetector array working at 2 kHz (i.e., the repetition rate of the laser source).

## 2.5 Conclusions

In this Chapter the experimental techniques used in this work, i.e. time- and -angle resolved photoemission spectroscopy and time-resolved reflectivity, were described. Firstly, a theoretical overview about angle-resolved photoemission spectroscopy was presented together with an illustration of the three-step model and many-body effects. Subsequently, our Yb-based TR-ARPES setup enabling one to acquire energy and momentum information about the electronic band structure of matter was described. Lastly, the time-resolved reflectivity setup which can be used to determine non-equilibrium properties of correlated electron systems was presented.

# Chapter 3

## Electron Dynamics in Black Phosphorus

### 3.1 Introduction

The synthesis of graphene in 2004 [111] spawned a new class of atomically thin materials which is nowadays known as two-dimensional (2D) crystals. The number of materials in this class has been constantly increasing ever since to include transition metal dichalcogenides, hexagonal boron nitride and several 2D allotropes (phosphorene, stanene, germanene) [112]. They all share the common feature of being layered structures, bound by van der Waals forces, which can eventually be thinned down to a single layer. Owing to their peculiar two-dimensional character, they display a pronounced dependence on the thickness, providing a mean to tune and engineer their electrical and optical properties. Among them, black phosphorus (BP) is a striking example of such peculiarity and it has lately attracted great interest [21, 113]. This material is a layered semiconductor which exhibits high carrier mobility (up to  $\sim 10^4 \text{ cm}^2\text{V}^{-1}\text{s}^{-1}$  in the monolayer (1D) [114]), anisotropic optical/electronic response (DC conductance and reflectance vary by a factor  $\sim 2 - 4$  with in-plane orientation) [19, 115] and outstanding mechanical properties (1L-BP can be subjected to a tensile stress up to  $\sim 30\%$ ) [116]. BP has a direct bandgap which depends on the number of layers and ranges from  $\sim 0.4 \text{ eV}$  in the bulk [5] to  $\sim 2 \text{ eV}$  in the monolayer system, called phosphorene [117], with strong sensitivity to pressure, external field and in-plane strain [118–120]. It has been recently observed that surface doping by alkali atoms allows a wide and continuous tunability of the bandgap, leading to a surface band inversion at sufficiently high dopant concentration, namely  $\sim 0.35 \text{ 1L} \sim 9 \times 10^{13} \text{ cm}^{-2}$  [15, 16, 121]. This exceptional modulation of the gap is ascribed to the so-called giant Stark effect [122], i.e. an electric field-induced shift of the electronic states and it has been

theoretically supported by density function theory [16, 123] and tight binding calculations [121, 124]. A common feature identified by all computational methods is the strong, alkali-induced electrons re-distribution, in particular surface depletion at the valence band (VB) maximum and surface confinement of the conduction band (CB). The latter has been experimentally confirmed by angle-resolved photoemission spectroscopy (ARPES) with variable photon energy [121], suggesting the inherent surface character of the CB in alkali-doped BP. Lately, time-resolved ARPES (TR-ARPES) investigations on BP have explored the transient electronic dynamics in the sub-ns time window: a power-law carrier recovery has been considered as the possible fingerprint of exciton formation [125], while the role of photo-induced band broadening and ionized surface impurities on the carrier dynamics has been discussed, but no significant bandgap renormalization (BGR) has been found [22]. On the other hand, a pump-induced shift of the VB has been recently recognized as the signature of BGR and has been supported by *ab initio* calculations [23], in agreement with resonant transient absorption measurements [126]. In order to shed light on these controversial aspects and understand the ultrafast non-equilibrium response of BP, we employ TR-ARPES to investigate bulk BP in its pristine state and after surface doping by Cs atoms. The Cs doping amount is proportional to the deposition time and its estimation is obtained by comparing the resulting bandgap with the data in Ref. [15]. The latter states that a deposition time of 45 s corresponds to the critical doping dose of  $\sim 0.35$  1L Cs, which leads to the closure of the gap. In the pristine sample, the injected photo-carriers (electron-hole pairs) thermalize within several picoseconds and induce a band broadening, in agreement with previous studies. However, based on the comparison with surface-doped BP, we attribute the observed broadening to carriers drift-diffusion processes, and not to Stark-related effects [22]. Furthermore, our VB dynamics reveals a  $\sim 50$  meV BGR entwined to a transient VB flattening that we ascribe to the Pauli blocking. After Cs deposition, a more intriguing phenomenology arises: pump photons trigger a long-lived (ns) surface photovoltage (SPV) of a few hundreds mV that compensates the Cs-induced surface band bending. This fact allows us to investigate the mechanism underlying the band inversion and to disentangle bulk from surface electronic states in bulk samples.

## 3.2 Sample Properties

Under ambient conditions, BP crystallizes in the orthorhombic structure where  $sp^3$  orbital hybridization leads to buckled layers normal to the  $z$ -axis, as shown in Fig. 3.1(a), held together by van der Waals forces. The sample surface is normal to the  $z$ -axis and standard mechanical exfoliation by tape can be repeatably performed to expose a clean surface layer. Fig. 3.1(b) displays the first Brillouin Zone (BZ) of

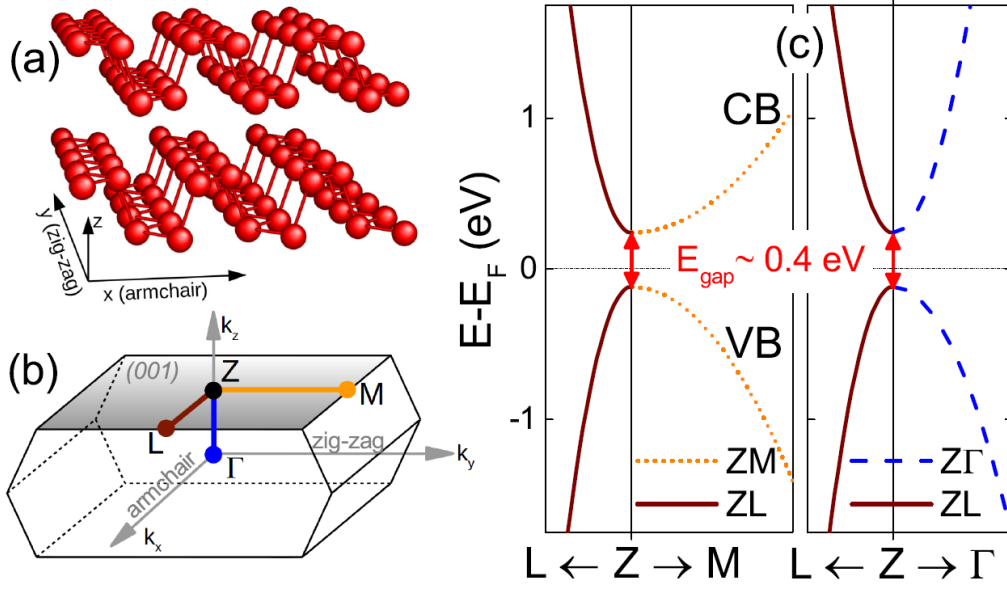


**Figure 3.1.** Atomic and electronic structure of BP from Ref. [1]. (a) BP crystal structure. Each phosphorene layer, normal to the  $z$ -axis, is buckled along the  $x$ -axis (armchair direction). (b) First Brillouin Zone (BZ) of bulk BP. The direct bandgap is located at the Z-point. (c) Schematic electronic band structure around the Z-point: band dispersions along the three main axes are estimated from the effective masses reported in Ref. [5].

bulk BP. Here, the direct bandgap is placed at the Z-point of BZ as shown in Fig. 3.1(c) where the strongly anisotropic band dispersion can be clearly seen. On the left panel in Fig. 3.1(c) electronic bands along the  $x$ -axis (armchair direction) and the  $y$ -axis (zig-zag direction) are reported: electron/hole effective masses vary from  $\sim 0.08 m_0$  along the armchair direction to  $\sim 1 m_0$  along the zig-zag direction [5]. This large in-plane anisotropy results in peculiar electronic [127], optical [128] and thermal [129] behaviors. We focus the following analysis on the armchair direction where the band dispersion is largest. However, since we examine the region around the Z symmetry point, our results about band dynamics are not influenced by the in-plane crystallographic orientation.

### 3.3 TR-ARPES on Pristine BP

TR-ARPES measurements are performed with the setup described in Chapter 2. All data are acquired at room temperature (RT) after establishing the in-plane crystallographic orientation of the sample by Low Energy Electron Diffraction (LEED). The ARPES map of bulk BP measured along the armchair direction at

positive pump-probe delay  $\sim +2.4$  ps is reported in Fig. 3.2(a). The map clearly shows the VB, which is completely below the Fermi level  $E_F$ , and the ordinarily unoccupied CB above  $E_F$ . In order to highlight the photo-induced effects in BP, the photoemission spectrum recorded at negative delay, i.e. before pump arrival, is subtracted from ARPES spectra at two selected pump-probe delays. The resulting differential ARPES maps at  $+50$  fs and  $+2.4$  ps are shown in Fig. 3.2(b), where the photo-induced enhancement of spectral weight is indicated by red color while the electron depletion by blue color. The dynamics of band extrema and band sides

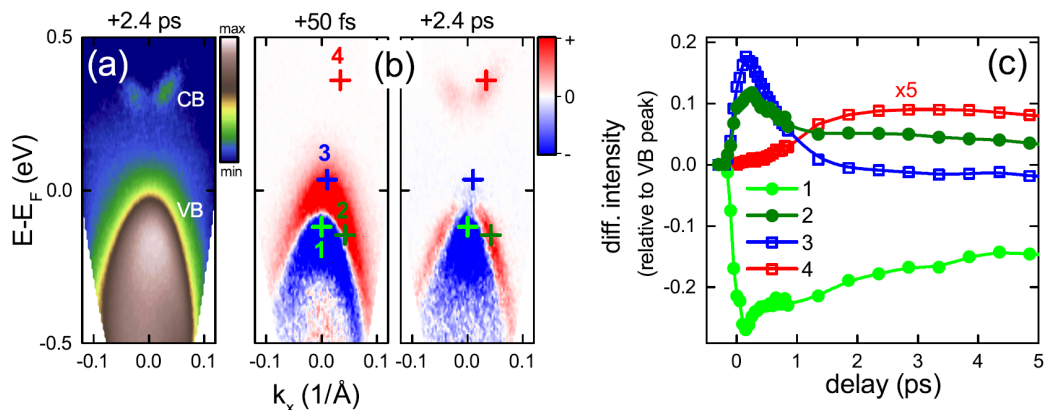


**Figure 3.2.** (a) ARPES map of bulk BP along the armchair direction at pump-probe delay  $+2.4$  ps from Ref. [1]. As a consequence of the optical pumping the CB is also populated. (b) Differential spectra at two fixed delays, i.e.  $+50$  fs and  $+2.4$  ps, where red indicates enhancement, whereas blue is depletion. The crosses labeled 1 to 4 mark spectral features whose dynamics is reported in panel (c).

is examined in Fig. 3.2(c). The latter shows the temporal evolution of selected points of the energy-momentum map, which are marked by the four crosses in Fig. 3.2(b). The VB dynamics is traced by light green, dark green and blue lines (labels 1-3): in all three cases, a fast ( $< 100$  fs) response to pump pulses can be recognized. On the contrary, the temporal evolution of the CB (label 4), indicated by the red lines, is characterized by a slow build-up on the ps scale. This result suggests that CB is indirectly occupied. Indeed, electrons are first excited from the VB to higher levels of the CB by the pump pulse and then they decay towards the bottom of the CB via electron-electron and electron-phonon scattering processes. Because of the presence of a bandgap, the increased intensity on the VB upper border (crosses 2,3) can be attributed to photo-induced broadening and/or shift of the band edge. More precisely, this increase lasts longer on the VB sides (cross 2) with respect to the VB center (cross 3).

Although our results line up with earlier TR-ARPES studies on BP [22, 23, 125], two issues were not unambiguously clarified to date: VB broadening and BGR.

The zoom-in of the VB ARPES map at + 2.4 ps delay is reported in Fig. 3.3(a). We normalize the energy distribution curves (EDCs) to their maxima in order to highlight the band shape. Subsequently, we estimate the band dispersion, which is shown by open red symbols, through a fitting procedure described in Paragraph 3.4.1. This allowed us to retrieve the temporal evolution of the VB structure. The

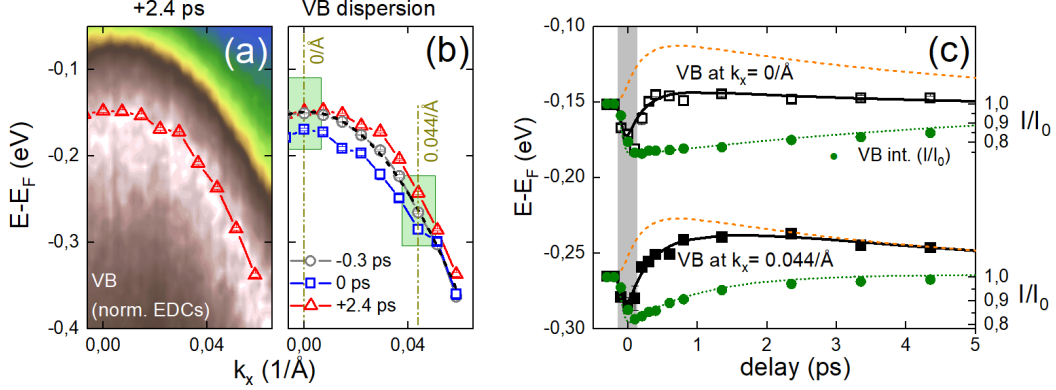


**Figure 3.3.** Analysis of the VB dispersion from Ref. [1]. (a) Zoom-in of the VB ARPES map at + 2.4 ps delay. EDCs are normalized to their maxima. The open symbols indicate the fitted band dispersions (see Paragraph 3.4.1). (b) Comparison of VB dispersions at -0.3 ps (circles), 0 ps (squares) and +2.4 ps (triangles) delays. A parabolic fit is indicated by the black dashed line. (c) VB temporal evolution at  $k_x = 0 \text{ \AA}^{-1}$  (open squares) and  $k_x = 0.044 \text{ \AA}^{-1}$  (solid squares). Lines are found via a phenomenological fit. Green solid circles are obtained by integrating the VB spectral intensities in the rectangular areas of Panel (b). The vertical axis on the right-hand-side shows the relative intensity  $I/I_0$ , normalized to  $I_0$  at negative delay. The pump fluence is kept at  $0.4 \text{ mJ/cm}^2$ .

resulting VB dispersions at -0.3 ps (circles), 0 ps (squares) and +2.4 ps (triangles) delays are shown in Fig. 3.3(b). The comparison clearly shows the presence of a dynamics in the valence band after photo-excitation. By comparing the grey and blue dispersion curves, i.e. the VB dispersions at -0.3 ps and 0 ps respectively, it is evident that, at 0 delay, there is a pump-induced  $\sim 20 \text{ meV}$  downward shift of the whole VB. Then, after +2.4 ps, by looking at the red dispersion curve, we can recognize a reduction of the band curvature, indicating an increased hole effective mass. The latter result is in agreement with the long-lasting spectral increase at the VB sides in Fig. 3.2(b) (cross 2). Furthermore, notice that only the VB dispersion at negative pump-probe delay can be fitted by a simple parabola (black dashed line), obtaining a hole effective mass  $m_{VB} \sim 0.065 m_0$  ( $m_0$  being the free electron mass) in accordance with the literature [5, 22]. This result implies

two possible scenarios: (i) flattening of the top VB (for  $k_x < 0.03 \text{ \AA}^{-1}$ ), rather than an enlargement of effective mass, which causes a deviation from the parabolic shape, especially noticeable at positive delay; (ii) pump-induced upward shift of  $\sim 50 \text{ meV}$  of the VB toward  $E_F$ , hint of BGR [130, 131]. On the top of the VB, the flattening and the BGR counterbalance each other. Further information can be derived by the dynamics in Fig. 3.3(c): the temporal evolution of the VB at  $k_x = 0 \text{ \AA}^{-1}$  is indicated by open symbols while the one at  $k_x = 0.044 \text{ \AA}^{-1}$  is represented by solid squares (the associated dash-dotted vertical lines can be seen in Fig. 3.3(b)). As we can see, the two curves cannot be reproduced by a single-component model. However, we found that they can both be reproduced by means of a phenomenological model based on two contributions, labeled C1 and C2. The positive component C1, indicated by the orange dashed lines, represents a shift in energy of the whole VB towards the Fermi level  $E_F$  as a signature of a BGR (see Paragraph 1.2.2). This phenomenon is independent of  $k_x$  and the fit reveals that it has a maximum amplitude of  $\sim 47 \pm 5 \text{ meV}$ , a rise time of  $\sim 280 \pm 100 \text{ fs}$  and a decay time of  $\sim 4.8 \pm 0.8 \text{ ps}$ . Green dotted lines represent the second negative component C2 which is  $k_x$ -dependent. Indeed, in this case, the decay time at  $k_x = 0.044 \text{ \AA}^{-1}$  is  $\sim 1 \text{ ps}$ , while  $\sim 6 \text{ ps}$  at  $k_x = 0 \text{ \AA}^{-1}$ . Furthermore, it has a maximum amplitude of  $\sim 36 \pm 5 \text{ meV}$  and a pulsewidth-limited rise time ( $< 100 \text{ fs}$ ). In order to understand the origin of this second component, the dynamics of the VB intensity is considered. For this purpose, we integrate the VB spectral weights in the rectangular areas in Fig. 3.3(b). This procedure provides the green dots displayed in Fig. 3.3(c). Notice that they not only reproduce the transient depletion of the VB but, if properly rescaled, they also match the green dashed lines (component C2). Photoexcitation generates electrons in CB and holes in VB, which occupy states at the corresponding band edges. In particular, holes accumulate at the maximum of the VB, as confirmed by the slower intensity recovery at  $k_x = 0 \text{ \AA}^{-1}$ . The gathering of holes reduces the ARPES spectral weight and, as a result, the VB edge moves downward in energy. This is possible because the used pump fluence of  $0.4 \text{ mJ/cm}^2$  corresponds to a photo-carrier density  $< 10^{19} \text{ cm}^{-3}$ , which overcomes the equilibrium carrier density of  $\sim 10^{16} \text{ cm}^{-3}$  (see Paragraph 3.4.2). The simultaneous occurrence of depletion at the VB top and filling at the CB bottom determines a blue-shift of the optical absorption edge, that is called the Burstein-Moss shift (BMS) [24, 132], due to Pauli blocking [133] (see Paragraph 1.2.1). Since the amplitudes of BGR and BMS are comparable but opposite, these phenomena compensate almost completely. The concurrence of these two counterbalancing phenomena justifies the different conclusions about the presence of BGR in BP from earlier TR-ARPES studies [22, 23]. Therefore, thanks to our analysis, we disentangle these two effects, confirming the presence of both BGR and BMS.



### 3.4 TR-ARPES on Cs-doped BP

In this section, we analyze the ultrafast response of photo-excited BP in presence of a vertical electric bias, resulting from Cs adsorption. Firstly, it is necessary to specify that Cs atoms, as all alkali atoms, donate electrons [35]. Therefore, the Cs doping determines the formation of a  $n$ -type surface region, causing a band bending [36]. More precisely, the energy bands bend downwards as one moves from bulk to surface (in presence of a  $p$ -type surface region, an upward band bending would occur [36]). Besides, since BP is host to the giant Stark effect, the CB bending is considerably larger than the VB one [15, 16, 120] and, for Cs surface doping  $> 0.35$  1L, a surface band inversion takes place [15]. In addition to these effects, we observe that an appreciable (up to  $\sim 0.25$  V) surface photovoltage (SPV, see Paragraph 1.2.3) [40, 134] is induced in Cs-adsorbed BP by pump irradiation. In the presence of downward band bending photo-injected electrons and holes are spatially separated by the built-in potential generated by surface doping: electrons migrate towards the surface, while holes move towards the bulk. This charge separation generates a dipole electric field (and potential) that (*i*) opposes to the alkali-induced bending and (*ii*) can extend outside the sample. Photo-emitted electrons experience this accelerating potential even if they are emitted before pump arrival, provided they meanwhile are moving in the vacuum region where the dipole field acts.

Let us consider the three static ARPES maps of BP shown in Fig. 3.4a, which are acquired at negative pump-probe delay of  $\sim -1$  ps after a Cs deposition of 45 s ( $\sim 0.35$  1L). In order to emphasize the Cs-induced variations, the ARPES spectrum in the absence of the pump is first displayed on the left map of Fig. 3.4a. If one compares this map with the one in Fig. 3.2(a), it is evident that there is a downward shift of the VB top of  $\sim 0.3$  eV and a concomitant downward bending of  $\sim 0.6$  eV of the CB minimum, which approximately touches the VB maximum, corresponding to the apparent closing of the bandgap. The central and right maps of Fig. 3.4a report the ARPES spectrum at pump fluences  $F_{pump}$  of  $24 \mu\text{J}/\text{cm}^2$  and  $485 \mu\text{J}/\text{cm}^2$ . As we can see, by increasing  $F_{pump}$ , a rigid and non-linear shift of the whole ARPES spectrum to higher energy is recorded, as a consequence of SPV. Notice that also the Fermi level  $E_F$  moves consequently. By considering the top scale of Fig. 3.4b, one can observe the saturation of SPV at higher  $F_{pump}$ . We convert the incident pump fluence  $F_{pump}$  into photo-excited carrier concentration  $n_{eh}$ , which is reported on the bottom axis (see Paragraph 3.4.2), and fit the experimental data with a phenomenological logarithmic model [41, 42]:  $\phi_{SPV} = \alpha k_B T / e \ln(1 + n_{eh}/p_0)$ . In the last equation,  $\alpha = 1.33 \pm 0.05$  and  $p_0 = 2.8 \pm 0.5 \times 10^{16} \text{cm}^{-3}$  are fitting parameters,  $n_{eh}$  is the photo-injected carrier density and  $k_B T = 25$  meV is the thermal energy at room temperature.

Through the fitting procedure illustrated in Paragraph 3.4.1, we estimate the en-

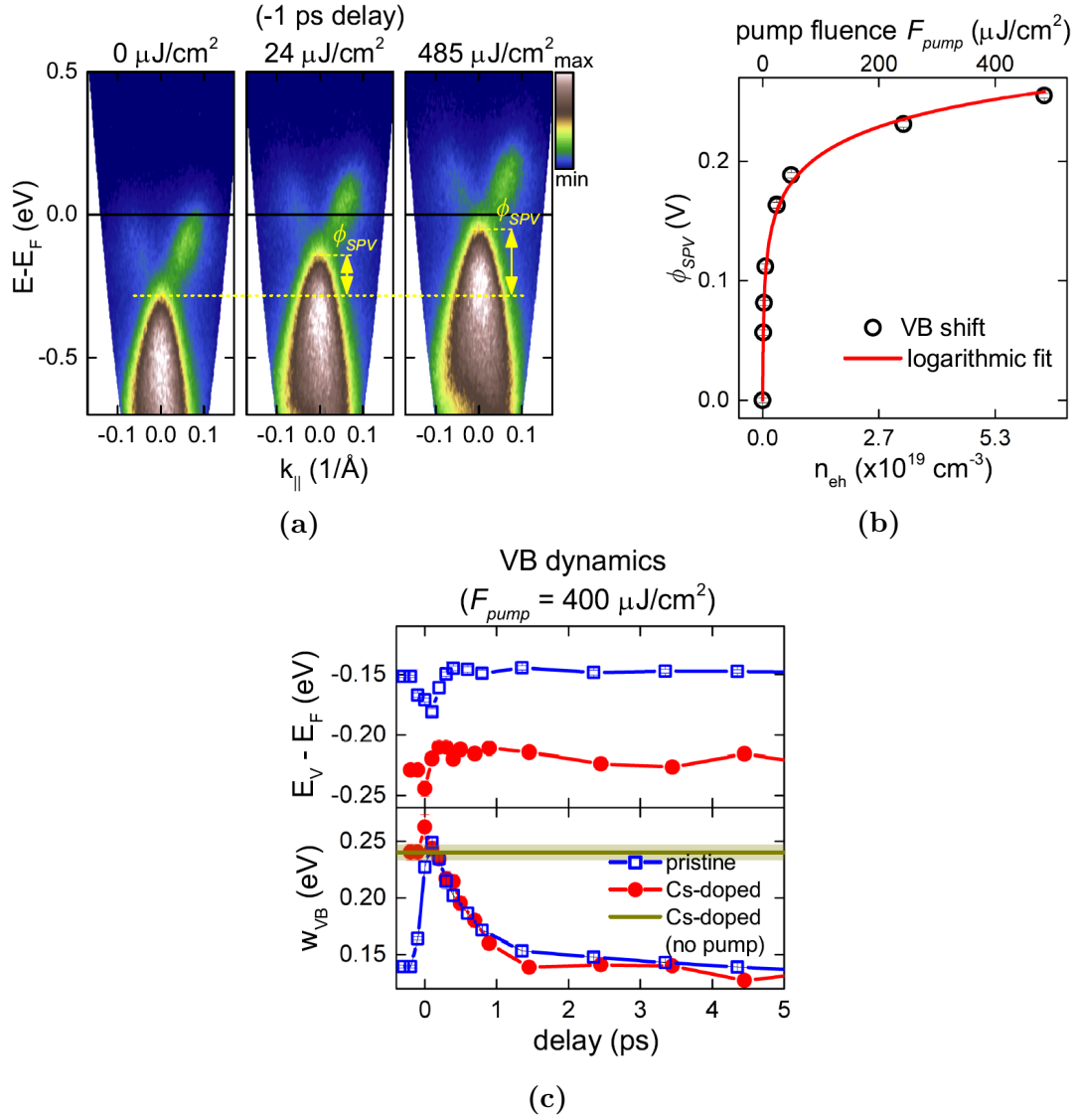


**Figure 3.4.** Surface photovoltage (SPV) and transient photo-induced effects from Ref. [1]. (a) ARPES maps after 45 s Cs exposure at three pump fluences ( $0 \mu\text{J}/\text{cm}^2$ ,  $24 \mu\text{J}/\text{cm}^2$ ,  $485 \mu\text{J}/\text{cm}^2$ ) and negative pump-probe delay of -1 ps. The asymmetric shape of the CB is an effect of the selection rules in the photoemission. The presence of SPV can be recognized by the shift of the spectra. (b) Bottom scale: surface photovoltage ( $\phi_{SPV}$ ) as a function of the photo-excited carrier density ( $n_{eh}$ ); top scale:  $\phi_{SPV}$  as a function of the pump fluence ( $F_{pump}$ ). (c) VB maximum (top) and broadening (bottom) of pristine (open squares), and Cs-doped BP (solid circles) as a function of the pump-probe delay.

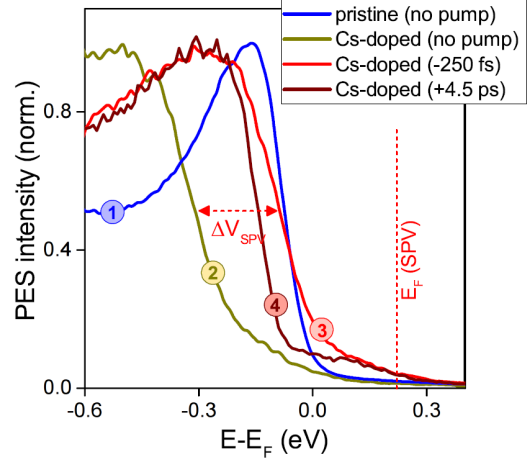


**Figure 3.5.** Comparison of EDCs at  $k_x = 0 \text{ \AA}^{-1}$  in different doping/pumping conditions.

ergy of the VB maximum,  $E_V$ , and its edge width  $w_{VB}$  at different pump-probe delays and the resulting VB dynamics is shown in Fig. 3.4c. Here, open squares stand for temporal evolutions before Cs coverage, while solid circles indicate the behaviours after Cs exposure. In all cases, the pump fluence is  $\sim 0.4 \text{ mJ/cm}^2$ . The dynamics of  $E_V$  for undoped BP is equal to the one reported in Fig. 3.3(c). Regardless of the different binding energies, the temporal evolutions of the VB maximum after photoexcitation with and without Cs coverage closely resemble each other. Here we point out that, similar to the case of undoped BP previously illustrated, the coexistence of BGR and band flattening might apply also to the Cs-doped sample. Let us now focus on the dynamics of the peak width (lower graph): pump irradiation in undoped BP causes a considerable broadening of the VB, in agreement with recent experimental observations [22]. In Cs-doped BP and in the absence of pump (see dark yellow horizontal line), the VB width is nearly twice as compared to the pristine case, whereas after laser pumping (solid circles) it undergoes a marked reduction that follows the temporal evolution of the undoped sample very closely. This coincidence provides a useful hint to clarify the band dynamics in Cs-doped BP and also the VB broadening in the pristine sample. We begin examining the EDCs in Fig. 3.5, which refer to  $k_x = 0 \text{ \AA}^{-1}$ . Each spectrum is marked by a different number/color and represents a specific situation.

1.(blue): pristine BP. The starting point is the VB spectrum of pristine BP without pump effects.

2.(dark yellow): Cs-doped BP. After Cs-doping the VB shifts to lower energy, as a consequence of the alkali-induced band bending. Notice the enhanced width of the VB edge (here, no pump is present).

3.(red): Cs-doped BP, negative pump-probe delay. Laser irradiation affects the Cs-doped sample even at negative delay: it leads to a rigid shift of the whole

spectrum (including the Fermi level) to higher energy, as a consequence of the SPV effect. Notice that the shape of this spectrum is identical (within the experimental uncertainty) to the one recorded without pump. In fact, electrons are first emitted by the probe and then accelerated by the pump-induced SPV, thus preserving the un-pumped spectral shape.

4.(dark red): Cs-doped BP, positive pump-probe delay. A few picoseconds past the pump, no significant shift of the VB is observed (SPV is still present and unaltered), but the width of the band edge is considerably reduced and very similar to the pristine BP case. Here, the pump effect on the spectrum (i.e. the reduced peak width) is genuine since electrons are emitted *after* pump arrival. Keeping in mind these phenomenological aspects, we can now provide the physical explanation. Fig. 3.6 sketches the photoemission process in the specific situations previously discussed. In Panel (a) of Fig. 3.6 the photoemission process for the

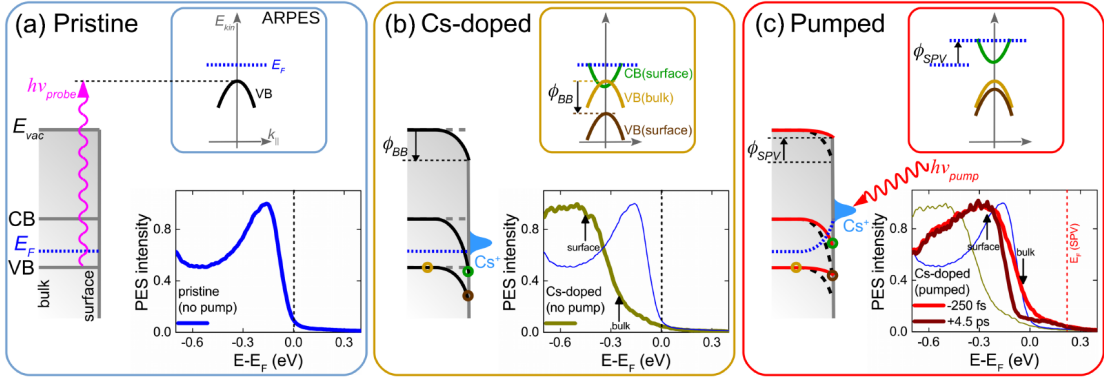


**Figure 3.6.** Scheme of photoemission process for (a) pristine BP, (b) Cs-doped BP and (c) pumped, Cs-doped BP from Ref. [1]. The upper inset in each panel illustrates the expected ARPES spectrum, the lower shows the measured EDCs at  $k_{\parallel} = 0 \text{ \AA}^{-1}$ .  $E_F$ : Fermi level,  $E_{vac}$ : vacuum level,  $\phi_{BB}$ : band bending potential,  $\phi_{SPV}$ : surface photo-voltage.

pristine BP case is depicted. As there is no band bending, all relevant energy levels of the sample, i.e. CB, VB,  $E_F$  and the vacuum level  $E_{vac}$ , are indicated by horizontal lines. Electrons are promoted to free states by the probe photons with energy  $h\nu_{probe}$ . As a result, they travel in vacuum towards the electron analyzer, which acquires the ARPES spectrum, as shown in the upper inset. The graph in the lower inset reports the measured EDC at  $k_x = 0 \text{ \AA}^{-1}$ . Panel (b) of Fig. 3.6 shows the Cs-doped BP case in the absence of the pump pulse. The first aspect to note is that Cs surface states are situated above the Fermi level  $E_F$  because they are ionized donors. For this reason, the surface region of the sample turns out to be *n*-doped and, as a result, a downward bending potential  $\phi_{BB}$  is established.

As already said, the CB bending is larger than the VB one because of the Stark effect. More in detail, when the alkali doping becomes sufficiently high, i.e.  $> 0.11$  L as stated in Ref. [15], the CB minimum at the surface shifts below the Fermi level (green circle), which makes it detectable by static photoemission. By comparing the EDC in the lower inset with the one of the pristine BP case (lower inset of Fig. 3.6(a)), an enhancement of the VB width can be recognized. In order to understand the reason behind this modification, we focus on the VB and the photoemission process for the Cs-doped BP. In this case, owing to the downward band bending, the electrons photoemitted from the surface (brown circle) are characterized by larger binding energy. Therefore, they give rise to the main peak of the PES spectrum. Nevertheless, for the low photon energy (6 eV) used in our experiment, the bulk sensitivity of photoemission is increased because of the large electron mean free path [3]. This implies that bulk VB states, indicated by dark yellow circle, are also detected. Due to their lower binding energy with respect to the surface VB states, they determine the enhanced VB width after Cs doping (see the vertical arrows in the EDC).

Lastly, let us consider the pumped Cs-doped BP case, which is displayed in Fig. 3.6(c). Notice that, in such case, two EDCs, one at negative pump-probe delay (i.e. - 250 fs, red curve) and one at positive pump-probe delay (i.e. + 4.5 ps, dark red curve) are reported in the lower graph. Indeed, depending on whether the probe pulse precedes or follows the pump pulse, different spectral features can be observed. When Cs-doped BP is irradiated by the pump pulse, the SPV sets it: the energy levels at the surface move upward and, as a consequence, the band bending is compensated. At negative pump-probe delays, SPV develops after electron photoemission. The resulting dipole electric field accelerates the free electrons traveling in vacuum, leading to a rigid shift of the whole PES spectrum. For this reason, the EDC at negative pump-probe delay is the same as the one measured without pump (dark yellow EDC of the lower graph in Fig. 3.6(b)), except for the energy shift: the un-pumped EDC shape is preserved because electrons are photoemitted before excitation. On the other hand, it is also evident that the EDC at positive pump-probe delay, i.e. when probe photons follow the pump pulse, looks like the photoemission spectrum of the pristine BP case. This result is due to the fact that SPV sets in before photoemission and, therefore, surface and bulk levels recover almost identical binding energies, counterbalancing the Cs-doping effect. Notice in particular that the dynamics of the peak width formerly reported in Fig. 3.4c (red curve) indirectly represents the dynamics of the SPV which in turn, in light of the previous observations, reveals the temporal evolution of electron-hole space separation that generates a long-range dipole field [45].

At this point, we can also explain the photo-induced dynamics of the VB broadening in pristine BP. Its similarity to the Cs-doped one at positive delay (Fig.3.4c,

bottom graph) suggests a common physical origin. Pump irradiation generates equal densities of electrons and holes, which can be considerably larger than the equilibrium ones [1] and decrease exponentially from the surface towards the bulk. These concentration gradients determine the carriers diffusion. We first recall that hole mobility perpendicular to the bulk BP surface is higher than the electron one [5]. Einstein's relation states that mobility  $\mu$  and diffusion coefficient  $D$  are directly proportional ( $D = \mu k_B T$ ), therefore we expect that holes diffuse faster than electrons. This implies that, upon pumping, electrons tend to accumulate at the sample surface while holes diffuse towards the bulk. This charge separation generates a dipole field which, in turn, gives rise to a potential, named Dember photovoltage [40] (see Paragraph 3.4.3), able to modify the bands energy position at the surface. Our photoemission bulk sensitivity allows us to record these modifications that manifest as peak broadening, in analogy with the Cs-doped case. The dipole field counterbalances charge separation and spectral broadening (see Fig. 3.4c). This explanation is also corroborated by two experimental findings: (i) the logarithmic saturation of the Dember photovoltage as a function of the carrier concentration [40] and (ii) a similar logarithmic trend of the VB band broadening in pristine BP as a function of the pump fluence [22].

Having elucidated the physical significance of our experimental observations, we can now deal with the combined effects of Cs doping and photo-excitation in BP. Figs. 3.7(a)-(f) report RT ARPES maps measured at negative ( $-0.5$  ps, (a)-(c)) and positive ( $+1.5$  ps, (d)-(f)) pump-probe delays for three Cs exposure times, i.e. 15, 30 and 45 s. Figs. 3.7(g)-(i) display the related EDCs at  $0^\circ$  emission angle ( $k_x = 0 \text{ \AA}^{-1}$ ). Here, the zero energy coincides with the onset of the VB at positive delay ( $E_{onset(+)}$ ), for comparative purpose. We first point out that, by increasing Cs deposition, the CB minimum shifts to lower energy, relative to the VB, as a consequence of the Stark effect [15,16]. At the highest concentration and negative delay (45 s, bottom), VB and CB cross each other. This situation corresponds to the critical Cs doping of 0.35 monolayers identified by Ref. [15]. Comparing negative and positive delays, the energy position and line shape of the CB do not vary after photo-excitation. A reduction of spectral weight can be only recognized as a result of photo-induced depletion. On the other hand, there is a remarkable change of the VB binding energy after pumping, common to all Cs contents: the onset shifts to lower energy at positive delay. As previously illustrated in Fig. 3.6, this is the result of the pump-induced SPV that counterbalances the Cs-induced band bending potential and it is resolved thanks to the bulk sensitivity of our ARPES photon energy. Therefore, the observed VB shift is actually caused by its edge sharpening. Indeed, at negative pump-probe delay, the VB onset in Cs-doped BP is defined by its bulk level with lower binding energy with respect to the surface ones (upper inset in Fig. 3.6(b)). After optical excitation, SPV and

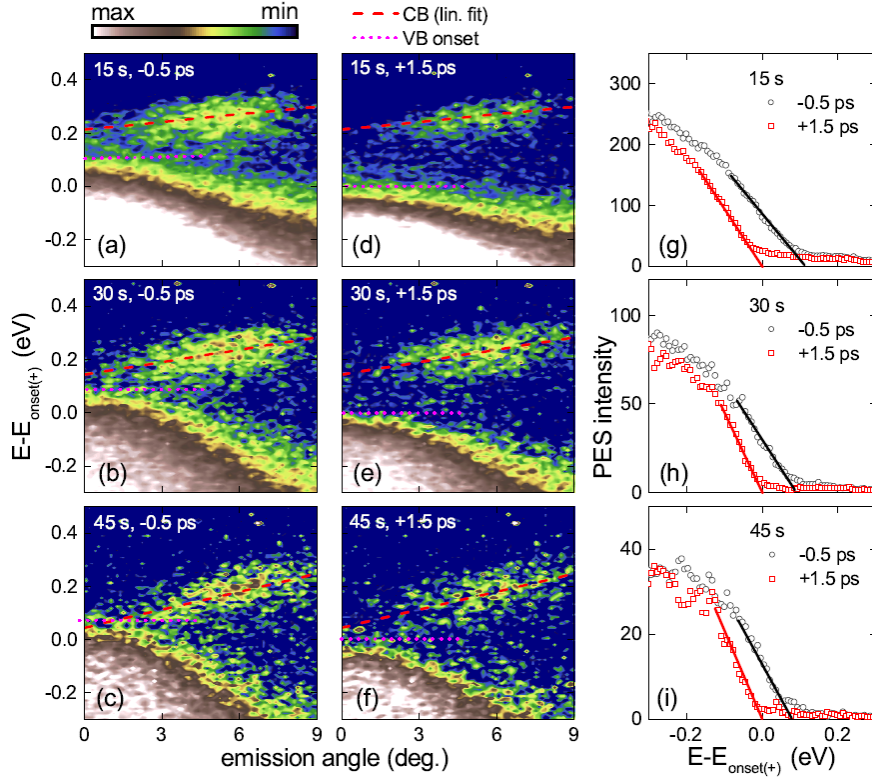


**Figure 3.7.** ARPES maps recorded at  $-0.5$  ps pump-probe delay (a)-(c) and at  $+1.5$  ps delay (d)-(f) for three increasing Cs exposure times (15 s, 30 s and 45 s, top to bottom) from Ref. [1]. The graphs on the right side (g)-(i) show the corresponding EDCs at  $0^\circ$  emission angle ( $k_x = 0 \text{ \AA}^{-1}$ ). In all maps and graphs, zero energy is referred to the *onset* of the VB at positive delay ( $E_{\text{onset}(+)}$ ), for comparative purpose. Pump fluence is  $0.4 \text{ mJ/cm}^2$ . All measurements at RT.

band bending compensate each other, thus surface and bulk states level to almost identical binding energies (upper inset in Fig. 3.6(c)), determining the sharpening of the VB edge. At this point, two important consequences of this experimental evidence need to be highlighted.

(i) Since the CB bending is larger than the VB one because the Stark effect and since SPV modified all bands identically, a noticeable photo-induced sharpening for the CB at positive delay is expected. However, this is not the case. The only plausible explanation is to assume a strong surface localization of the CB: in fact, in this circumstance the bulk contribution would be absent and the counteracting effects of SPV and band bending would simply shift the CB without any line shape modification. The surface character of the CB after alkali atoms deposition has been previously argued both experimentally [121] and theoretically [15, 16] and

finds here a further confirmation.

(ii) In view of these results, the occurrence of band inversion should be asserted carefully, especially in thick BP samples (more than a few layers). Given the strong surface localization of the CB, band inversion should take place predominantly at the sample surface. In this regard, we point out that the intertwining of CB and VB in Fig. 3.7(c) actually corresponds to the overlap between *bulk* VB and *surface* CB. Therefore, our results demonstrate that only in monolayer BP (i.e. *phosphorene*) the band inversion can be genuinely argued, since band bending and bulk contributions are not present.

### 3.4.1 Spectral Analysis and Fitting

In order to estimate the band dispersions and quantify the photoexcitation effects, the following fitting procedure of the VB and CB measured by TR-ARPES is applied. Fig. 3.8 describes the procedure. Panel (a) reports the EDCs of the VB at  $k_x = 0 \text{ \AA}^{-1}$  for -250 fs (black) and 0 fs (red) pump-probe delays. From the comparison, the VB shift/broadening and the photo-induced depletion of spectral weight can be recognized. Here, we cannot directly use a gaussian distribution for the fit owing to the noticeable asymmetry of the peak. More precisely, the latter, which is caused by the presence of secondary electrons (inelastic scattering processes during photoemission), makes the correct determination of the peak position less reliable from a direct peak fitting. For this reason, an alternative procedure is followed. The first step is to calculate the EDCs numerical derivative and, then, the resulting curves are fitted with the analytical derivative of the gaussian function:

$$\frac{\partial}{\partial E} \left[ A e^{-\frac{2(E-E_V)^2}{w_{VB}^2}} \right] = - \left[ \frac{4A(E - E_V)}{w_{VB}^2} \right] e^{-\frac{2(E-E_V)^2}{w_{VB}^2}},$$

where  $E_V$  is the binding energy,  $w_{VB}$  is the width ( $2\sigma$ ) and  $A$  is the peak amplitude. The outcomes are illustrated in Panel (b). As shown by the reconstructed gaussian curves in Panel (a), the fits carried out in the yellow-shaded region give a precise quantification of the high-energy side of the original VB peaks, overcoming the peak asymmetry issue. To determine the VB dispersion, the same procedure has been repeated at different values of  $k_x$ . We have also tested the Shirley method to delete the incoherent background. Almost identical peak positions and widths have been obtained, but poorer estimates of the peak amplitude.

Fig. 3.8(c) shows the fitting procedure for the CB at larger delay (+ 3 ps) and at  $k_x = 0.04 \text{ \AA}^{-1}$ . In this case, owing to the good definition of the spectral feature, a direct modeling of the peak with a gaussian profile and a linear background can



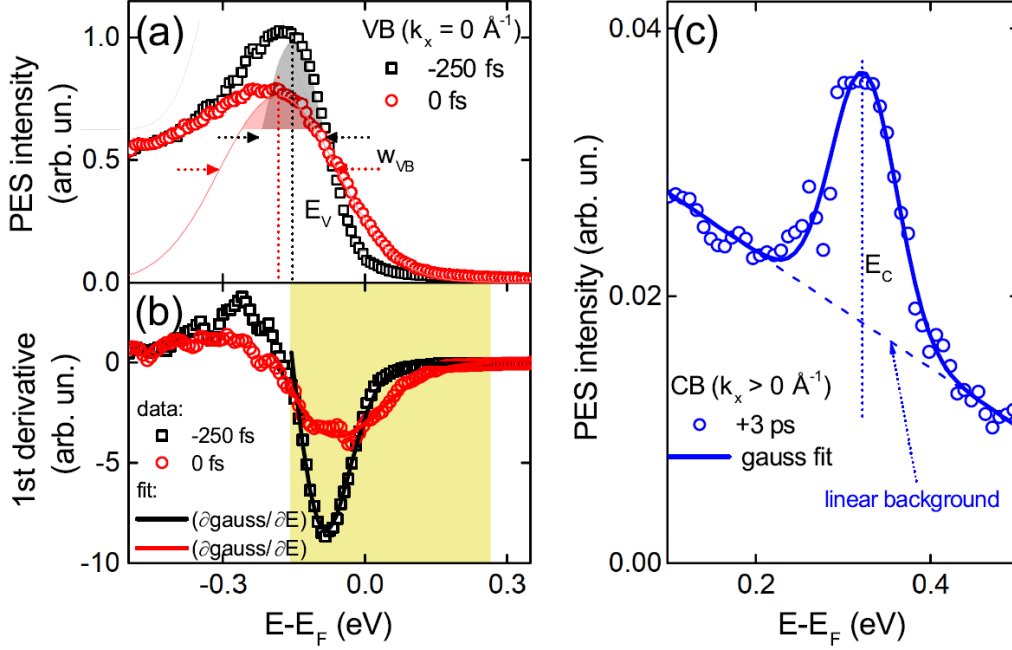


**Figure 3.8.** (a) EDCs of the VB of pristine BP at  $k_x = 0 \text{ \AA}^{-1}$  for -250 fs (black) and 0 fs (red) pump-probe delays from Ref. [1]. (b) Numerical derivative of the EDCs shown in panel (a): the solid lines are fits (see text). The resulting peaks are reproduced as shaded areas in panel (a), with the associated peak position  $E_V$  and  $w_{VB}$ . (c) EDC of the CB at  $k_x = 0.04 \text{ \AA}^{-1}$  and +3 ps delay: the solid line is a gaussian fit centered at  $E_C$ .

be performed. The binding energy of the CB is determined by the position of gaussian peak ( $E_C$ ). As in the case of the VB, the dispersion of the CB is evinced from the fitting at various  $k_x$ .

### 3.4.2 Electronic and Optical Properties of BP

According to the TR-ARPES analysis previously described, the bandgap of BP has been estimated as  $E_g = 0.44 \pm 0.01$  eV, with the VB maximum  $\sim 0.15$  eV below the Fermi level and the CB minimum  $\sim 0.29$  eV above  $E_F$ , as shown in Fig. 3.9(a). This analysis refers to positive pump-probe delay, i.e.  $\sim +2.4$  ps, when the CB is populated. This value of the gap is lightly larger than the generally reported ones (0.3 – 0.4 eV) [113]. However, this discrepancy might be due to the  $k_z$  sensitivity of photoemission, related to our photon energy. The band dispersion along the  $\Gamma Z$  crystallographic direction is very strong. Therefore, our 6 eV probe photon might explore a  $k_z$  slightly away from the  $Z$ -point, thus measuring a larger

bandgap. Furthermore, according to our fitting procedure, we have observed that the CB line width is almost half the VB one at negative delay ( $w_{CB} \approx 0.08$  eV,  $w_{VB} \approx 0.15$  eV). This discrepancy might be a consequence of the poor  $k_z$  selectivity of our probe photon (and also suggests a strong surface localization of the CB). As demonstrative test, we show a VB spectral simulation assuming a smaller gaussian line width ( $w \approx 0.1$  eV) convoluted with a possible spectral function  $a(E)$ , as depicted in Fig. 3.9(b). Here,  $a(E)$  decays exponentially at large binding energy and it is peaked at  $E_V - E_F = -0.09$  eV. By means of a convolution with a

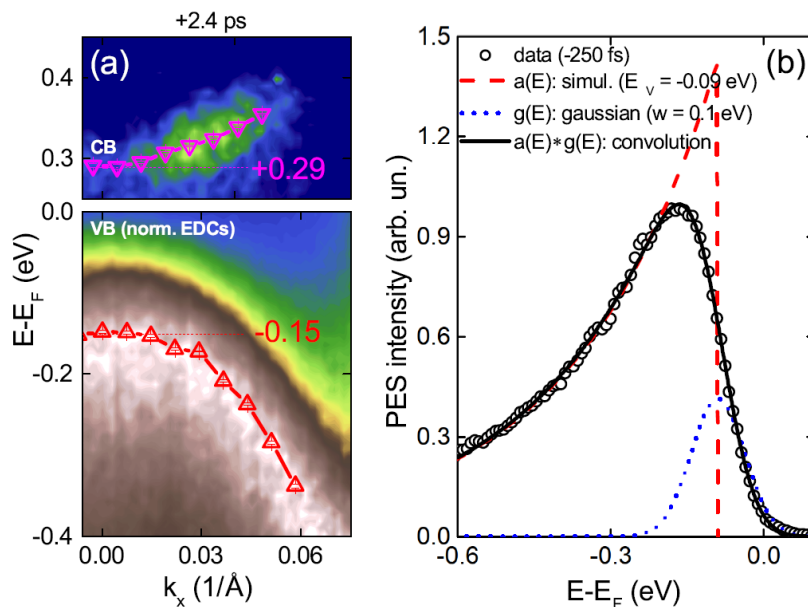


**Figure 3.9.** (a) ARPES maps and dispersion fits of CB (top) and VB (bottom) at +2.4 ps delay from Ref. [1]. (b) Simulation of the VB photoemission spectrum at negative delay (Ref. [1]): the spectral function  $a(E)$  is peaked at  $E_V - E_F = -0.09$  eV and decays exponentially at larger binding energy. By a convolution with a gaussian profile  $g(E)$  (line width  $w = 0.1$  eV), it matches the experimental data.

gaussian function, it produces a very satisfactory fit of the experimental spectrum, where the VB maximum turns out to be at  $E_V = -0.09$  eV instead of  $-0.15$  eV and the bandgap  $E_g$  equal to 0.38 eV.

Independently of the precise value of the bandgap, an estimation of the equilibrium carrier concentrations in BP at room temperature can be performed. By textbook definitions [17],  $n_0 = N_C e^{-(E_C - E_F)/k_B T}$  (electrons in CB) and  $p_0 = N_V e^{-(E_F - E_V)/k_B T}$  (holes in VB), with  $N_C = 2.5(m_C/m_0)^{3/2} \times 10^{19} \text{ cm}^{-3}$ ,  $N_V = 2.5(m_V/m_0)^{3/2} \times 10^{19} \text{ cm}^{-3}$  and  $n_i^2 = n_0 p_0 = N_C N_V e^{-2(E_C - E_V)/k_B T}$  (mass action law). Here,  $E_V$  and  $E_C$  are the energies of the VB maximum and CB minimum,  $m_V$  and  $m_C$  the respective effective masses,  $E_F$  is the Fermi level,  $k_B T = 0.025$  eV

is the thermal energy at RT and  $n_i$  is the intrinsic carrier density. Since electron and hole effective masses in BP are almost identical ( $m_C \sim m_V \sim 0.23m_0$ ) [5], one obtains  $N_C \sim N_V \sim 2.8 \times 10^{18} \text{ cm}^{-3}$ . This value does not depend on the bandgap and represents the maximum achievable carrier density at the VB (CB) maximum (minimum) under equilibrium conditions and in the non-degenerate case. Starting from the measured values of  $E_g$  and the VB maximum, the equilibrium electron and hole concentrations can be quantified. The results are shown in Table 3.1 (for comparison, both values derived from the fitting procedure and from the convolution are utilized). Notice that majority carrier density  $p_0$  is of the order of  $\sim 10^{16}$

$E_g[\text{eV}]$	$E_V - E_F [\text{eV}]$	$n_i[\text{cm}^{-3}]$	$p_0[\text{cm}^{-3}]$	$n_0[\text{cm}^{-3}]$
$0.44 \pm 0.01$	-0.15	$4.2 \times 10^{14}$	$6.9 \times 10^{15}$	$2.6 \times 10^{13}$
0.38	-0.09	$1.4 \times 10^{15}$	$7.7 \times 10^{16}$	$2.6 \times 10^{12}$

**Table 3.1.**  $E_g$  is the estimated bandgap,  $E_V - E_F$  is the binding energy of the VB,  $n_i$  is the intrinsic carrier density,  $p_0$  and  $n_0$  are the estimated hole (in VB) and electron (in CB) concentrations at room temperature.

$\text{cm}^{-3}$  and agrees fairly well with the value deduced from the fluence dependence of the SPV (Fig. 3.4b). More interestingly, a comparison between the equilibrium electron and hole densities and the photo-induced ones can be performed. Based on the reported optical properties of BP [5], pump photon  $h\nu \sim 1.82 \text{ eV}$  ( $\lambda \sim 680 \text{ nm}$ ) and an electric field polarized along the  $x$ -axis (armchair direction) give rise to a dielectric constant  $\epsilon \sim 12 + 2i$ . The latter determines, in turn, a refractive index  $n = \sqrt{\epsilon} \sim 3.5 + 0.3i$ , reflectivity  $R = (|n - 1|/|n + 1|)^2 \sim 0.3$  and absorption length  $1/\alpha = \lambda/4\pi\text{Im}(n) \sim 180 \text{ nm}$  [135]. By considering the relation [135]  $n_{eh} = F_{pump}(1 - R)\alpha/h\nu$ , where the quantum efficiency is set equal to 1, the pump fluence  $F_{pump}[\text{J}/\text{cm}^2]$  can be transformed into density of photo-excited electron-hole pairs  $n_{eh}[\text{cm}^{-3}]$ . In the same way, the variation (increase) of the lattice temperature can be estimated as [135]  $\Delta T = \phi(1 - R)\alpha M/\rho c_p$ , where  $\rho \simeq 2.7 \text{ g}/\text{cm}^3$  [136] is the mass density,  $M \simeq 31 \text{ g}/\text{mol}$  is the molar mass and  $c_p \simeq 21 \text{ J}/\text{mol K}$  is the lattice specific heat of BP [136]. For a pump fluence of  $\sim 0.5 \text{ mJ}/\text{cm}^2$ , one gets  $n_{eh} \sim 7 \times 10^{19} \text{ cm}^{-3}$  and  $\Delta T \sim 11 \text{ K}$ . It is important to note that  $n_{eh}$  (photoexcitation)  $\gg N_C, N_V$  (maximum carrier density at RT)  $\gg p_0$  (majority carrier density). Therefore, with the typical laser fluence we employ, we are always in a strong photoexcitation regime.

### 3.4.3 The Demer Potential

Upon pump irradiation, equal electron and hole distributions,  $\delta n$  and  $\delta p$  respectively, are generated. The latter can be much higher than the equilibrium densities

$(n_0, p_0)$  in particular at the surface (for  $p$ -doped samples,  $\delta n, \delta p \gg p_0 \gg n_0$ ) and decay exponentially from the surface to the bulk. Carriers diffusion is induced by density gradient. In the following, recombination and drift processes are neglected. Ref. [5] reports that in bulk BP hole mobility  $\mu_p$  along the direction perpendicular to the surface, i.e. the  $z$ -axis, is larger than the electron mobility  $\mu_n$ . By considering that mobility and diffusion coefficient are directly proportional [35], it is expected that holes diffuse faster than electrons. As a result, after pump arrival, holes head towards the bulk, whereas electrons gather at the sample surface. Diffusion equation [137] enables one to describe this process:

$$\frac{\partial \delta n(z, t)}{\partial t} = D_n \frac{\partial^2 \delta n(z, t)}{\partial z^2}, \quad (3.1)$$

$$\frac{\partial \delta p(z, t)}{\partial t} = D_p \frac{\partial^2 \delta p(z, t)}{\partial z^2}, \quad (3.2)$$

$$\delta p(z, 0) = \delta n(z, 0) = n_{eh} \exp(-\alpha |z|). \quad (3.3)$$

Here,  $D_n = k_B T \mu_n / e$ ,  $D_p = k_B T \mu_p / e$ ,  $n_{eh}$  is the photo-excited carrier density and  $\alpha$  is the pump absorption coefficient. Since diffusion through the sample surface cannot occur, the absolute value  $|z|$  is used in Eq. (3.3), where the initial conditions are fixed. By analytically solving the system of equations (3.1)-(3.3), the carrier distributions over depth and time can be retrieved. More in detail, in our case, the quantity  $\delta r(z, t) = [\delta p(z, t) - \delta n(z, t)] / n_{eh}$  plays an important role:  $\delta r(z, t)$  results to be positive when holes exceed electrons and negative if electrons surpass holes. Fig. 3.10(a) depicts the temporal and depth evolution of  $\delta r(z, t)$ . Within a few picoseconds, electrons gather at the sample surface ( $\delta r(z, t) < 0$ ) as indicated by blue color, whereas holes shift towards the bulk ( $\delta r(z, t) > 0$ ) as shown by red color. Here, the estimated diffusion coefficients refer to the room temperature case. The temporal evolution of  $\delta r$  at  $z = 0$  for  $T = 300$  K (green solid curve) and  $T = 1000$  K (orange dashed curve) is reported in Fig. 3.10(b). The electron-hole separation determines the development of an electric dipole field  $E_d$ . As we can see from Fig. 3.10(a), the region of sample surface where electrons exceed is highlighted in light blue, while the region where holes accumulate is marked in light red. Between these two regions of opposite electric charge, the dipole field  $E_d$  (large black arrow in Fig. 3.10(a)) arises, in order to compensate the charge separation. The amplitude of the dipole field can be estimated starting from the expressions of hole and electron currents, which are [137]:

$$J_n(z, t)/e = \mu_n(\delta n + n_0)E_d + D_n \frac{\partial \delta n(z, t)}{\partial z}, \quad (3.4)$$

$$J_p(z, t)/e = \mu_p(\delta p + p_0)E_d - D_p \frac{\partial \delta p(z, t)}{\partial z}. \quad (3.5)$$

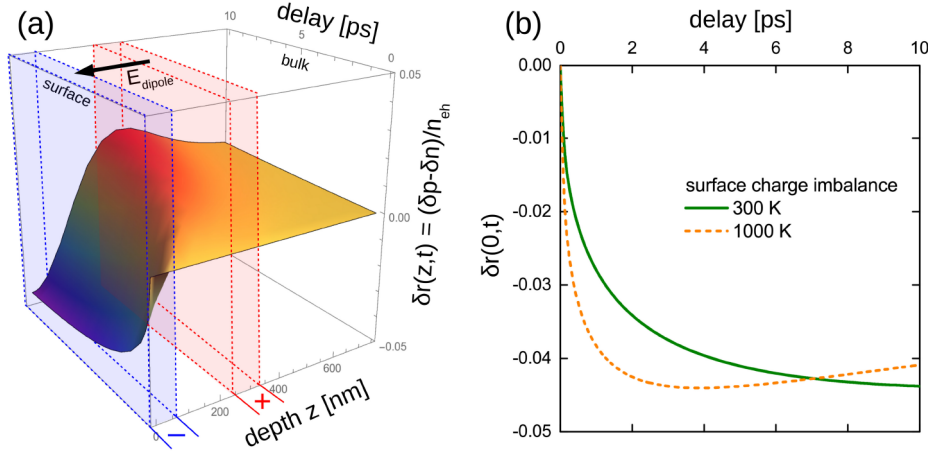


**Figure 3.10.** (a) Simulation of electrons and holes diffusion after pump irradiation, according to Eqs.(3.1)-(3.3) from Ref. [1]. The colored surface represents  $\delta r(z, t) = [\delta p(z, t) - \delta n(z, t)] / n_{eh}$  as a function of delay  $t$  and depth  $z$  (blue color:  $p < n$ , red color  $n < p$ ). Charge separation gives rise to a dipole field  $E_d$  that compensates diffusion. (b) Surface charge imbalance at  $z = 0$  as a function of delay at 300 K (green solid line) and 1000 K (orange dashed line) from Ref. [1].

Indeed, since the dipole field  $E_d$  neutralizes diffusion, it can be obtained by imposing that the total current is equal to zero, i.e.  $J_n + J_p = 0$ . Thereby, the following expression of  $E_d$  is derived:

$$E_d = \frac{D_p \frac{\partial \delta p}{\partial z} - D_n \frac{\partial \delta n}{\partial z}}{\mu_p (\delta p + p_0) + \mu_n (\delta n + n_0)} \approx \frac{(D_p - D_n) \frac{\partial \delta p}{\partial z}}{(\mu_p + \mu_n) \delta p + \mu_p p_0}. \quad (3.6)$$

The last term of Eq. (3.6) is obtained by taking into account that for a  $p$ -doped sample  $\delta p \sim \delta n \gg p_0 \gg n_0$ . If the dipole field  $E_d$  is known, the associated potential  $\phi_D$  can be estimated by integration, namely:

$$\begin{aligned} \phi_D &= - \int_0^\infty E_d dz = - \int_0^\infty \frac{(D_p - D_n) \frac{\partial \delta p}{\partial z}}{(\mu_p + \mu_n) \delta p + \mu_p p_0} dz \\ &= \frac{D_p - D_n}{\mu_p + \mu_n} \ln \left( 1 + \frac{\mu_p + \mu_n}{\mu_p} \frac{\delta p(0, t)}{p_0} \right). \end{aligned} \quad (3.7)$$

This is the Demer photovoltage [40]. By setting  $\mu_p = 550 \text{ cm}^2/\text{Vs}$ ,  $\mu_n = 400 \text{ cm}^2/\text{Vs}$  and  $\delta p/p_0 \sim 10^2 - 10^3$ , one finds  $\phi_D \sim (0.8 - 1.2)k_B T/e$ . A transient photo-induced electronic temperature  $T \sim 10^3 \text{ K}$  determines a Demer potential  $\phi_D \sim 0.1 \text{ V}$ , in accordance with our measured VB broadening. Eq. (3.7) shows that  $\phi_D$  also saturates logarithmically with photo-injected carrier density as reported in

Ref. [22]. Therefore, the temporal evolution of the VB peak width photo-induced in pristine BP, which is shown in Fig. 3.2(c), can be attributed to the transient charge separation, analogously to the Cs-doped BP case.

### 3.5 Conclusions

In conclusion, our TR-ARPES measurements on bulk BP demonstrate that photoexcitation triggers a bandgap renormalization and a concurrent valence band flattening, due to Pauli blocking. After surface doping by Cs deposition, both valence and (to a greater degree) conduction bands experience surface bending. Under this condition, laser irradiation generates a surface photovoltage, which saturates logarithmically with increasing fluence and counterbalances the Cs-induced band bending. These findings enable us to distinguish bulk vs surface states, showing the strong surface localization of the conduction band and clarifying the true occurrence of band inversion in bulk specimens. Since the semiconductor-to-semimetal transition by means of the deposition of alkali atoms on the BP surface can be stated only in monolayer or few-layer BP, a future plan is to perform time-resolved experiments on these systems. Furthermore, we are developing a TR-ARPES setup with tunable pump source in order to obtain a pump resonant with the BP gap.

# Chapter 4

## Transition Metal Dichalcogenides

### 4.1 A general overview

In the last few years, layered two-dimensional materials, such as graphene and hexagonal boron nitride (h-BN), have received significant attention due to their potential applications in several fields [138–140]. Graphene, a single layer (*monolayer*) of carbon atoms, was the first 2D material to be extracted via mechanical exfoliation from bulk graphite in 2004. Because of its attractive properties, the discovery of graphene has stimulated a great deal of attention in the investigation of other layered 2D materials, which are able to complement the demands related to graphene and can be employed as platforms for exploring new physical and chemical phenomena.

Recently, two-dimensional transition metal dichalcogenides (TMDs) are an emerging class of the layered materials family owing to their special electrical [141], mechanical [142, 143] and optical properties [8, 144] as well as to their possible technological applications [145].

TMDs are materials of the form  $MX_2$  where  $M$  refers to a transition metal of groups 4  $\sim$  10 and  $X$  indicates a chalcogen element such as sulfur (S), selenium (Se), or tellurium (Te) as shown in Fig. 4.1. They form a group of layered compounds where a sheet of transition metal is sandwiched between two chalcogen layers. The resulting  $X$ - $M$ - $X$  slabs display strong intralayer covalent bonding and a weak mutual coupling by means of van der Waals forces, which are responsible for a quasi-two-dimensional (2D) behaviour. Because of the relatively large number of the feasible transition metal and chalcogen combinations, TMDs with various electronic structures can be realized [146–148]. The electronic structure of TMDs is based on the filling of  $d$  orbitals of the transition metals, unlike silicon or graphene in which the electronic properties depend on the hybridization of  $s$  and  $p$  orbitals. They arrange in a stacking of hexagonally packed planes and accord-

$MX_2$  → X = Chalcogen

M = Transition Metal

$MX_2$ → X = Chalcogen																																																																																																																																														
M = Transition Metal																																																																																																																																														
<table border="1" style="width: 100%; border-collapse: collapse; text-align: center;"> <tr> <td>1 IA 1</td><td>2 IIA 2A</td><td colspan="10"></td><td>13 IIIA 3A</td><td>14 IVA 4A</td><td>15 VA 5A</td><td>16 VIA 6A</td><td>17 VIIA 7A</td><td>18 VIIIA 8A</td></tr> <tr> <td>H Hydrogen 1.008</td><td>Li Lithium 6.941</td><td>Be Beryllium 9.012</td><td colspan="10"></td><td>B Boron 10.811</td><td>C Carbon 12.011</td><td>N Nitrogen 14.007</td><td>O Oxygen 15.999</td><td>F Fluorine 18.998</td><td>Ne Neon 20.180</td></tr> <tr> <td>3 11 Na Sodium 22.990</td><td>4 12 Mg Magnesium 24.305</td><td>5 3 IIB 3B</td><td>6 4 IVB 4B</td><td>7 5 VB 5B</td><td>8 6 VIB 6B</td><td>9 7 VIIB 7B</td><td>10 8 VIII 8</td><td>11 9 IB 1B</td><td>12 10 IIB 2B</td><td>13 Al Aluminum 26.982</td><td>14 Si Silicon 28.086</td><td>15 P Phosphorus 30.974</td><td>16 S Sulfur 32.06</td><td>17 Cl Chlorine 35.453</td><td>18 Ar Argon 39.948</td></tr> <tr> <td>19 K Potassium 39.098</td><td>20 Ca Calcium 40.078</td><td>21 Sc Scandium 44.956</td><td>22 Ti Titanium 47.88</td><td>23 V Vanadium 50.942</td><td>24 Cr Chromium 51.996</td><td>25 Mn Manganese 54.938</td><td>26 Fe Iron 55.845</td><td>27 Co Cobalt 58.933</td><td>28 Ni Nickel 58.693</td><td>29 Cu Copper 63.546</td><td>30 Zn Zinc 65.38</td><td>31 Ga Gallium 69.723</td><td>32 Ge Germanium 72.631</td><td>33 As Arsenic 74.922</td><td>34 Se Selenium 78.96</td><td>35 Br Bromine 79.904</td><td>36 Kr Krypton 83.798</td></tr> <tr> <td>37 Rb Rubidium 85.468</td><td>38 Sr Strontium 87.62</td><td>39 Y Yttrium 88.906</td><td>40 Zr Zirconium 91.224</td><td>41 Nb Niobium 92.906</td><td>42 Mo Molybdenum 95.94</td><td>43 Tc Technetium 98.906</td><td>44 Ru Ruthenium 101.07</td><td>45 Rh Rhodium 102.905</td><td>46 Pd Palladium 106.42</td><td>47 Ag Silver 107.868</td><td>48 Cd Cadmium 112.411</td><td>49 In Indium 114.818</td><td>50 Sn Tin 118.710</td><td>51 Sb Antimony 121.757</td><td>52 Te Tellurium 127.6</td><td>53 I Iodine 126.905</td><td>54 Xe Xenon 131.29</td></tr> <tr> <td>55 Cs Cesium 132.905</td><td>56 Ba Barium 137.327</td><td>57-71 Lanthanide Series</td><td>72 Hf Hafnium 178.49</td><td>73 Ta Tantalum 180.948</td><td>74 W Tungsten 183.84</td><td>75 Re Rhenium 186.207</td><td>76 Os Osmium 190.23</td><td>77 Ir Iridium 192.222</td><td>78 Pt Platinum 195.084</td><td>79 Au Gold 196.967</td><td>80 Hg Mercury 200.59</td><td>81 Tl Thallium 204.383</td><td>82 Pb Lead 207.2</td><td>83 Bi Bismuth 208.980</td><td>84 Po Polonium 209</td><td>85 At Astatine 209</td><td>86 Rn Radon 222</td></tr> <tr> <td>87 Fr Francium 223</td><td>88 Ra Radium 226</td><td>89-103 Actinide Series</td><td>104 Rf Rutherfordium 261</td><td>105 Db Dubnium 262</td><td>106 Sg Seaborgium 263</td><td>107 Bh Bohrium 264</td><td>108 Hs Hassium 265</td><td>109 Mt Meitnerium 266</td><td>110 Ds Darmstadtium 267</td><td>111 Rg Roentgenium 268</td><td>112 Cn Copernicium 269</td><td>113 Uut Ununtrium 270</td><td>114 Fl Flerovium 270</td><td>115 Uup Ununpentium 271</td><td>116 Lv Livermorium 273</td><td>117 Uus Ununseptium 274</td><td>118 Uuo Ununoctium 276</td></tr> </table>																		1 IA 1	2 IIA 2A											13 IIIA 3A	14 IVA 4A	15 VA 5A	16 VIA 6A	17 VIIA 7A	18 VIIIA 8A	H Hydrogen 1.008	Li Lithium 6.941	Be Beryllium 9.012											B Boron 10.811	C Carbon 12.011	N Nitrogen 14.007	O Oxygen 15.999	F Fluorine 18.998	Ne Neon 20.180	3 11 Na Sodium 22.990	4 12 Mg Magnesium 24.305	5 3 IIB 3B	6 4 IVB 4B	7 5 VB 5B	8 6 VIB 6B	9 7 VIIB 7B	10 8 VIII 8	11 9 IB 1B	12 10 IIB 2B	13 Al Aluminum 26.982	14 Si Silicon 28.086	15 P Phosphorus 30.974	16 S Sulfur 32.06	17 Cl Chlorine 35.453	18 Ar Argon 39.948	19 K Potassium 39.098	20 Ca Calcium 40.078	21 Sc Scandium 44.956	22 Ti Titanium 47.88	23 V Vanadium 50.942	24 Cr Chromium 51.996	25 Mn Manganese 54.938	26 Fe Iron 55.845	27 Co Cobalt 58.933	28 Ni Nickel 58.693	29 Cu Copper 63.546	30 Zn Zinc 65.38	31 Ga Gallium 69.723	32 Ge Germanium 72.631	33 As Arsenic 74.922	34 Se Selenium 78.96	35 Br Bromine 79.904	36 Kr Krypton 83.798	37 Rb Rubidium 85.468	38 Sr Strontium 87.62	39 Y Yttrium 88.906	40 Zr Zirconium 91.224	41 Nb Niobium 92.906	42 Mo Molybdenum 95.94	43 Tc Technetium 98.906	44 Ru Ruthenium 101.07	45 Rh Rhodium 102.905	46 Pd Palladium 106.42	47 Ag Silver 107.868	48 Cd Cadmium 112.411	49 In Indium 114.818	50 Sn Tin 118.710	51 Sb Antimony 121.757	52 Te Tellurium 127.6	53 I Iodine 126.905	54 Xe Xenon 131.29	55 Cs Cesium 132.905	56 Ba Barium 137.327	57-71 Lanthanide Series	72 Hf Hafnium 178.49	73 Ta Tantalum 180.948	74 W Tungsten 183.84	75 Re Rhenium 186.207	76 Os Osmium 190.23	77 Ir Iridium 192.222	78 Pt Platinum 195.084	79 Au Gold 196.967	80 Hg Mercury 200.59	81 Tl Thallium 204.383	82 Pb Lead 207.2	83 Bi Bismuth 208.980	84 Po Polonium 209	85 At Astatine 209	86 Rn Radon 222	87 Fr Francium 223	88 Ra Radium 226	89-103 Actinide Series	104 Rf Rutherfordium 261	105 Db Dubnium 262	106 Sg Seaborgium 263	107 Bh Bohrium 264	108 Hs Hassium 265	109 Mt Meitnerium 266	110 Ds Darmstadtium 267	111 Rg Roentgenium 268	112 Cn Copernicium 269	113 Uut Ununtrium 270	114 Fl Flerovium 270	115 Uup Ununpentium 271	116 Lv Livermorium 273	117 Uus Ununseptium 274	118 Uuo Ununoctium 276
1 IA 1	2 IIA 2A											13 IIIA 3A	14 IVA 4A	15 VA 5A	16 VIA 6A	17 VIIA 7A	18 VIIIA 8A																																																																																																																													
H Hydrogen 1.008	Li Lithium 6.941	Be Beryllium 9.012											B Boron 10.811	C Carbon 12.011	N Nitrogen 14.007	O Oxygen 15.999	F Fluorine 18.998	Ne Neon 20.180																																																																																																																												
3 11 Na Sodium 22.990	4 12 Mg Magnesium 24.305	5 3 IIB 3B	6 4 IVB 4B	7 5 VB 5B	8 6 VIB 6B	9 7 VIIB 7B	10 8 VIII 8	11 9 IB 1B	12 10 IIB 2B	13 Al Aluminum 26.982	14 Si Silicon 28.086	15 P Phosphorus 30.974	16 S Sulfur 32.06	17 Cl Chlorine 35.453	18 Ar Argon 39.948																																																																																																																															
19 K Potassium 39.098	20 Ca Calcium 40.078	21 Sc Scandium 44.956	22 Ti Titanium 47.88	23 V Vanadium 50.942	24 Cr Chromium 51.996	25 Mn Manganese 54.938	26 Fe Iron 55.845	27 Co Cobalt 58.933	28 Ni Nickel 58.693	29 Cu Copper 63.546	30 Zn Zinc 65.38	31 Ga Gallium 69.723	32 Ge Germanium 72.631	33 As Arsenic 74.922	34 Se Selenium 78.96	35 Br Bromine 79.904	36 Kr Krypton 83.798																																																																																																																													
37 Rb Rubidium 85.468	38 Sr Strontium 87.62	39 Y Yttrium 88.906	40 Zr Zirconium 91.224	41 Nb Niobium 92.906	42 Mo Molybdenum 95.94	43 Tc Technetium 98.906	44 Ru Ruthenium 101.07	45 Rh Rhodium 102.905	46 Pd Palladium 106.42	47 Ag Silver 107.868	48 Cd Cadmium 112.411	49 In Indium 114.818	50 Sn Tin 118.710	51 Sb Antimony 121.757	52 Te Tellurium 127.6	53 I Iodine 126.905	54 Xe Xenon 131.29																																																																																																																													
55 Cs Cesium 132.905	56 Ba Barium 137.327	57-71 Lanthanide Series	72 Hf Hafnium 178.49	73 Ta Tantalum 180.948	74 W Tungsten 183.84	75 Re Rhenium 186.207	76 Os Osmium 190.23	77 Ir Iridium 192.222	78 Pt Platinum 195.084	79 Au Gold 196.967	80 Hg Mercury 200.59	81 Tl Thallium 204.383	82 Pb Lead 207.2	83 Bi Bismuth 208.980	84 Po Polonium 209	85 At Astatine 209	86 Rn Radon 222																																																																																																																													
87 Fr Francium 223	88 Ra Radium 226	89-103 Actinide Series	104 Rf Rutherfordium 261	105 Db Dubnium 262	106 Sg Seaborgium 263	107 Bh Bohrium 264	108 Hs Hassium 265	109 Mt Meitnerium 266	110 Ds Darmstadtium 267	111 Rg Roentgenium 268	112 Cn Copernicium 269	113 Uut Ununtrium 270	114 Fl Flerovium 270	115 Uup Ununpentium 271	116 Lv Livermorium 273	117 Uus Ununseptium 274	118 Uuo Ununoctium 276																																																																																																																													

**Figure 4.1.** Composition of transition metal dichalcogenides (TMDs). Periodic table where the shaded areas highlight the transition metals and chalcogens which form the compounds  $MX_2$ .

ing to the stacking sequence a differentiation into polytypes can be accomplished. The commonly used notation is the Ramsdell's one [149] whereby stacking polytypic sequences are identified through the couple  $nY$ :  $n$  indicates the number of  $X-M-X$  slabs in a unit cell and  $Y$  denotes the lattice type which can be trigonal ( $T$ ), hexagonal ( $H$ ), or rhombohedral ( $R$ ). Not all combinations of  $n$  and  $Y$  exist. The only known polytype with one  $MX_2$  in a unit cell is trigonal ( $1T$ ), while three different polytypes have two  $MX_2$  layers per unit cell ( $2H_a$ ,  $2H_b$ ,  $2H_c$ ) and so forth for the other polytypes [150]. For example, a schematic representation of the  $CdI_2$ -type  $1T$  crystal structure is shown in Fig. 4.2, where the octahedral coordination around the metal atom is recognizable.

#### 4.1.1 Tantalum-based TMDs

Among TMDs, the tantalum-based compounds  $TaX_2$  with  $X = S$  or  $Se$  are of particular interest because they are host to coexisting strongly correlated phases including charge density waves (CDWs) and an unusual metal-insulator transition (MIT). These materials exhibit several CDW phases as incommensurate (IC-CDW), nearly-commensurate (NCCDW) and commensurate (CCDW), with transition temperatures over a broad range extending from 75 K up to 473 K [151].  $1T$ - $TaS_2$  forms a commensurate CDW phase at temperatures below 180 K. This state coexists with a Mott phase and it is characterized by a contraction of the 12



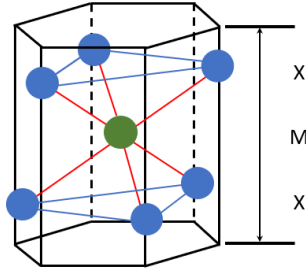


**Figure 4.2.** Schematic representation of the  $\text{CdI}_2$ -type  $1T$  sandwich structure: the transition metal atom (M) with a octahedral coordination is green, chalcogen atoms (X) are dark blue.

Ta atoms towards a central Ta one, represented by a  $\sqrt{13} \times \sqrt{13}$  supercell, which gives rise to a Star of David (SoD) configuration (see Fig.4.3). The formation of SoD units comes with a rotation of the new primitive lattice vectors of around  $13^\circ$  with respect to the original ones and this rotation is clearly observed by diffraction experiments [152]. By increasing the temperature above 180 K, the material undergoes a transition from the CCDW phase to a NCCDW, then from the NCCDW to an ICCDW at 350 K. Similar to  $1T\text{-TaS}_2$ , also in  $1T\text{-TaSe}_2$  the transition to the CCDW phase is accompanied by an in-plane periodic lattice distortion of  $\sqrt{13} \times \sqrt{13}$  dimensions and a rotation of  $13^\circ$  with respect to the original unit cell. However, in this sample, the NCCDW phase is not observed and there is just a direct transition from the CCDW to an ICCDW phase at 473 K [152]. Moreover, in contrast to  $1T\text{-TaS}_2$ , the transition to the CCDW phase does not come with a MIT. Signatures of a MIT in  $1T\text{-TaSe}_2$  have been observed at lower temperature: by means of surface-sensitive techniques probing the electronic structure such as ARPES [153] and STM [154] the opening of an electronic gap  $\Delta_{Mott}$  of about 250 meV across the whole Fermi surface has been found below about 260 K. It is also important to point out that bulk resistivity measurements as a function of the temperature indicate that  $1T\text{-TaSe}_2$  remains metallic [155] at all temperatures. Therefore, the observed MIT has been considered as a *surface* Mott insulating phase [153]. The CDW has been suggested to be a precursor to the Mott phase, because it causes a modification of the band structure, giving rise to a narrow half-filled band at the Fermi level and increasing the probability of electron localization [156]. In this regard, extended Huckel calculations [157] reveal that the CDW splits the Ta  $d$  conduction band into subbands hosting a total of 13 electrons per unit cell. Below the Fermi level, there are six subbands completely filled with 2 electrons/atom each. As a result, the Fermi surface consists of a half-filled subband carrying the thirteenth electron. By lowering the temperature, there is

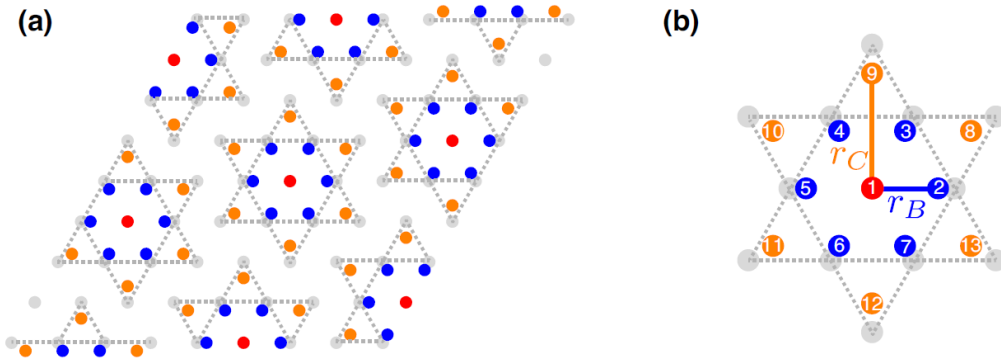


**Figure 4.3.** (a) Periodic lattice distortion (PLD) in the Star-of-David (SoD) configuration in real space (exaggerated). Red dots indicate the central Ta atoms, blue dots indicate the 6 Ta nearest neighbors, orange dots indicate the 6 Ta atoms forming the tips of the star, respectively. For reference, Ta atoms without PLD are shown by the gray dots; (b) parameters  $r_B$  and  $r_C$  characterizing the SoD configuration. Reprinted from Ikeda, T. N., Tsunetsugu, H., and Yonemitsu, K. (2019). Photoinduced Dynamics of Commensurate Charge Density Wave in 1T-TaS<sub>2</sub> Based on Three-Orbital Hubbard Model. *Applied Sciences*, 9(1), 70.

an increase of the CDW amplitude which in turn determines a narrowing of the bandwidth ( $W$ ), associated to the in-plane electron hopping between neighbouring SoD clusters in the CDW superlattice [156]. If the bandwidth ( $W$ ) decreases below a critical value, electrons will localize and the Mott criterion  $U/W \geq 1$  is fulfilled, where  $U$  is the on-site electron-electron Coulomb repulsion. As a consequence of this localization, the formation of a gap,  $\Delta_{Mott}$ , and the transition to an insulating state occur [153, 156].

Although considerable progress in the knowledge of these materials has been made, some questions about the origin of the Mott transition in the tantalum-based compounds and its connection to the CDW phase still await responses. In general, 1T-TaSe<sub>2</sub> has been studied far less than 1T-TaS<sub>2</sub>. However, if on the one hand 1T-TaS<sub>2</sub> exhibits a richer phase diagram, on the other it shows many phases in close proximity to each other and this makes the investigation of these questions more complicated, in particular, when trying to disentangle the relationship of the CDW with the Mott phase. On the contrary, 1T-TaSe<sub>2</sub> has recently identified to be a better platform to investigate these phenomena [158] because of the reduced complexity of its phase diagram, larger  $\Delta_{Mott}$  and well-separated temperatures between the CDW and Mott transitions.

Since the CDW phase is related to the electron-phonon interaction (see Paragraph 1.3.2), one can understand more about this phase by performing ultrafast time-

resolved measurements. More in detail, TR-ARPES enables one to resolve the electronic band structure and investigate the photo-induced suppression of the order parameter in real time as well as its recovery [159, 160]. Prior TR-ARPES investigations on 1*T*-TaSe<sub>2</sub> have used high-harmonics ( $\sim 22$  eV probe) with various repetition rates and energy resolution (260 meV [158], 130 meV [161]) and have either concentrated on the early stages ( $<300$  fs) of the dynamics, i.e., on the suppression of electronic and lattice order [158] or the room temperature phase (CCDW) without studying the Mott gap physics [161].

In the following, the results of our TR-ARPES and TRR experiments on 1*T*-TaSe<sub>2</sub> performed at Politecnico di Milano are shown. We have investigated the electronic and phonon dynamics of 1*T*-TaSe<sub>2</sub> up to several picoseconds at different temperatures and with unprecedented time and energy resolution [61] in comparison to other studies [158, 161]. Our findings emphasize that both the CDW and lattice degrees of freedom play an important role in stabilizing the Mott phase in 1*T*-TaSe<sub>2</sub>, clarifying the interplay between these coexisting phases.

### The band structure of 1*T*-TaSe<sub>2</sub>

The band structure of 1*T*-TaSe<sub>2</sub> in the normal phase along the  $\Gamma$ KM direction of the Brillouin zone is sketched in Fig. 4.4(a). The metal atom is Ta<sup>+4</sup> ionized, hence its configuration is 5*d*<sup>1</sup>. Therefore, only one (out of five) *d*-like band is partially filled (black line), the others being all above  $E_F$  (not shown). The chalcogen atom is Se<sup>-2</sup> ionized and, as a result, its 4*p* orbitals are all filled. Thus, *p*-like bands (red lines) lie below  $E_F$ .

Below 473 K, the CCDW phase sets in. Periodic lattice distortion (PLD) mostly affects the Ta layer [162], inducing strong band folding of the 5*d*-like bands. The SoD cluster involves 13 Ta atoms. Therefore, the 13 5*d*<sup>1</sup> electrons form six filled bands with weak dispersion and one half-filled band crossing  $E_F$ , (blue lines in Fig. 4.4(b)). These flat bands indicate strong 5*d* electron localization, thus poor mobility. Around the  $\Gamma$  point, the Ta5*d* and Se4*p* bands overlap and *p*-*d* hybridization might become relevant. The weak PLD of Se atoms [162], however, suggest a weak or negligible folding of *p*-like bands with respect to the 5*d*-like ones.

Below  $\sim 260$  K, ARPES data show the formation of a gap at  $E_F$  [153], attributed to Mott metal-insulator transition that splits the flat 5*d* half-filled band into lower (LHB) and upper (UHB) Hubbard bands (green lines in Fig. 4.4(c)). Despite the gap, some ARPES spectral weight remains at  $E_F$  in agreement with metal-like resistivity data [155]. Ref. [163] suggests that the *p*-like band at  $\Gamma$  crosses  $E_F$ , explaining ARPES and resistivity measurements. Ref. [164] infers a 2D in-layer insulating behavior and a 1D normal-to-layer metallic one (with a Fermi surface along the  $\Gamma$ A direction, parallel to  $k_z$ ) in 1*T*-TaS<sub>2</sub>, but no similar evidence is reported to date on 1*T*-TaSe<sub>2</sub>.

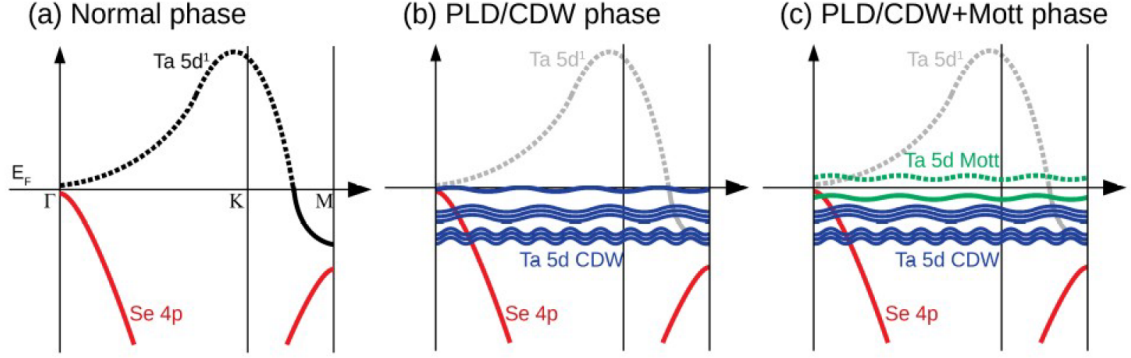


**Figure 4.4.** Schematic representation of the band structure of  $1T$ -TaSe<sub>2</sub> along the  $\Gamma$ KM direction of the Brillouin zone. (a) Normal phase. (b) Commensurate CDW phase, below 473 K. (c) Commensurate CDW and coexisting Mott phase, below about 260 K.

## 4.1.2 Preparation and characterization of $1T$ -TaSe<sub>2</sub> single crystals

### Crystal growth

The crystal growth process was carried out at the University of Bath (United Kingdom) by the group of Prof. Enrico Da Como.  $1T$ -TaSe<sub>2</sub> single crystals were grown by chemical vapour transport (CVT) using anhydrous iodine as a transport agent. In this regard, iodine has proven to be especially effective for the growth of the metallic TMDs [165]. The technique is based on the reaction between high-purity tantalum (99.9 %) and selenium (99.9 %) powders, together with pellets of anhydrous iodine (99.9 %) inside an evacuated quartz ampoule. In order to reach the ideal stoichiometry, an excess of selenium ( $\sim 3 \text{ mg cm}^{-3}$ ) was added [166]. For  $\sim 21$  days, the temperature of the quartz ampoule has been kept constant at  $960^\circ$ . Then, the metastable  $1T$  phase was obtained by quenching the ampoule in water from high temperature. In this way, single crystals with lateral dimensions of a few mm were grown. Moreover, the samples showed the metallic gold colour typical of  $1T$ -TaSe<sub>2</sub>, as reported in Fig. 4.5.

### Electronic transport

In order to characterize the  $1T$ -TaSe<sub>2</sub> samples, different techniques were used. Firstly, bulk resistivity measurements as a function of temperature were performed. The resulting trend of normalized electrical resistance in the temperature range of (4 - 300) K is shown in Fig. 4.6(a). By a first inspection, an overall metallic behaviour can be recognized, which is similar to the one observed in Ref. [151].

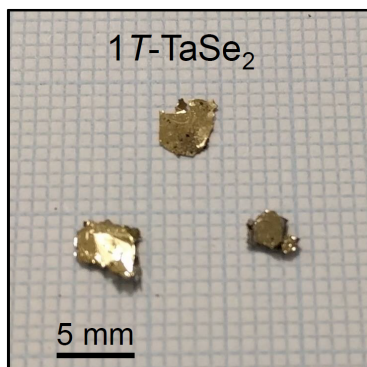


**Figure 4.5.** Image of typical  $1T$ -TaSe<sub>2</sub> single crystals used for our TR-ARPES measurements from Ref. [6].

Furthermore, by looking at the first derivative of resistance  $dR/dT$  in Fig. 4.6(b), it is not possible to recognize any experimental evidence of a metal-insulator transition. On the contrary, surface-sensitive angle-resolved photoemission spectroscopy experiments performed by Perfetti *et al.* [153] give evidence for a Mott transition at the  $1T$ -TaSe<sub>2</sub> surface. This suggests that the transition to an insulating behaviour occurring at about 260 K only involves the surface of the sample, which remains metallic in the bulk.

### LEED measurements

Before performing TR-ARPES measurements, the orientation of the  $1T$ -TaSe<sub>2</sub> crystal was determined by low-energy electron diffraction (LEED). The result of our LEED measurement on  $1T$ -TaSe<sub>2</sub> is shown in Fig. 4.7. The diffraction pattern reveals the hexagonal symmetry of the sample, where the spot separation is of  $\sim 720$  pixels, as indicated by the red line. Weak secondary spots, separated by a distance of  $\sim 200$  pixels, were recognized in correspondence of each corner (blue lines). As theoretically expected for the CDW phase [151, 167], the ratio between the two spot separations is  $720 \text{ pixels} / 200 \text{ pixels} = 3.6 \approx \sqrt{13}$  and the secondary hexagon is rotated by  $\sim 13^\circ$  with respect to the primary. Therefore, the weaker spots originate from the  $\sqrt{13}a_0 \times \sqrt{13}a_0$  superlattice with  $\sim 13^\circ$  rotation. This LEED pattern was acquired at 77 K but the same features were also seen at room temperature.

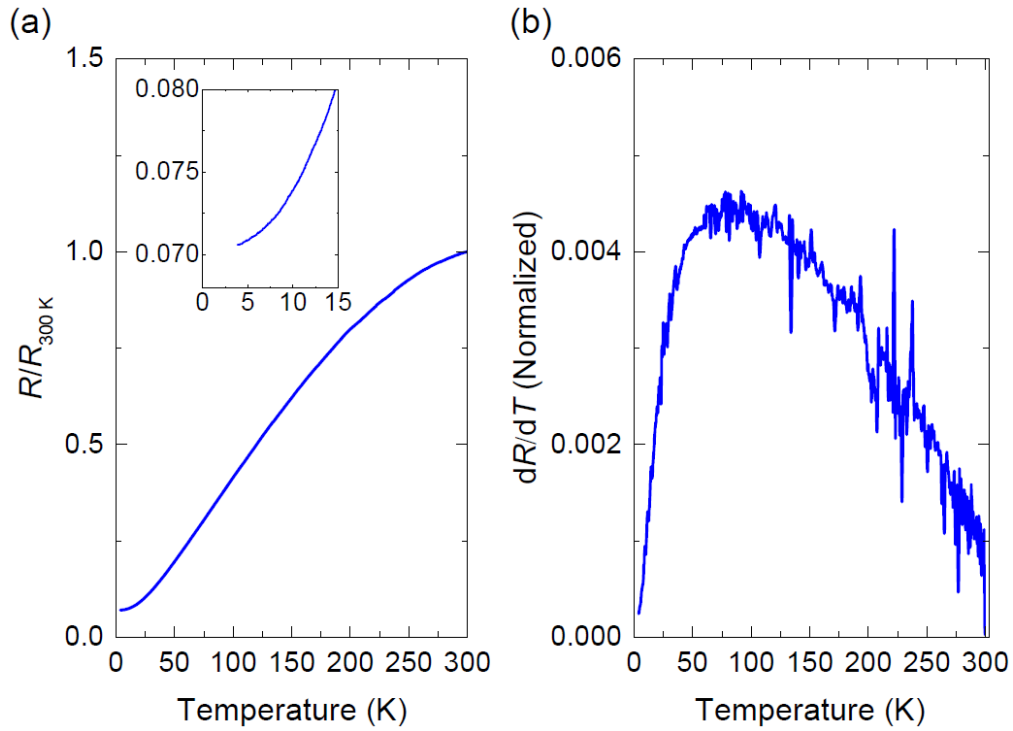


**Figure 4.6.** Bulk resistivity measurements performed at the University of Bath (United Kingdom) from Supplemental material of Ref. [6]. (a) Normalized electrical resistance as a function of temperature. In the inset, the low temperature ( $< 15$  K) range is reported. (b) First derivative of resistance,  $dR/dT$ .

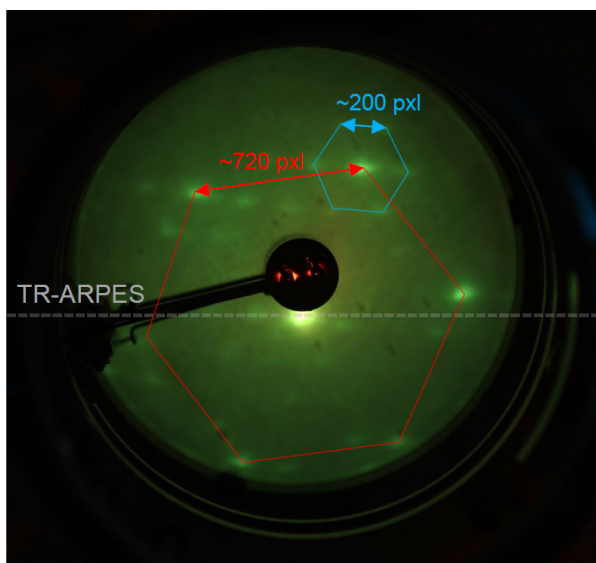


**Figure 4.7.** LEED pattern from Ref. [6] obtained on a  $1T$ -TaSe<sub>2</sub> single crystal, which was mounted on the sample holder in the photoemission chamber at the temperature of 77 K. This image was acquired before TR-ARPES measurements in order to determine the sample orientation.

## 4.2 Steady-State and Time-Resolved Investigations on $1T$ -TaSe<sub>2</sub>

In this section, we will present the electronic structure of  $1T$ -TaSe<sub>2</sub> and the effects of CDW and Mott transitions. Firstly, we will show the full-wavevector ARPES images acquired at Bristol NanoESCA Facility, which provide the main features of the electronic structure of  $1T$ -TaSe<sub>2</sub>. Then, the results of the TR-ARPES and TRR measurements will be reported and discussed. All the technical and experimental aspects have been described in detail in Ref. [61].

### 4.2.1 Full-wavevector ARPES

Steady-state ARPES measurements were performed at the Bristol NanoESCA facility using He-I $\alpha$  radiation ( $h\nu = 21.2$  eV), with  $\sim 50$  meV energy resolution at 40 K. Fig. 4.8 shows the full in-plane projection of the BZ ARPES images of  $1T$ -TaSe<sub>2</sub> at specific binding energies, i.e.  $E_B = E_F - 0.5$  eV,  $E_B = E_F - 0.3$  eV and  $E_B = E_F$ . In Fig. 4.8(a) a sketch of the hexagonal BZ of the undistorted lattice is overlapped with the high-symmetry points labelled. On the BZ edges around the  $\bar{M}$  points, elliptical Ta-5d electron pockets can be recognized, while at the  $\bar{\Gamma}$  point, namely the center of the BZ, there is the Se-4p electron pocket,

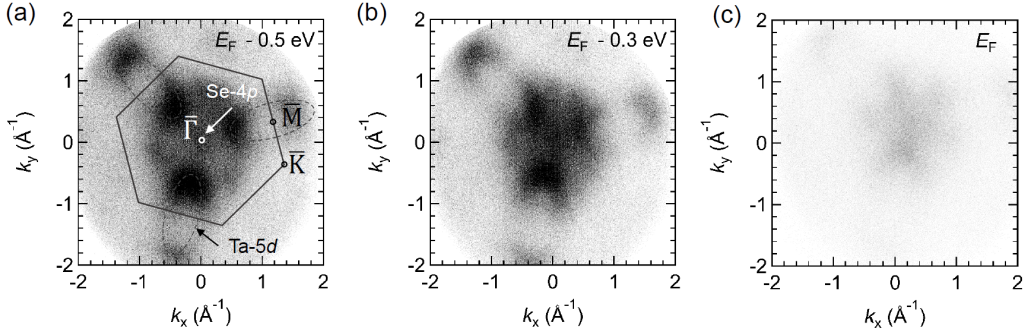


**Figure 4.8.** Full-wavevector ARPES ( $h\nu = 21.2$  eV) images of  $1T$ -TaSe<sub>2</sub> at specific binding energies and at 40 K from Supplemental material of Ref. [6]. (a) Electronic structure at  $E_B = E_F - 0.5$  eV. The black line indicates the hexagonal BZ, while grey dashed ellipses point out the Ta-5d derived electron pockets. The labelled high-symmetry points are a projection onto the experimental  $k_z$ . (b) Electronic structure at  $E_B = E_F - 0.3$  eV (c) Electronic structure at the Fermi level  $E_F$ .

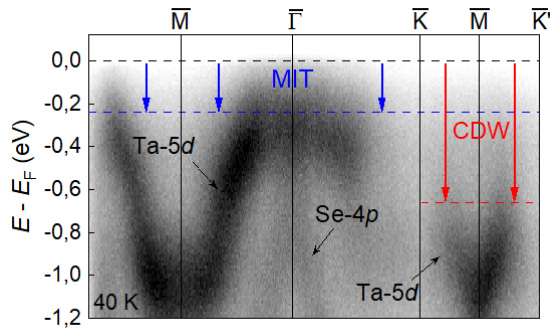


**Figure 4.9.** Band dispersions through the BZ from Supplemental material of Ref. [6]. The CDW gap opens up at the  $\bar{M}$  point as indicated by the red vertical arrow. The Mott gap extends across all  $k$  space as marked by the blue vertical arrow.

in accordance to previous ARPES studies [167, 168]. On the parallel arms of the Ta-5d pockets, there is a loss of intensity where the CDW gap is expected to appear [155]. Panel (b) of Fig. 4.8 displays the full-wavevector ARPES image acquired at  $E_B = E_F - 0.3$  eV and, apparently, the electronic structure is still distinctly visible. Finally, at the Fermi level  $E_F$ , shown in Fig. 4.8(c), there is almost a total loss of intensity across the BZ. The latter result indicates that the whole Fermi surface is suppressed by the formation of a gap uniform on the entire BZ because of the occurrence of the metal-insulator Mott transition.

Fig. 4.9 shows the band dispersion acquired along the  $\bar{M}$ - $\bar{\Gamma}$ - $\bar{K}$ - $\bar{M}$ - $\bar{K}$  direction of the BZ at 40 K and the main features are emphasized, such as the Ta-5d and Se-4p derived bands. Dispersion through the electron pocket along the  $\bar{K}$ - $\bar{M}$ - $\bar{K}$  direction gives evidence for a lowering of the band edge below the Fermi level  $E_F$  as a consequence of the CDW gap,  $\Delta_{CDW}$ . From the band dispersion along the



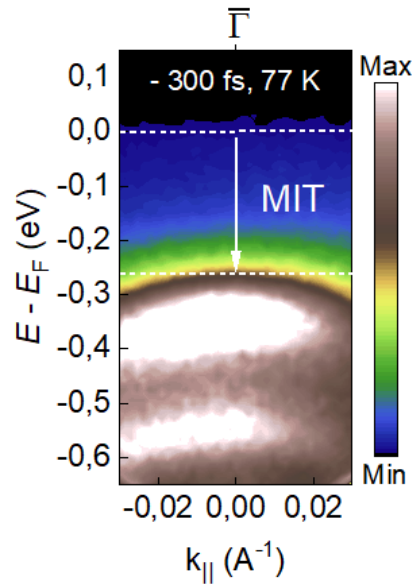


**Figure 4.10.** ARPES intensity map at 77 K and at negative pump-probe delay measured at Politecnico di Milano by using 6 eV probe photon energy from Ref. [6].

$\bar{M}$ - $\bar{\Gamma}$  direction, it is clear that all bands near  $E_F$  have been lowered by  $\sim 250$  meV because of a Mott gap,  $\Delta_{Mott}$  which extends across the whole BZ.

#### 4.2.2 TR-ARPES and TRR on 1T-TaSe<sub>2</sub>

Fig. 4.10 shows the ARPES intensity map of 1T-TaSe<sub>2</sub>, acquired at Politecnico di Milano by using  $h\nu = 6$  eV photon energy, at 77 K around the  $\bar{\Gamma}$  point before pump arrival (-300 fs). According to the low-energy electron diffraction (LEED) pattern, the measured dispersion is roughly along the  $\bar{M}$ - $\bar{\Gamma}$ - $\bar{M}$  direction. As we can see, the band edge is placed below the Fermi level  $E_F$  as a consequence of the Mott metal-insulator transition.

Let us now consider the temporal evolution of the valence band at the  $\bar{\Gamma}$  point and at 77 K, which is reported in Fig. 4.11. Panel (a) displays the TR-ARPES spectra of the valence band acquired by using  $1.10 \text{ mJ cm}^{-2}$  pump fluence. As highlighted in Fig. 4.11(b), in correspondence to the perturbation by the pump pulse at  $t = 0$ , there is a fast reduction of valence band intensity which is followed by a recovery within  $\sim 2$  ps. An analogous temporal evolution has been observed in the Mott phase of 1T-TaS<sub>2</sub> [169]. The time invariance of the Mott gap  $\Delta_{Mott}$  indicates that the Mott phase is stable. Furthermore, notice that  $1.10 \text{ mJ cm}^{-2}$  pump fluence is not enough for melting the CDW [170], therefore we conclude that the TR-ARPES measurements were carried out in a perturbative regime where both CDW and Mott phases are preserved.

The dynamics of the valence band edge is reported in Panel (c) of Fig. 4.11, from

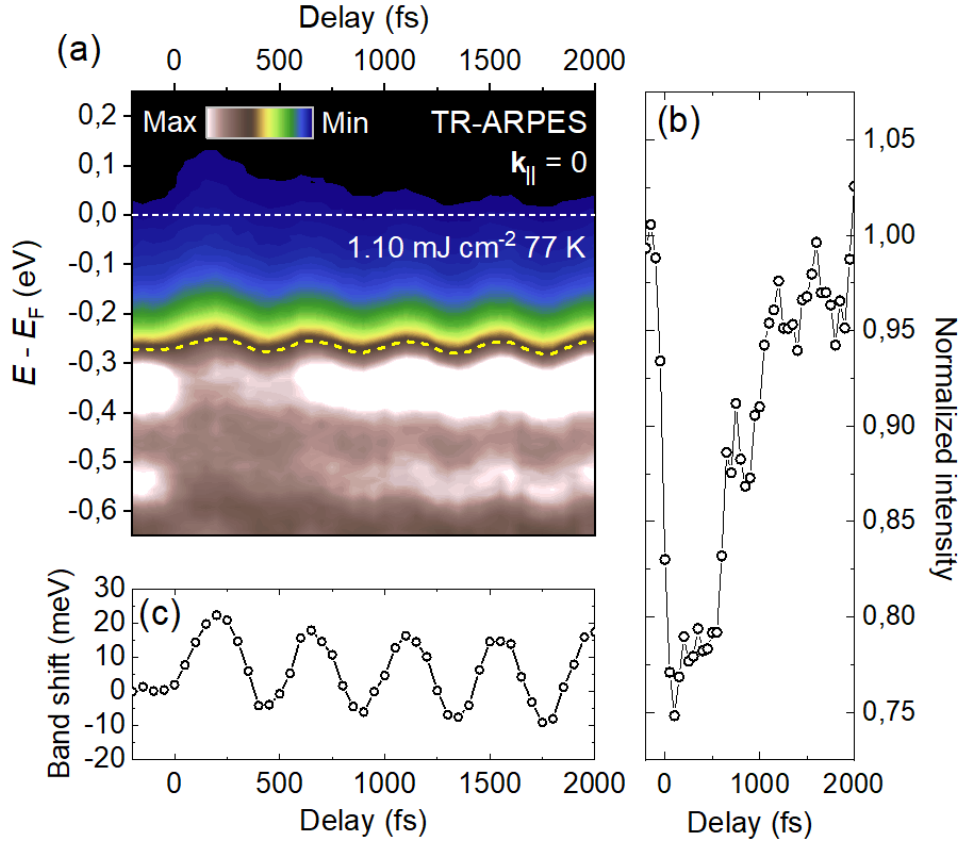


**Figure 4.11.** Temporal evolution of the valence band in the CDW-Mott phase from Ref. [6]. (a) TR-ARPES spectra at the  $\bar{\Gamma}$  point (77 K) acquired by using  $1.10 \text{ mJ cm}^{-2}$  pump fluence. (b) Normalized valence band intensity, extracted from the maximum near  $E - E_F \approx -0.35 \text{ eV}$ . (c) Shift of the valence band extracted from a constant intensity contour in panel (a), identified by the yellow dashed line.

which we can deduce that weakly damped strong coherent oscillations are triggered by the pump pulse. Fig. 4.12 compares the TR-ARPES and TRR measurements (Panels (a) and (b)). TR-ARPES data in Panel (a) give evidence for clear oscillations at a single frequency lasting up to 6 ps with a maximum initial amplitude of about  $\pm 20 \text{ meV}$  around the equilibrium position. The data were fitted with a damped periodic function given by  $E(t) = A \exp(-t/\tau_d) \sin(2\pi\nu t + \phi)$ , obtaining a frequency  $\nu \approx (2.19 \pm 0.01) \text{ THz}$  and a damping time  $\tau_d$  of about  $(6.3 \pm 1.0) \text{ ps}$ . These oscillations have also been observed in the Mott phase of  $1T\text{-TaS}_2$  [169, 171] and from theoretical calculations it is known that it is the CDW amplitude mode, related to the in-plane breathing mode of the SoD [172]. This mode consists of a coherent movement of the Ta atoms belonging to the same star of David where the

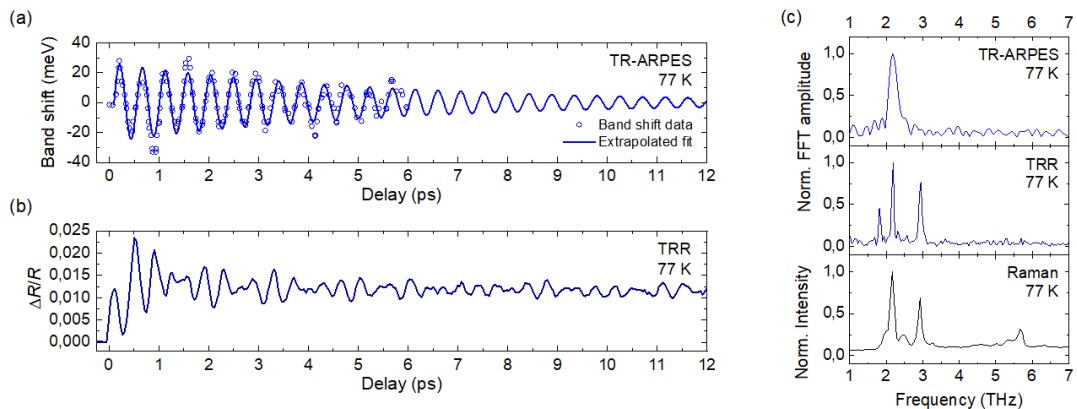


**Figure 4.12.** Coherent phonon oscillations in the CDW-Mott phase from Ref. [6]. (a) Oscillatory component of the valence band shift measured by TR-ARPES ( $1.16 \text{ mJ cm}^{-2}$ ). (b) Differential reflectivity signal measured by TRR ( $0.11 \text{ mJ cm}^{-2}$ ), where  $\Delta R/R$  is the absolute value of the differential reflectivity. The reported data are for  $1.84 \text{ eV}$  probe photon energy. (c) Normalized fast Fourier transform (FFT) amplitude of the TR-ARPES and TRR oscillatory components, together with the Raman spectrum for comparison.

central Ta atom remains fixed during the oscillation. The fast Fourier transform of the TR-ARPES signal reported in Fig. 4.12(c) (top panel) reveals a sharp peak at  $2.2 \text{ THz}$ . Therefore, we conclude that the binding energy of the valence band edge in  $1T\text{-TaSe}_2$  is modulated by the CDW amplitude mode. This result agrees with the scenario in which the CDW amplitude, which is associated with the magnitude of the in-plane periodic lattice distortion, determines the  $U/W$  ratio by affecting the electron hopping between adjacent stars-of-David [154, 156, 158, 173, 174]. Thus, the coherent oscillations of the CDW amplitude mode, triggered by the pump pulse, induces a modulation of the  $U/W$  ratio which reveals the magnitude of the Mott gap  $\Delta_{Mott}$ .

Panel (b) of Fig. 4.12 shows the temporal evolution of the differential reflectivity  $\Delta R/R$  of  $1T\text{-TaSe}_2$  acquired at  $77 \text{ K}$  by performing TRR measurements. The data refer to  $1.84 \text{ eV}$  probe photon energy. The dynamics of  $\Delta R/R$  is characterized by strong oscillations which are weakly damped. However, differently from the single frequency modulating the valence band observed by TR-ARPES, the oscillations of the TRR signal are due to multiple frequencies. This is clearly visible from the FFT of  $\Delta R/R$  reported in Fig. 4.12(c) that discloses three phonon modes at  $\sim 1.8$ ,  $2.2$  and  $2.9 \text{ THz}$ , in agreement with the Raman spectrum shown in Fig. 4.12(c) and previously displayed in other works [175, 176]. The  $\sim 1.8 \text{ THz}$  mode is absent in our Raman spectrum because the cut-off of the spectrometer laser filter falls at higher frequencies. Another feature to note is that the  $2.2 \text{ THz}$  phonon mode

in the FFT of the TR-ARPES data is broader as a consequence of the shorter sampling interval of the oscillations.

Since in our TR-ARPES and TRR measurements comparable pump photon energies and pulse durations are used, we expect that more than one Raman-active  $\Gamma$ -point phonon modes are triggered in both cases. Nevertheless, in light of its energy-momentum selectivity, TR-ARPES provides information about the local electronic band structure of the valence band at the  $\bar{\Gamma}$  point. Therefore, the CDW amplitude mode is clearly visible by both techniques. However, time resolved reflectivity shows two additional modes, which are absent in TR-ARPES because they are not able to influence the valence band binding energy as the CDW amplitude mode is able to do. We conclude that the Mott phase is especially linked to that particular mode.

### 4.2.3 Temperature dependence of coherent phonons in the CDW phase

Let us now consider the results of our temperature-dependent TRR and Raman measurements. The aim of these experiments was to study the behavior of the phonon modes across the CDW transition at  $T_{CDW}$ . Panels (a) and (b) of Fig. 4.13 provide a comparison between the FFT of the differential reflectivity signal and the Raman spectra measured over the 295-478 K temperature range. In Panel (a) of Fig. 4.13, the FFT of the transient reflectivity  $\Delta R/R$  signal shows multiple frequencies at 295 K, analogous to the TRR data at 77 K. More in detail, two phonon peaks at  $\sim 2.0$  and  $2.7$  THz are present corresponding to the two highest intensity phonon modes with frequencies of  $\sim 2.2$  and  $2.9$  THz measured at 77 K (Fig. 4.12 (c)): they appear here at slightly lower frequencies due to the higher temperature of the sample. This phenomenon which consists in a reduction of the phonon frequencies by increasing the temperature of the material is known as *phonon mode softening* [6, 176]. In Fig. 4.13(a), a different behavior as a function of the temperature of the two phonon modes can be observed using  $0.11 \text{ mJ cm}^{-2}$  fluence. The amplitude of the  $\sim 2.0$  THz phonon mode decreases rapidly, disappearing for  $T \geq 450$  K. Differently, the  $\sim 2.7$  THz phonon mode is detectable up to the temperature of the ICCDW-CCDW transition, i.e.  $T_{CDW} = 473$  K. Raman spectra in Fig. 4.13(b) show multiple phonon frequencies at the low temperatures. By heating the sample, the intensities of all modes gradually decrease until they completely disappear above  $T_{CDW}$ . In order to point out the difference in the temperature dependence of the phonon mode intensities obtained by the two types of measurements, the trend of the integrated peak area for the 2.0 THz amplitude and 2.7 THz modes in TRR and Raman spectra is shown. Panels (c) and (d) of Fig. 4.13 display the comparison for the TRR-FFT and Raman spectra, respectively.

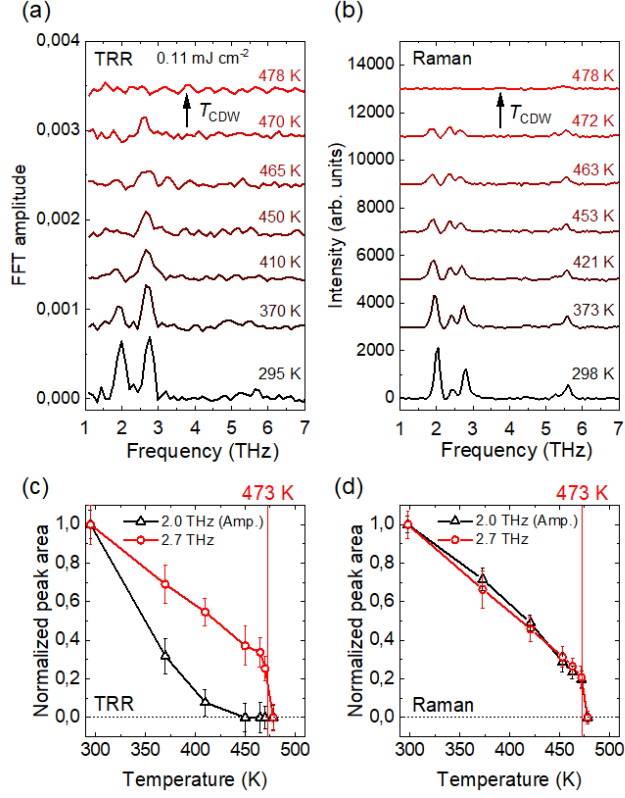


**Figure 4.13.** Temperature dependence of coherent phonons in the CDW phase from Ref. [6]. (a) FFT of the transient reflectivity  $\Delta R/R$  signal measured by TRR using  $0.11 \text{ mJ cm}^{-2}$  fluence in the range 295–478 K. The reported data is for 1.89 eV probe photon energy. (b) Raman spectra measured over a similar temperature range as panel (a) for comparison. Panels (c) and (d) display the temperature dependence of the integrated peak area for the 2.0 amplitude and 2.7 THz modes in the TRR-FFT and Raman spectra, respectively.

In Fig. 4.13(d), where the Raman normalized peak areas are shown, for both the  $\sim 2.0$  and 2.7 THz modes, a steep onset at  $T_{CDW}$  followed by a linear temperature dependence is evident. Therefore, both the  $\sim 2.0$  and 2.7 THz modes exhibit the expected first-order nature of the CDW transition. On the contrary, in TRR reported in Fig. 4.13(c), only the  $\sim 2.7$  THz mode exhibits a first-order behavior, remaining robust up to  $T_{CDW}$ . The  $\sim 2.0$  THz amplitude mode in TRR is suppressed and deviates from the expected trend. The latter behavior suggests that a transient photoinduced melting of the CDW amplitude occurs. This comparison of the temperature dependence of coherent phonons across the CDW transition suggests that the amplitude mode is more easily suppressed during perturbation of the CDW state by the optical excitation with respect to other modes. There-

fore, we conclude that the  $\sim 2.0$  THz CDW amplitude mode is strongly coupled to electrons and very sensitive to photoexcitation.

#### 4.2.4 Experimental hints of dimerization in 1T-TaSe<sub>2</sub>

In Paragraph 4.2.2, we have investigated by time- and angle-resolved photoemission spectroscopy (TR-ARPES) and time-resolved reflectivity (TRR) the electron and phonon dynamics of 1T-TaSe<sub>2</sub> at low temperature (77 K) where the commensurate CDW and Mott phases coexist, finding that the Mott phase is preferentially linked to the in-plane CDW amplitude mode. Subsequently, as discussed in Paragraph 4.2.3, we have performed temperature-dependent TRR and Raman measurements over the 295-478 K temperature range, concluding that the CDW amplitude mode is strongly coupled to the electronic degrees of freedom and very sensitive to the optical excitation.

In this paragraph, we discuss temperature-dependent TR-ARPES measurements on 1T-TaSe<sub>2</sub>, which were carried out by varying the sample temperature within the commensurate CDW phase. We found a change of spectral weights in ARPES spectra as well as a phonon splitting of the CDW amplitude mode at low temperature that point at a dimerization process in 1T-TaSe<sub>2</sub>.

Photoemission spectra of 1T-TaSe<sub>2</sub> at 300 K and 85 K before pump arrival are shown in Fig. 4.14(a). By a first inspection, it is evident that, lowering the temperature from 300 K to 85 K, a variation of spectral weights occurs. In Fig. 4.14(b), the comparison between the energy dispersion curves (EDCs) at these temperatures, obtained by cutting the corresponding ARPES map at  $k_{\parallel} = 0$ , is reported. The presence of the Mott gap of about 250 meV both at 300 K and 85 K can be recognized. However, at 300 K there is a single broad peak, whereas at 85 K there are two peaks separated by 0.2 eV. The dynamics of the band edge after pumping at both temperatures is shown in Fig. 4.14(c). There are damped oscillations but, in addition, at 85 K there is also a phonon beating. Therefore, by lowering the temperature, there are variations in both the band structure and oscillations. In the following, we show how these results can be explained by assuming the occurrence of a dimerization process in 1T-TaSe<sub>2</sub>, by analogy to 1T-TaS<sub>2</sub>. Recent theoretical and experimental studies [177, 178] have demonstrated that a correct understanding of the phase transitions in 1T-TaS<sub>2</sub> is possible only by assuming the existence of interlayer interaction. Ref. [177] investigates the vertical stacking of S-Ta-S layers by first-principles calculations based on density functional theory (DFT), finding that interlayer coupling changes with the stacking sequence and affects the electronic structure and phase transition of 1T-TaS<sub>2</sub>. More in detail, they demonstrated that the only way to explain the experimental results about the electronic band structure of this material is to assume that there is a dimerization, namely, a double-layer stacking in the direction perpendicular to the S-Ta-S

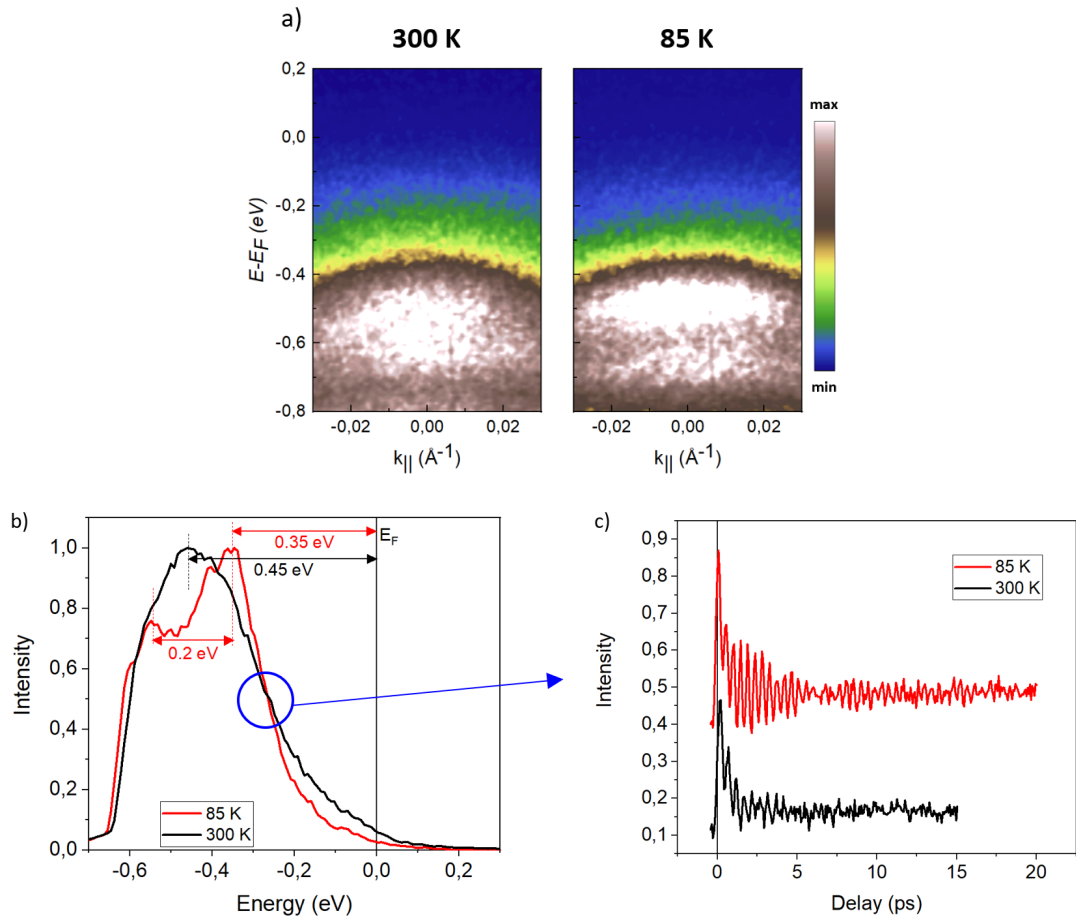


**Figure 4.14.** Temperature-dependent TR-ARPES measurements. (a) ARPES maps of 1T-TaSe<sub>2</sub> at 300 K (on the left) and 85 K (on the right) before pump arrival (-300 fs). (b) Comparison of energy dispersion curves extracted from the  $\Gamma$  point ( $k_{||} = 0$ ) at 300 K (black line) and 85 K (red line). (c) EDCs extracted from  $\Gamma$  point at 300 and 85 K are reported again; on the right, the temporal evolutions of the band edge ( $E = -0.26$  eV) are shown.

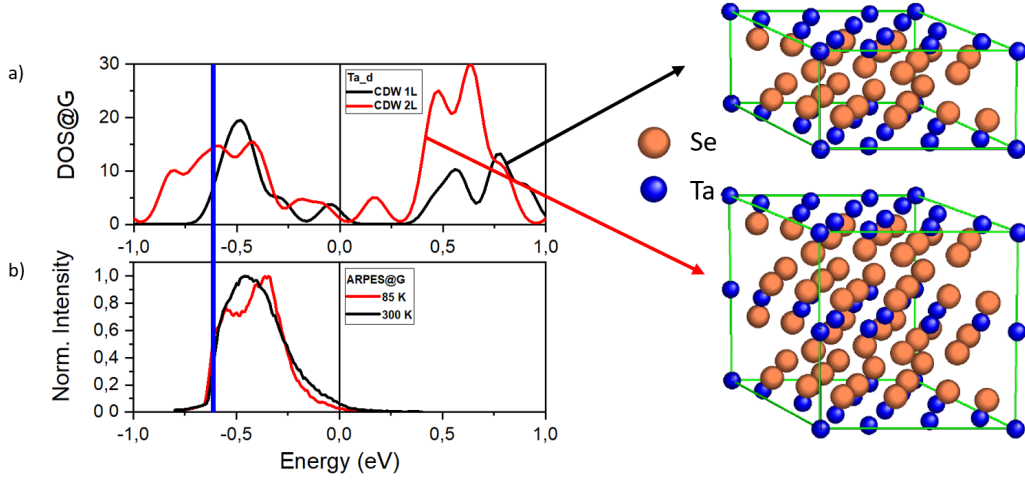


**Figure 4.15.** (a) DFT simulations of the charge density wave phase. The black curve refers to the one-layer per unit cell case, while the red curve to the two-layer per unit cell one. The two configurations of unit cell are indicated by the black and red arrows with the same criterion. (b) EDCs extracted from  $\Gamma$  point at 300 and 85 K.

layer. In a similar manner, we have identified some hints of dimerization also in  $1T$ -TaSe<sub>2</sub> on the basis of our TR-ARPES measurements.

Firstly, preliminary DFT simulations of the CDW phase were performed with Quantum Espresso (see Paragraph 4.2.5). Since many atoms per unit cell are involved, only the band structure at the  $\Gamma$  point was calculated and in Fig. 4.15(a) the corresponding estimated density of states (DoS) is shown. The black curve refers to the one-layer per unit cell case, while the red curve refers to the use of a doubled unit cell along the z-axis that include two layers. The corresponding atomic structures are shown on the right. From calculations, it is evident that doubling the unit cell normal to the layer modifies the interlayer coupling and affects the density of states, which now resembles our ARPES results in Fig. 4.14(b) reported again in Fig. 4.15(b). The vertical blue line on the two panels marks the low energy cut-off of our measurements. By comparing the calculated DoS at the  $\Gamma$  point with the measured EDCs, we can identify a match between the one-layer configuration and the 300 K case as well as between the two-layer configuration and the 85 K case. This result can be considered as a first hint of the occurrence of dimerization in  $1T$ -TaSe<sub>2</sub> by lowering the temperature from 300 K to 85 K.

A second hint of dimerization can be identified by considering the photo-induced dynamics of the band edge at 300 K and 85 K (Fig. 4.14(c)). In order to properly model our data, all incoherent contributions (such as the slowly varying back-



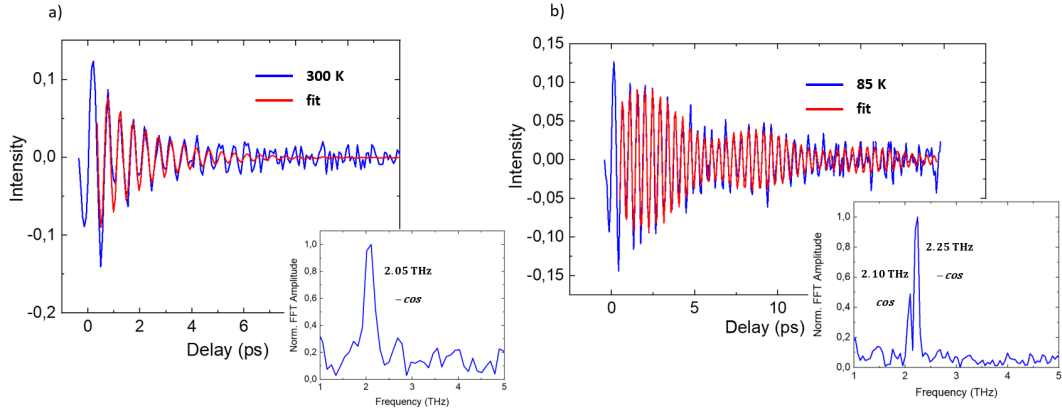


**Figure 4.16.** Temporal evolution of the band edge. (a) Oscillation at 300 K (15 mW pump power): experimental data are indicated by the blue curve, the fitting curve by the red curve. In the inset, the FFT of the signal shows one phonon peak at 2.05 THz, confirming the results of the fit. The phase of this phonon mode is minus cosine. (b) Oscillation at 85 K (12 mW pump power): experimental data are indicated by the blue curve, the fitting curve by the red curve. Also in this case, the FFT of the signal agrees with the fit results, showing two phonon peaks at 2.10 and 2.25 THz with opposite phases.

ground) have been removed, obtaining the blue curves in Fig. 4.16. The resulting oscillations are fitted with two damped harmonic modes, getting the overlapped red curves. As shown in Fig. 4.16(a), at 300 K the fit reveals only one mode with a minus cosine behavior and frequency of 2.05 THz. Differently, at 85 K in Fig. 4.16(b), there are two phonon modes at slightly different frequencies, in agreement with the FFT in the inset, with opposite phases. Therefore, from this analysis of the dynamics of the band edge, one can conclude that by lowering the temperature a phonon mode splitting occurs. It is possible to demonstrate that also this splitting can be ascribed to the occurrence of dimerization.

We will employ a simple one-dimensional harmonic lattice model implemented in Mathematica. Referring to Fig. 4.17(a), the CCDW lattice distortion leads to the formation of SoD that involves 13 Ta atoms: the central one (blue), 6 nearest neighbours (green) forming the inner green shell and 6 next nn (red) forming the outer red shell. In a simplified 1D model, this can be represented by the 5 atoms shown in Panel (b): the color-code is the same used in the SoD picture and recalls the corresponding shells. One can imagine the 5 Ta atoms connected by springs as shown in Fig. 4.17(b). The latter displays the one-layer per unit cell configuration, where the  $h$ ,  $l$  and  $k$  spring constants are similar to one another ( $h \approx l \approx k$ ). Even though this model is a one-dimensional picture, it is able to reproduce an amplitude mode in one-dimension by analogy to the two-dimensional case. The

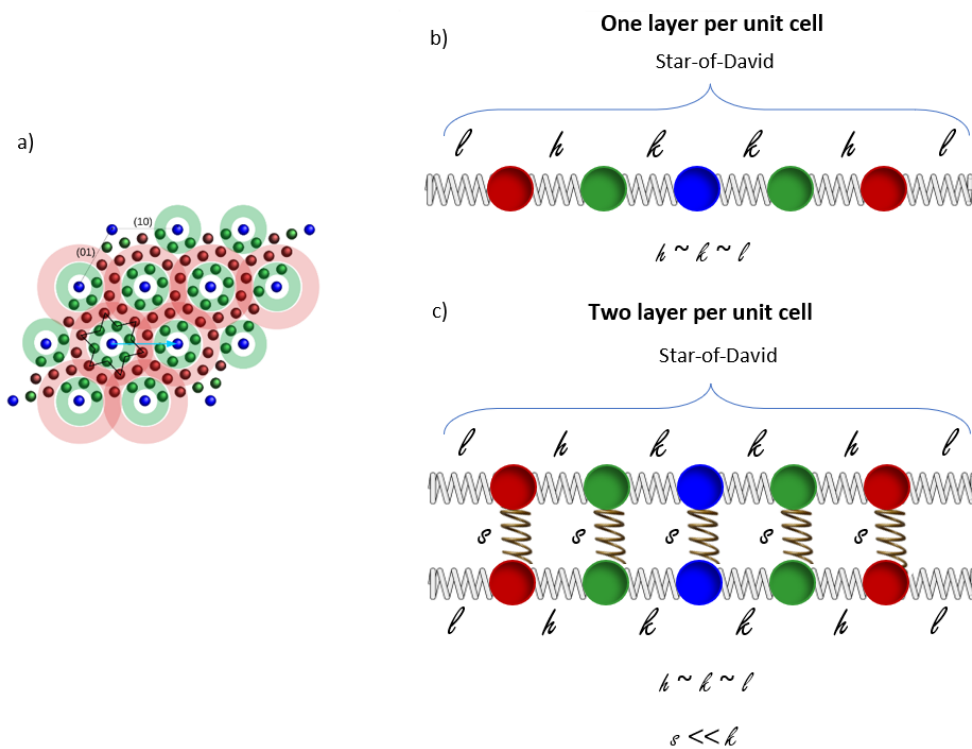


**Figure 4.17.** One-dimensional harmonic lattice model. (a) A Ta-plane where the 13 Ta atoms clusters - stars of David - are shown. They can be divided in the central Ta atom (blue), the 6 Ta nearest neighbors ring (green) and the 6 Ta forming the tips of the stars (red). (b) One-layer per unit cell configuration: the 5 Ta atoms placed along a high symmetry direction are connected by springs, where the  $h$ ,  $l$  and  $k$  spring constants are similar to one another. (c) Two-layers per unit cell configuration: the presence of an interlayer coupling is taken into account by adding the  $s$  spring constant.

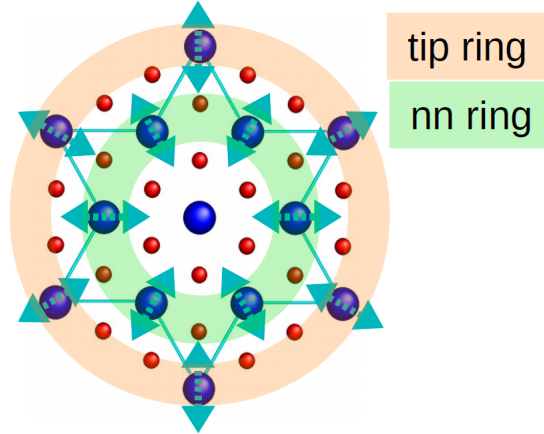


**Figure 4.18.** CDW amplitude mode. It consists of a coherent movement of the Ta atoms belonging to the same star of David where the central atom is not moving. Ta and Se atoms are indicated by blue and red circles, respectively. The nn ring involves the 6 nearest neighbours Ta atoms, while the tip ring is composed of the 6 next nearest neighbours Ta atoms. The light blue arrows emphasize their radial motion.

in-plane CDW amplitude mode involves a synchronous radial motion of the Ta atoms belonging to the same star of David where the central Ta atom remains fixed during the oscillation (Fig. 4.18). This is a fully symmetric  $A_{1g}$ -like mode, typically detected in Raman spectroscopy. We now include the dimerization, by adding the  $s$  spring constant as indicated in Fig. 4.17(c). Since the intralayer coupling is stronger than the interlayer one, the  $s$  spring constant is smaller than the others. Furthermore, since the model is one-dimensional, the  $s$  spring acts parallel to  $h$ ,  $l$  and  $k$ : in other words, it couples one-dimensional neighbour cells, simulating the interlayer coupling between SoDs in the three-dimensional system. In this case, two modes with slightly different frequencies and opposite phases, which resemble the two phonon modes experimentally observed at 85 K (4.16(b)), appear. These two modes are the result of the splitting of the CDW amplitude mode: one phonon mode corresponds to the in-phase oscillations of two neighboring stars of David, while the other one is related to out-of-phase oscillations of two neighboring stars of David, as shown in Fig. 4.19. For a ratio  $s/k = 0.084$ , one obtains a frequency  $\nu = 2.14$  THz for the in-phase amplitude mode, while  $\nu = 2.27$  THz for the out-of-phase amplitude mode, resulting in a frequency splitting similar to the one experimentally observed.

Therefore, by assuming that the one-layer per unit cell configuration corresponds to the 300 K case and that the double layer per unit cell configuration corresponds to the 85 K one, one can deduce that, by lowering the temperature, a dimeriza-

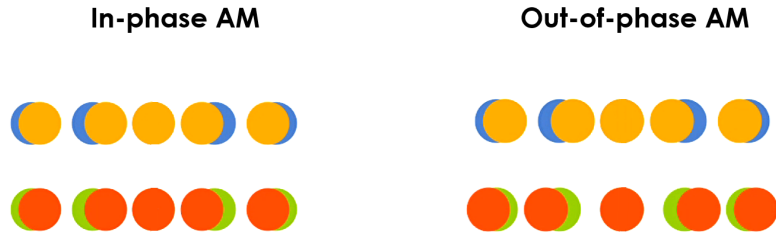


**Figure 4.19.** Splitting of the CDW amplitude mode (AM) with slightly different frequencies and opposite phases as a consequence of dimerization. On the left, a snapshot of the in-phase oscillations of two neighboring stars of David (in-phase AM). On the right, a snapshot of the out-of-phase oscillations of two neighboring stars of David (out-of-phase AM). These modes resemble the two phonon modes experimentally observed at 85 K (4.16(b)).

tion takes place and, as a consequence, the splitting of the charge density wave amplitude mode is observed. This result can be considered as a second hint of the occurrence of a dimerization in 1*T*-TaSe<sub>2</sub>.

To summarize, by means of temperature-dependent TR-ARPES measurements on 1*T*-TaSe<sub>2</sub>, we found that, by lowering the sample temperature from 300 K to 85 K, a variation of the spectral weights and a phonon splitting of the CDW amplitude mode occur. By DFT calculations and by invoking a one-dimensional harmonic lattice model, we provided evidence that both experimental observations can be explained in terms of a dimerization. Additionally, one can conclude that, within the commensurate CDW phase, a further unexpected [179] structural transition should occur.

#### 4.2.5 DFT calculations with Quantum Espresso

DFT calculations were performed with the Quantum Espresso package [180, 181]. Exchange-correlation was considered using the Perdew-Burke-Ernzerhof functional revised for solids (PBEsol). Van der Waals interaction was included using the semiempirical Grimme’s DFT-D2 correction [182]. Since the large number of atoms per CCDW unit cell (39 for the 1L case, 78 for the 2L case) implies a considerable computational power (and time), the calculations presented here have been performed with minimal convergence thresholds and should be considered as preliminary and indicative results. For both 1L and 2L cases the experimental lattice parameter and atomic positions from Ref. [183] were used:  $a = 12.54 \text{ \AA}$ ,  $c = 6.27 \text{ \AA}$  (1L)/ $12.54 \text{ \AA}$  (2L), space group P-3 (no. 147). The atomic positions within the fixed cells were then allowed to relax until residual forces were below  $1e^{-3}$

Ry/Bohr, with self-consistency convergence threshold of  $10e^{-5}$  Ry and  $2 \times 2 \times 4$   $k$ -point mesh. Notice that the use of space group P-3 implies an AA stacking for the 2L case. Fig. 4.15(a) reports the calculated  $k$ -projected DOS at the  $\Gamma$  point of the BZ.

### 4.3 Conclusions

In this Chapter, the results of our investigation of electron and phonon dynamics in 1T-TaSe<sub>2</sub> by TR-ARPES and TRR techniques were presented. Our measurements showed that both the CDW and the lattice degrees of freedom contribute to the stabilization of the Mott phase in 1T-TaSe<sub>2</sub>, shedding light on the interplay between these coexisting phases. Furthermore, temperature-dependent TR-ARPES measurements on this material provided evidence for a dimerization process in this material at low temperature. However, further proofs of this additional structural transition are required. For this purpose, in order to investigate 1T-TaSe<sub>2</sub> crystal lattice, X-ray diffraction measurements as a function of temperature should be performed. Finally, the  $k_z$  dispersion of the electronic states also needs to be explored by photon-energy dependent ARPES measurements.

## Conclusions and perspectives

Two-dimensional (2D) materials are at the center of a deep research due to their unique properties and their potential for disclosing fascinating new phenomena. Meanwhile, they allow the study of quantum phase transitions as well as new phases of matter. In this scenario, this thesis has presented a study of two notable two-dimensional layered materials, i.e. black phosphorus (BP) and the tantalum-based transition metal dichalcogenide (TMD)  $1T$ -TaSe<sub>2</sub>, performed using two ultrafast spectroscopy techniques, TR-ARPES and TRR.

BP is a layered semiconductor with intriguing physical properties such as high carrier mobility, large optical anisotropies and high strain limit. More interestingly, it exhibits a bandgap that can be widely tuned by changing the number of layers or by applying an external field. In this work, we investigate BP by TR-ARPES with 6 eV probe photons both in its pristine condition and in the presence of “giant” Stark effect, chemically induced by Cs surface doping. As concerning pristine BP, the photo-induced electronic dynamics allows to deduce the occurrence of a photo-induced bandgap renormalization (BGR) which comes with a concomitant VB flattening, due to Pauli blocking. Under Cs deposition, the observed VB broadening is found to be caused by photo-carriers ambipolar drift-diffusion. A surface photovoltage (SPV) counterbalancing the Cs-induced band bending is generated by pump irradiation. This effect has been used to infer that the crossing of VB and CB with the largest Cs dose can be interpreted as the overlap of bulk VB and surface CB, measured thanks to the bulk sensitivity of our ARPES system. We conclude that band inversion in Cs-doped bulk BP should be stated carefully: a real band crossing can be seen only in monolayer or few-layer ( $\leq 4$  layers) BP, where bulk contributions are not present. For this reason, it may be interesting to investigate monolayer or few-layer BP by TR-ARPES. Furthermore, the future plan is to build a TR-ARPES setup with tunable pump photon energy in order to resonantly pump BP. The complex photo-induced band dynamics disclosed in BP by our time-resolved study might be exploited for future opto-electronic applications of this material. Moreover, as bandgap tunability by alkali atoms deposition has also been observed in other 2D specimens as TMDs, our conclusions can be pertinent to a larger class of layered materials. Two-dimensional materials with buckled-layer structure are considered to be ideal candidates for innovative opto-electronics devices due to their anisotropic response to external stimuli and wide bandgap tunability with the number of layers. An in-plane puckered structure similar to the one of BP has been recently observed in the noble transition metal dichalcogenide PdSe<sub>2</sub>, whose physical properties could pave the way for new studies and applications.

The second material of our interest is the transition metal dichalcogenide  $1T$ -TaSe<sub>2</sub>. We used complementary TR-ARPES and TRR measurements to investigate the in-

terplay between the metal-insulator transition (MIT) and the charge density wave (CDW) phase in  $1T$ -TaSe<sub>2</sub>. As we have seen, a CDW is a periodic modulation of the electron density associated with a periodic distortion of the crystal lattice. In  $1T$ -TaSe<sub>2</sub>, an incommensurate to commensurate CDW transition occurs at 473 K. The commensurate CDW supercell experiences a  $\sqrt{13}\times\sqrt{13}$  reconstruction with a rotation of  $\sim 13^\circ$  with respect to the original lattice vectors, thus forming the “so-called” star-of-David configuration. By further lowering the temperature of the sample, a Mott metal-insulator transition (MIT) occurs and the opening of a gap of about 250 meV is observed correspondingly: ARPES measurements at 40 K show that all bands close to Fermi level  $E_F$  downshift in energy because of the Mott gap  $\Delta_{Mott}$  extending across the entire BZ. Even though surface-sensitive ARPES measurements give evidence for an insulating behaviour, bulk resistivity measurements as a function of the temperature prove a metallic behaviour of  $1T$ -TaSe<sub>2</sub>, suggesting the occurrence of a MIT only at the surface. TR-ARPES data show that the binding energy of the VB edge, associated to  $\Delta_{Mott}$ , is directly modulated by the CDW amplitude mode, related to the in-plane breathing mode of the stars-of-David. This result confirms the scenario in which the CDW is a precursor of the Mott phase because its amplitude controls the electron hopping between the adjacent stars-of-David. Therefore, the modulation of  $\Delta_{Mott}$  magnitude reflects the coherent oscillations of the CDW amplitude mode. Conversely, TRR signal gives evidence for multiple frequencies, related to phonons of the superlattice, including the CDW amplitude mode. As both TR-ARPES and TRR use comparable pump pulses, multiple modes are also triggered in TR-ARPES. However, the VB does not appear to be modulated by other frequencies. We conclude that the Mott phase is selectively linked to the CDW amplitude mode. TRR and Raman spectroscopy measurements in a wide temperature range (295 to 478 K) allowed us to deduce that the CDW amplitude mode can be suppressed by photo-excitation, although the CDW phase remains stable up  $T_{CDW}$ . Finally, temperature-dependent TR-ARPES measurements are presented. By lowering the sample temperature from 300 K to 85 K, a variation of the spectral weights and a phonon splitting of the CDW amplitude mode are observed. By comparing the experimental data to theoretical results obtained by DFT calculations and employing a simplified one-dimensional harmonic lattice model, we speculate that at low temperature a dimerization in  $1T$ -TaSe<sub>2</sub> takes place. However, a further proof of this additional structural transition, never seen before, should be obtained for instance by investigating the  $1T$ -TaSe<sub>2</sub> crystal lattice with X-ray diffraction measurements. Lastly, the exploration of the  $k_z$  dispersion by photon-energy dependent ARPES measurements is also required in order to achieve a more complete knowledge of the electronic band structure of  $1T$ -TaSe<sub>2</sub>.

Recent studies on transition metal dichalcogenides suggest that Mott physics and

CDW phase transitions can play a significant role also in superconducting systems, enriching our interest in this class of materials. The simultaneous occurrence of both the Mott-state CCDW phase and superconductivity in  $1T$ -TaS<sub>2</sub> [184] provides opportunities to investigate these collective states of matter in relation to each other. Therefore, the relationship between CDWs and superconductivity and forms of electronic and lattice order needs to be deeper investigated.



# Bibliography

- [1] Hamoon Hedayat, Arianna Ceraso, Giancarlo Soavi, Shahab Akhavan, Alison Cadore, Claudia Dallera, Giulio Cerullo, Andrea C Ferrari, and Ettore Carpene. Non-equilibrium band broadening, gap renormalization and band inversion in black phosphorus. *2D Materials*, 8(2):025020, 2021.
- [2] Andrea Damascelli. Probing the electronic structure of complex systems by arpes. *Physica Scripta*, 2004(T109):61, 2004.
- [3] M P I Seah and WA Dench. Quantitative electron spectroscopy of surfaces: A standard data base for electron inelastic mean free paths in solids. *Surface and interface analysis*, 1(1):2–11, 1979.
- [4] Ettore Carpene, Eduardo Mancini, Claudia Dallera, G Ghiringhelli, Cristian Manzoni, G Cerullo, and Sandro De Silvestri. A versatile apparatus for time-resolved photoemission spectroscopy via femtosecond pump-probe experiments. *Review of Scientific Instruments*, 80(5):055101, 2009.
- [5] A Morita. Semiconducting black phosphorus. *Applied Physics A*, 39(4):227–242, 1986.
- [6] CJ Sayers, Hamoon Hedayat, Arianna Ceraso, Flavien Museur, Mattia Cattelan, LS Hart, LS Farrar, Stefano Dal Conte, Giulio Cerullo, Claudia Dallera, et al. Coherent phonons and the interplay between charge density wave and mott phases in 1 t- ta se 2. *Physical Review B*, 102(16):161105, 2020.
- [7] Hui Fang, Steven Chuang, Ting Chia Chang, Kuniharu Takei, Toshitake Takahashi, and Ali Javey. High-performance single layered wse2 p-fets with chemically doped contacts. *Nano letters*, 12(7):3788–3792, 2012.
- [8] Andrea Splendiani, Liang Sun, Yuanbo Zhang, Tianshu Li, Jonghwan Kim, Chi-Yung Chim, Giulia Galli, and Feng Wang. Emerging photoluminescence in monolayer mos2. *Nano letters*, 10(4):1271–1275, 2010.

- [9] Han Liu, Adam T Neal, and Peide D Ye. Channel length scaling of mos2 mosfets. *ACS nano*, 6(10):8563–8569, 2012.
- [10] Xi Ling, Han Wang, Shengxi Huang, Fengnian Xia, and Mildred S Dresselhaus. The renaissance of black phosphorus. *Proceedings of the National Academy of Sciences*, 112(15):4523–4530, 2015.
- [11] Hamoon Hedayat, Davide Bugini, Hemian Yi, Chaoyu Chen, Xingjiang Zhou, Giulio Cerullo, Claudia Dallera, and Ettore Carpene. Surface state dynamics of topological insulators investigated by femtosecond time-and angle-resolved photoemission spectroscopy. *Applied Sciences*, 8(5):694, 2018.
- [12] C-K Sun, F Vallée, L Acioli, EP Ippen, and JG Fujimoto. Femtosecond investigation of electron thermalization in gold. *Physical Review B*, 48(16):12365, 1993.
- [13] C Gadermaier, AS Alexandrov, VV Kabanov, P Kusar, T Mertelj, X Yao, Cristian Manzoni, Daniele Brida, G Cerullo, and D Mihailovic. Electron-phonon coupling in high-temperature cuprate superconductors determined from electron relaxation rates. *Physical review letters*, 105(25):257001, 2010.
- [14] Roman Yusupov, Tomaz Mertelj, Viktor V Kabanov, Serguei Brazovskii, Primož Kusar, Jiun-Haw Chu, Ian R Fisher, and Dragan Mihailovic. Coherent dynamics of macroscopic electronic order through a symmetry breaking transition. *Nature Physics*, 6(9):681–684, 2010.
- [15] Jimin Kim, Seung Su Baik, Sae Hee Ryu, Yeongsup Sohn, Soohyung Park, Byeong-Gyu Park, Jonathan Denlinger, Yeonjin Yi, Hyoung Joon Choi, and Keun Su Kim. Observation of tunable band gap and anisotropic dirac semimetal state in black phosphorus. *Science*, 349(6249):723–726, 2015.
- [16] Sun-Woo Kim, Hyun Jung, Hyun-Jung Kim, Jin-Ho Choi, Su-Huai Wei, and Jun-Hyung Cho. Microscopic mechanism of the tunable band gap in potassium-doped few-layer black phosphorus. *Physical Review B*, 96(7):075416, 2017.
- [17] Neil W Ashcroft, N David Mermin, et al. *Solid state physics*, 1976.
- [18] G Grosso. *Pastori-parravicini 1999 solid state physics*.
- [19] Fengnian Xia, Han Wang, and Yichen Jia. Rediscovering black phosphorus as an anisotropic layered material for optoelectronics and electronics. *Nature communications*, 5(1):1–6, 2014.

- [20] Tu Hong, Bhim Chamlagain, Tianjiao Wang, Hsun-Jen Chuang, Zhixian Zhou, and Ya-Qiong Xu. Anisotropic photocurrent response at black phosphorus–mos 2 p–n heterojunctions. *Nanoscale*, 7(44):18537–18541, 2015.
- [21] Pengfei Chen, Neng Li, Xingzhu Chen, Wee-Jun Ong, and Xiujian Zhao. The rising star of 2d black phosphorus beyond graphene: synthesis, properties and electronic applications. *2D Materials*, 5(1):014002, 2017.
- [22] Zhesheng Chen, Jingwei Dong, Evangelos Papalazarou, Marino Marsi, Christine Giorgetti, Zailan Zhang, Bingbing Tian, Jean-Pascal Rueff, Amina Taleb-Ibrahimi, and Luca Perfetti. Band gap renormalization, carrier multiplication, and stark broadening in photoexcited black phosphorus. *Nano letters*, 19(1):488–493, 2018.
- [23] S Roth, A Crepaldi, M Puppini, G Gatti, D Bugini, I Grimaldi, TR Barrilot, CA Arrell, F Frassetto, L Poletto, et al. Photocarrier-induced band-gap renormalization and ultrafast charge dynamics in black phosphorus. *2D Materials*, 6(3):031001, 2019.
- [24] Elias Burstein. Anomalous optical absorption limit in insb. *Physical review*, 93(3):632, 1954.
- [25] Moss TS. The interpretation of the properties of indium antimonide. 1954.
- [26] Robert N Zitter. Saturated optical absorption through band filling in semiconductors. *Applied Physics Letters*, 14(2):73–74, 1969.
- [27] W Ebeling, D Blaschke, R Redmer, Heidi Reinholz, and G Röpke. The influence of pauli blocking effects on the properties of dense hydrogen. *Journal of Physics A: Mathematical and Theoretical*, 42(21):214033, 2009.
- [28] Yuankun Zhu, Rueben J Mendelsberg, Jiaqi Zhu, Jiecai Han, and André Anders. Dopant-induced band filling and bandgap renormalization in cdo: In films. *Journal of Physics D: Applied Physics*, 46(19):195102, 2013.
- [29] MK Hudait, P Modak, and SB Krupanidhi. Si incorporation and burstein–moss shift in n-type gaas. *Materials Science and Engineering: B*, 60(1):1–11, 1999.
- [30] B Ullrich, H Xi, and JS Wang. Photoinduced band filling in strongly confined colloidal pbs quantum dots. *Journal of Applied Physics*, 115(23):233503, 2014.
- [31] Michael Shur. Physics of semiconductor devices, prentice hall. *Inc., Englewood Cliffs, New Jersey*, page 680, 1990.

- [32] Ss Schmitt-Rink, DS Chemla, and DAB Miller. Linear and nonlinear optical properties of semiconductor quantum wells. *Advances in Physics*, 38(2):89–188, 1989.
- [33] Roberto Cingolani and Klaus Ploog. Frequency and density dependent radiative recombination processes in iii–v semiconductor quantum wells and superlattices. *Advances in Physics*, 40(5):535–623, 1991.
- [34] W Mönch. Work function and band bending at semiconductor surfaces. In *Chemistry and Physics of Solid Surfaces V*, pages 501–534. Springer, 1984.
- [35] SM Sze and K Ng. K., kk ng. *Physics of Semiconductor Devices, in: Phys. Semicond. Devices, 3rd ed., Wiley, Hoboken, New Jersey*, pages 416–475, 2007.
- [36] Hans Lüth. *Solid surfaces, interfaces and thin films*, volume 4. Springer, 2001.
- [37] Walter H Brattain and John Bardeen. Surface properties of germanium. *The Bell System Technical Journal*, 32(1):1–41, 1953.
- [38] CGBt Garrett and W He Brattain. Physical theory of semiconductor surfaces. *Physical Review*, 99(2):376, 1955.
- [39] EO Johnson. Large-signal surface photovoltage studies with germanium. *Physical Review*, 111(1):153, 1958.
- [40] Leeor Kronik and Yoram Shapira. Surface photovoltage phenomena: theory, experiment, and applications. *Surface science reports*, 37(1-5):1–206, 1999.
- [41] David Bröcker, Tatjana Giebel, and Wolf Widdra. Charge carrier dynamics at the sio<sub>2</sub>/si (1 0 0) surface: a time-resolved photoemission study with combined laser and synchrotron radiation. *Chemical physics*, 299(2-3):247–251, 2004.
- [42] E Papalazarou, L Khalil, M Caputo, L Perfetti, N Nilforoushan, H Deng, Z Chen, S Zhao, A Taleb-Ibrahimi, M Konczykowski, et al. Unraveling the dirac fermion dynamics of the bulk-insulating topological system bi<sub>2</sub>te<sub>3</sub>. *Physical Review Materials*, 2(10):104202, 2018.
- [43] Ben F Spencer, Darren M Graham, Samantha JO Hardman, Elaine A Seddon, Matthew J Cliffe, Karen L Syres, Andrew G Thomas, Stuart K Stubbs, Fausto Sirotti, Mathieu G Silly, et al. Time-resolved surface photovoltage measurements at n-type photovoltaic surfaces: Si (111) and zno (10 1 0). *Physical Review B*, 88(19):195301, 2013.

- [44] Shin-ichiro Tanaka. Utility and constraint on the use of pump-probe photoelectron spectroscopy for detecting time-resolved surface photovoltage. *Journal of Electron Spectroscopy and Related Phenomena*, 185(5-7):152–158, 2012.
- [45] S-L Yang, Jonathan A Sobota, Patrick S Kirchmann, and Z-X Shen. Electron propagation from a photo-excited surface: implications for time-resolved photoemission. *Applied Physics A*, 116(1):85–90, 2014.
- [46] RE Peierls. Quantum theory of solids—oxford up. *London, England*, page 108, 1955.
- [47] MD Johannes and II Mazin. Fermi surface nesting and the origin of charge density waves in metals. *Physical Review B*, 77(16):165135, 2008.
- [48] Lev Petrovich Gor’kov and George Grüner. *Charge density waves in solids*. Elsevier, 2012.
- [49] G Grüner. The dynamics of spin-density waves. *Reviews of modern physics*, 66(1):1, 1994.
- [50] George Gruner. *Density waves in solids*. CRC press, 2018.
- [51] R Samnakay, D Wickramaratne, TR Pope, RK Lake, TT Salguero, and AA Balandin. Zone-folded phonons and the commensurate–incommensurate charge-density-wave transition in 1 t-tase2 thin films. *Nano letters*, 15(5):2965–2973, 2015.
- [52] W Kohn. Image of the fermi surface in the vibration spectrum of a metal. *Physical Review Letters*, 2(9):393, 1959.
- [53] R Ho Friend and D Jerome. Periodic lattice distortions and charge density waves in one-and two-dimensional metals. *Journal of Physics C: Solid State Physics*, 12(8):1441, 1979.
- [54] Xuetao Zhu, Jiandong Guo, Jiandi Zhang, and EW Plummer. Misconceptions associated with the origin of charge density waves. *Advances in Physics: X*, 2(3):622–640, 2017.
- [55] J Hugo Dil. Spin-and angle-resolved photoemission on topological materials. *Electronic Structure*, 1(2):023001, 2019.
- [56] Taichi Okuda and Akio Kimura. Spin-and angle-resolved photoemission of strongly spin–orbit coupled systems. *Journal of the Physical Society of Japan*, 82(2):021002, 2013.

- [57] Eli Rotenberg and Aaron Bostwick. microarpes and nanoarpes at diffraction-limited light sources: opportunities and performance gains. *Journal of synchrotron radiation*, 21(5):1048–1056, 2014.
- [58] Mattia Cattelan and Neil A Fox. A perspective on the application of spatially resolved arpes for 2d materials. *Nanomaterials*, 8(5):284, 2018.
- [59] VN Strocov, X Wang, M Shi, M Kobayashi, J Krempasky, C Hess, T Schmitt, and L Patthey. Soft-x-ray arpes facility at the adress beamline of the sls: Concepts, technical realisation and scientific applications. *Journal of synchrotron radiation*, 21(1):32–44, 2014.
- [60] Yasunori Senba, Hikaru Kishimoto, Yoko Takeo, Hirokatsu Yumoto, Takahisa Koyama, Hidekazu Mimura, and Haruhiko Ohashi. Stable sub-micrometre high-flux probe for soft x-ray arpes using a monolithic wolter mirror. *Journal of Synchrotron Radiation*, 27(5), 2020.
- [61] Fabio Boschini, H Hedayat, Claudia Dallera, P Farinello, C Manzoni, A Magrez, H Berger, G Cerullo, and Ettore Carpene. An innovative yb-based ultrafast deep ultraviolet source for time-resolved photoemission experiments. *Review of Scientific Instruments*, 85(12):123903, 2014.
- [62] Christopher L Smallwood, Robert A Kaindl, and Alessandra Lanzara. Ultrafast angle-resolved photoemission spectroscopy of quantum materials. *EPL (Europhysics Letters)*, 115(2):27001, 2016.
- [63] Patrick S Kirchmann, Laurenz Rettig, Dhananjay Nandi, Uwe Lipowski, Martin Wolf, and Uwe Bovensiepen. A time-of-flight spectrometer for angle-resolved detection of low energy electrons in two dimensions. *Applied Physics A*, 91(2):211–217, 2008.
- [64] Y Saitoh, H Kimura, Y Suzuki, T Nakatani, T Matsushita, T Muro, T Miyahara, M Fujisawa, K Soda, S Ueda, et al. Performance of a very high resolution soft x-ray beamline BL25SU with a twin-helical undulator at spring-8. *Review of Scientific Instruments*, 71(9):3254–3259, 2000.
- [65] M Hoesch, TK Kim, P Dudin, H Wang, S Scott, P Harris, S Patel, M Matthews, D Hawkins, SG Alcock, et al. A facility for the analysis of the electronic structures of solids and their surfaces by synchrotron radiation photoelectron spectroscopy. *Review of Scientific Instruments*, 88(1):013106, 2017.
- [66] Yngve Cerenius, Franz Hennies, and Pedro Fernandes Tavares. Status of the MAX IV laboratory. *Synchrotron Radiation News*, 29(1):34–38, 2016.

- [67] R Reininger, SL Hulbert, PD Johnson, JT Sadowski, DE Starr, O Chubar, T Valla, and E Vescovo. The electron spectro-microscopy beamline at national synchrotron light source II: A wide photon energy range, micro-focusing beamline for photoelectron spectro-microscopies. *Review of Scientific Instruments*, 83(2):023102, 2012.
- [68] JD Koralek, JF Douglas, NC Plumb, JD Griffith, ST Cundiff, HC Kapteyn, MM Murnane, and DS Dessau. Experimental setup for low-energy laser-based angle resolved photoemission spectroscopy. *Review of Scientific Instruments*, 78(5):053905, 2007.
- [69] S Mathias, L Miaja-Avila, MM Murnane, H Kapteyn, M Aeschlimann, and M Bauer. Angle-resolved photoemission spectroscopy with a femtosecond high harmonic light source using a two-dimensional imaging electron analyzer. *Review of Scientific Instruments*, 78(8):083105, 2007.
- [70] Guodong Liu, Guiling Wang, Yong Zhu, Hongbo Zhang, Guochun Zhang, Xiaoyang Wang, Yong Zhou, Wentao Zhang, Haiyun Liu, Lin Zhao, et al. Development of a vacuum ultraviolet laser-based angle-resolved photoemission system with a superhigh energy resolution better than 1 meV. *Review of Scientific Instruments*, 79(2):023105, 2008.
- [71] T Kiss, T Shimojima, K Ishizaka, A Chainani, T Togashi, T Kanai, X-Y Wang, C-T Chen, S Watanabe, and S Shin. A versatile system for ultrahigh resolution, low temperature, and polarization dependent laser-angle-resolved photoemission spectroscopy. *Review of Scientific Instruments*, 79(2):023106, 2008.
- [72] Paul Van der Heide. X-ray photoelectron spectroscopy. *An Introduction to Principles and Practices*, 2011.
- [73] R Leckey. Ultraviolet photoelectron spectroscopy of solids. In *Surface Analysis Methods in Materials Science*, pages 337–345. Springer, 2003.
- [74] Andrea Damascelli, Zahid Hussain, and Zhi-Xun Shen. Angle-resolved photoemission studies of the cuprate superconductors. *Reviews of modern physics*, 75(2):473, 2003.
- [75] AA Kordyuk. Arpes experiment in fermiology of quasi-2d metals. *Low Temperature Physics*, 40(4):286–296, 2014.
- [76] DN Basov, MM Fogler, A Lanzara, Feng Wang, Yuanbo Zhang, et al. Colloquium: graphene spectroscopy. *Reviews of Modern Physics*, 86(3):959, 2014.

- [77] GD Mahan. Theory of photoemission in simple metals. *Physical Review B*, 2(11):4334, 1970.
- [78] Marcus Ossiander, Johann Riemensberger, S Neppl, M Mittermair, Martin Schäffer, A Duensing, MS Wagner, R Heider, M Wurzer, M Gerl, et al. Absolute timing of the photoelectric effect. *Nature*, 561(7723):374–377, 2018.
- [79] Carl Neil Berglund and William Edward Spicer. Photoemission studies of copper and silver: theory. *Physical Review*, 136(4A):A1030, 1964.
- [80] Edmund C Stoner. Xxiv. the thermodynamic functions for a fermi-dirac gas. *The London, Edinburgh, and Dublin Philosophical Magazine and Journal of Science*, 28(188):257–286, 1939.
- [81] S Parham, H Li, TJ Nummy, JA Waugh, XQ Zhou, J Griffith, J Schneeloch, RD Zhong, GD Gu, and DS Dessau. Ultrafast gap dynamics and electronic interactions in a photoexcited cuprate superconductor. *Physical Review X*, 7(4):041013, 2017.
- [82] Christopher L Smallwood, James P Hinton, Christopher Jozwiak, Wentao Zhang, Jake D Koralek, Hiroshi Eisaki, Dung-Hai Lee, Joseph Orenstein, and Alessandra Lanzara. Tracking cooper pairs in a cuprate superconductor by ultrafast angle-resolved photoemission. *Science*, 336(6085):1137–1139, 2012.
- [83] Jeff Graf, Chris Jozwiak, Chris L Smallwood, H Eisaki, Robert A Kaindl, Dung-Hai Lee, and Alessandra Lanzara. Nodal quasiparticle meltdown in ultrahigh-resolution pump–probe angle-resolved photoemission. *Nature Physics*, 7(10):805–809, 2011.
- [84] S Hellmann, T Rohwer, M Kalläne, K Hanff, C Sohr, A Stange, A Carr, MM Murnane, HC Kapteyn, L Kipp, et al. Time-domain classification of charge-density-wave insulators. *Nature communications*, 3(1):1–8, 2012.
- [85] F Schmitt, Patrick S Kirchmann, Uwe Bovensiepen, RG Moore, JH Chu, DH Lu, L Rettig, M Wolf, IR Fisher, and ZX Shen. Ultrafast electron dynamics in the charge density wave material tbte3. *New Journal of Physics*, 13(6):063022, 2011.
- [86] Madhab Neupane, Su-Yang Xu, Yukiaki Ishida, Shuang Jia, Benjamin M Fregoso, Chang Liu, Ilya Belopolski, Guang Bian, Nasser Alidoust, Tomasz Durakiewicz, et al. Gigantic surface lifetime of an intrinsic topological insulator. *Physical review letters*, 115(11):116801, 2015.



- [87] M Hajlaoui, E Papalazarou, J Mauchain, Z Jiang, I Miotkowski, YP Chen, A Taleb-Ibrahimi, L Perfetti, and M Marsi. Time resolved ultrafast arpes for the study of topological insulators: The case of  $\text{Bi}_2\text{Te}_3$ . *The European Physical Journal Special Topics*, 222(5):1271–1275, 2013.
- [88] Ro-Ya Liu, Yu Ogawa, Peng Chen, Kenichi Ozawa, Takeshi Suzuki, Masaru Okada, Takashi Someya, Yukiaki Ishida, Kozo Okazaki, Shik Shin, et al. Femtosecond to picosecond transient effects in  $\text{Bi}_2\text{Te}_3$  observed by pump-probe angle-resolved photoemission spectroscopy. *Scientific reports*, 7(1):1–7, 2017.
- [89] PK Das, D Di Sante, F Cilento, C Bigi, D Kopic, D Soranzio, A Sterzi, JA Krieger, I Vobornik, J Fujii, et al. Electronic properties of candidate type-ii weyl semimetal  $\text{WTe}_2$ . a review perspective. *Electronic Structure*, 1(1):014003, 2019.
- [90] Alexandre Gauthier, Jonathan A Sobota, Nicolas Gauthier, Ke-Jun Xu, Heike Pfau, Costel R Rotundu, Zhi-Xun Shen, and Patrick S Kirchmann. Tuning time and energy resolution in time-resolved photoemission spectroscopy with nonlinear crystals. *Journal of Applied Physics*, 128(9):093101, 2020.
- [91] Christopher L Smallwood, Christopher Jozwiak, Wentao Zhang, and Alessandra Lanzara. An ultrafast angle-resolved photoemission apparatus for measuring complex materials. *Review of Scientific Instruments*, 83(12):123904, 2012.
- [92] Jérôme Faure, J Mauchain, E Papalazarou, W Yan, J Pinon, M Marsi, and Luca Perfetti. Full characterization and optimization of a femtosecond ultraviolet laser source for time and angle-resolved photoemission on solid surfaces. *Review of Scientific Instruments*, 83(4):043109, 2012.
- [93] S Passlack, S Mathias, O Andreyev, D Mittnacht, M Aeschlimann, and M Bauer. Space charge effects in photoemission with a low repetition, high intensity femtosecond laser source. *Journal of applied physics*, 100(2):024912, 2006.
- [94] Christian Tusche, Ying-Jiun Chen, Claus M Schneider, and Jürgen Kirschner. Imaging properties of hemispherical electrostatic energy analyzers for high resolution momentum microscopy. *Ultramicroscopy*, 206:112815, 2019.
- [95] Jonathan A Sobota, Shuolong Yang, James G Analytis, YL Chen, Ian R Fisher, Patrick S Kirchmann, and Z-X Shen. Ultrafast optical excitation of

- a persistent surface-state population in the topological insulator  $\text{Bi}_2\text{Se}_3$ . *Physical review letters*, 108(11):117403, 2012.
- [96] Yan Zhang, Chenlu Wang, Li Yu, Guodong Liu, Aiji Liang, Jianwei Huang, Simin Nie, Xuan Sun, Yuxiao Zhang, Bing Shen, et al. Electronic evidence of temperature-induced Lifshitz transition and topological nature in  $\text{ZrTe}_5$ . *Nature communications*, 8(1):1–9, 2017.
- [97] Carsten Winterfeldt, Christian Spielmann, and Gustav Gerber. Colloquium: Optimal control of high-harmonic generation. *Reviews of Modern Physics*, 80(1):117, 2008.
- [98] GL Dakovski, Y Li, T Durakiewicz, and G Rodriguez. Tunable ultrafast extreme ultraviolet source for time- and angle-resolved photoemission spectroscopy. *Review of Scientific Instruments*, 81(7):073108, 2010.
- [99] Philippe Wernet, Jérôme Gaudin, Kai Godehusen, Olaf Schwarzkopf, and Wolfgang Eberhardt. Femtosecond time-resolved photoelectron spectroscopy with a vacuum-ultraviolet photon source based on laser high-order harmonic generation. *Review of Scientific Instruments*, 82(6):063114, 2011.
- [100] Simone Peli, Denny Puntel, Damir Kopic, Benjamin Sockol, Fulvio Parmigiani, and Federico Cilento. High repetition rate time-resolved VUV ARPES at 10.8 eV photon energy. *arXiv preprint arXiv:1911.05590*, 2019.
- [101] Magnus H Berntsen, Olof Götberg, and Oscar Tjernberg. An experimental setup for high resolution 10.5 eV laser-based angle-resolved photoelectron spectroscopy using a time-of-flight electron analyzer. *Review of Scientific Instruments*, 82(9):095113, 2011.
- [102] Yu He, Inna M Vishik, Ming Yi, Shuolong Yang, Zhongkai Liu, James J Lee, Sudi Chen, Slavko N Rebec, Dominik Leuenberger, Alfred Zong, et al. Invited article: High resolution angle resolved photoemission with tabletop 11 eV laser. *Review of Scientific Instruments*, 87(1):011301, 2016.
- [103] Alfred Zong, Anshul Kogar, Ya-Qing Bie, Timm Rohwer, Changmin Lee, Edoardo Baldini, Emre Ergeçen, Mehmet B Yilmaz, Byron Freelon, Edbert J Sie, et al. Disentangling amplitude and phase dynamics of a charge density wave in a photo-induced phase transition. *arXiv preprint arXiv:1806.02766*, 2018.
- [104] Cristian Manzoni, Dario Polli, and Giulio Cerullo. Two-color pump-probe system broadly tunable over the visible and the near infrared with sub-30 fs temporal resolution. *Review of scientific instruments*, 77(2):023103, 2006.

- [105] Hamoon Hedayat, Charles J Sayers, Arianna Ceraso, Jasper van Wezel, Stephen R Clark, Claudia Dallera, Giulio Cerullo, Enrico Da Como, and Ettore Carpene. Investigation of the non-equilibrium state of strongly correlated materials by complementary ultrafast spectroscopy techniques. *New Journal of Physics*, 23(3):033025, 2021.
- [106] Ettore Carpene, H Hedayat, Fabio Boschini, and Claudia Dallera. Ultrafast demagnetization of metals: Collapsed exchange versus collective excitations. *Physical Review B*, 91(17):174414, 2015.
- [107] HJ Zeiger, J Vidal, TK Cheng, EP Ippen, G Dresselhaus, and MS Dresselhaus. Theory for displacive excitation of coherent phonons. *Physical Review B*, 45(2):768, 1992.
- [108] George Placzek. *The rayleigh and raman scattering*, volume 526. Lawrence Radiation Laboratory, 1959.
- [109] H Hirori, T Tachizaki, O Matsuda, and OB Wright. Electron dynamics in chromium probed with 20-fs optical pulses. *Physical Review B*, 68(11):113102, 2003.
- [110] Barbara Mansart, Davide Boschetto, A Savoia, F Rullier-Albenque, F Bouquet, E Papalazarou, A Forget, D Colson, Antoine Rousse, and M Marsi. Ultrafast transient response and electron-phonon coupling in the iron-pnictide superconductor  $\text{Ba}(\text{Fe}_{1-x}\text{Co}_x)_2\text{As}_2$ . *Physical Review B*, 82(2):024513, 2010.
- [111] Kostya S Novoselov, D Jiang, F Schedin, TJ Booth, VV Khotkevich, SV Morozov, and Andre K Geim. Two-dimensional atomic crystals. *Proceedings of the National Academy of Sciences*, 102(30):10451–10453, 2005.
- [112] Rafael Roldán, Luca Chirilli, Elsa Prada, Jose Angel Silva-Guillén, Pablo San-Jose, and Francisco Guinea. Theory of 2d crystals: graphene and beyond. *Chemical Society Reviews*, 46(15):4387–4399, 2017.
- [113] Han Liu, Adam T Neal, Zhen Zhu, Zhe Luo, Xianfan Xu, David Tománek, and Peide D Ye. Phosphorene: an unexplored 2d semiconductor with a high hole mobility. *ACS nano*, 8(4):4033–4041, 2014.
- [114] Jingsi Qiao, Xianghua Kong, Zhi-Xin Hu, Feng Yang, and Wei Ji. High-mobility transport anisotropy and linear dichroism in few-layer black phosphorus. *Nature communications*, 5(1):1–7, 2014.

- [115] Wei Xin, Hao Bo Jiang, Teng Qian Sun, Xiao Guang Gao, Shao Nan Chen, Bo Zhao, Jian Jun Yang, Zhi Bo Liu, Jian Guo Tian, and Chun Lei Guo. Optical anisotropy of black phosphorus by total internal reflection. *Nano Materials Science*, 1(4):304–309, 2019.
- [116] Qun Wei and Xihong Peng. Superior mechanical flexibility of phosphorene and few-layer black phosphorus. *Applied Physics Letters*, 104(25):251915, 2014.
- [117] Vy Tran, Ryan Soklaski, Yufeng Liang, and Li Yang. Layer-controlled band gap and anisotropic excitons in few-layer black phosphorus. *Physical Review B*, 89(23):235319, 2014.
- [118] ZJ Xiang, GJ Ye, C Shang, B Lei, NZ Wang, KS Yang, DY Liu, FB Meng, XG Luo, LJ Zou, et al. Pressure-induced electronic transition in black phosphorus. *Physical review letters*, 115(18):186403, 2015.
- [119] Yan Li, Shengxue Yang, and Jingbo Li. Modulation of the electronic properties of ultrathin black phosphorus by strain and electrical field. *The Journal of Physical Chemistry C*, 118(41):23970–23976, 2014.
- [120] Yanpeng Liu, Zhizhan Qiu, Alexandra Carvalho, Yang Bao, Hai Xu, Sherman JR Tan, Wei Liu, AH Castro Neto, Kian Ping Loh, and Jiong Lu. Gate-tunable giant stark effect in few-layer black phosphorus. *Nano letters*, 17(3):1970–1977, 2017.
- [121] N Ehlen, A Sanna, BV Senkovskiy, L Petaccia, AV Fedorov, G Profeta, and A Grüneis. Direct observation of a surface resonance state and surface band inversion control in black phosphorus. *Physical review B*, 97(4):045143, 2018.
- [122] KH Khoo, Steven G Louie, et al. Tuning the electronic properties of boron nitride nanotubes with transverse electric fields: A giant dc stark effect. *Physical Review B*, 69(20):201401, 2004.
- [123] Qihang Liu, Xiuwen Zhang, LB Abdalla, Adalberto Fazzio, and Alex Zunger. Switching a normal insulator into a topological insulator via electric field with application to phosphorene. *Nano letters*, 15(2):1222–1228, 2015.
- [124] AN Rudenko, Shengjun Yuan, and MI Katsnelson. Toward a realistic description of multilayer black phosphorus: From g w approximation to large-scale tight-binding simulations. *Physical Review B*, 92(8):085419, 2015.
- [125] Munisa Nurmamat, Yukiaki Ishida, Ryohei Yori, Kazuki Sumida, Siyuan Zhu, Masashi Nakatake, Yoshifumi Ueda, Masaki Taniguchi, Shik Shin,

- Yuichi Akahama, et al. Prolonged photo-carriers generated in a massive-and-anisotropic dirac material. *Scientific reports*, 8(1):1–7, 2018.
- [126] Xianchong Miao, Guowei Zhang, Fanjie Wang, Hugen Yan, and Minbiao Ji. Layer-dependent ultrafast carrier and coherent phonon dynamics in black phosphorus. *Nano letters*, 18(5):3053–3059, 2018.
- [127] Xiaomu Wang, Aaron M Jones, Kyle L Seyler, Vy Tran, Yichen Jia, Huan Zhao, Han Wang, Li Yang, Xiaodong Xu, and Fengnian Xia. Highly anisotropic and robust excitons in monolayer black phosphorus. *Nature nanotechnology*, 10(6):517–521, 2015.
- [128] Hongtao Yuan, Xiaoge Liu, Farzaneh Afshinmanesh, Wei Li, Gang Xu, Jie Sun, Biao Lian, Alberto G Curto, Guojun Ye, Yasuyuki Hikita, et al. Polarization-sensitive broadband photodetector using a black phosphorus vertical p–n junction. *Nature nanotechnology*, 10(8):707–713, 2015.
- [129] Ruixiang Fei, Alireza Faghaninia, Ryan Soklaski, Jia-An Yan, Cynthia Lo, and Li Yang. Enhanced thermoelectric efficiency via orthogonal electrical and thermal conductances in phosphorene. *Nano letters*, 14(11):6393–6399, 2014.
- [130] Claus F Klingshirn. *Semiconductor optics*. Springer Science & Business Media, 2012.
- [131] Nasser Peyghambarian, Stephan W Koch, and Andre Mysyrowicz. *Introduction to semiconductor optics*. Prentice-Hall, Inc., 1993.
- [132] TS Moss. The interpretation of the properties of indium antimonide. *Proceedings of the Physical Society. Section B*, 67(10):775, 1954.
- [133] Tony Low, AS Rodin, A Carvalho, Yongjin Jiang, Han Wang, Fengnian Xia, and AH Castro Neto. Tunable optical properties of multilayer black phosphorus thin films. *Physical Review B*, 90(7):075434, 2014.
- [134] Zhesheng Chen, Jingwei Dong, Christine Giorgetti, Evangelos Papalazarou, Marino Marsi, Zailan Zhang, Bingbing Tian, Qingwei Ma, Yingchun Cheng, Jean-Pascal Rueff, et al. Spectroscopy of buried states in black phosphorus with surface doping. *2D Materials*, 7(3):035027, 2020.
- [135] Martin V Allmen and Andreas Blatter. *Laser-beam interactions with materials: physical principles and applications*, volume 2. Springer Science & Business Media, 2013.

- [136] CC Stephenson, RL Potter, TG Maple, and JC Morrow. The thermodynamic properties of elementary phosphorus the heat capacities of two crystalline modifications of red phosphorus, of  $\alpha$  and  $\beta$  white phosphorus, and of black phosphorus from 15 to 300 k. *The Journal of Chemical Thermodynamics*, 1(1):59–76, 1969.
- [137] JF Schetzina and JP McKelvey. Ambipolar transport of electrons and holes in anisotropic crystals. *Physical Review B*, 2(6):1869, 1970.
- [138] Kostya S Novoselov, Andre K Geim, Sergei V Morozov, Dingde Jiang, Yan-shui Zhang, Sergey V Dubonos, Irina V Grigorieva, and Alexandr A Firsov. Electric field effect in atomically thin carbon films. *science*, 306(5696):666–669, 2004.
- [139] Li Song, Lijie Ci, Hao Lu, Pavel B Sorokin, Chuanhong Jin, Jie Ni, Alexander G Kvashnin, Dmitry G Kvashnin, Jun Lou, Boris I Yakobson, et al. Large scale growth and characterization of atomic hexagonal boron nitride layers. *Nano letters*, 10(8):3209–3215, 2010.
- [140] Kang Hyuck Lee, Hyeon-Jin Shin, Jinyeong Lee, In-yeal Lee, Gil-Ho Kim, Jae-Young Choi, and Sang-Woo Kim. Large-scale synthesis of high-quality hexagonal boron nitride nanosheets for large-area graphene electronics. *Nano letters*, 12(2):714–718, 2012.
- [141] Oriol Lopez-Sanchez, Dominik Lembke, Metin Kayci, Aleksandra Radenovic, and Andras Kis. Ultrasensitive photodetectors based on monolayer mos 2. *Nature nanotechnology*, 8(7):497–501, 2013.
- [142] Niraj K Nepal, Liping Yu, Qimin Yan, and Adrienn Ruzsinszky. First-principles study of mechanical and electronic properties of bent monolayer transition metal dichalcogenides. *Physical Review Materials*, 3(7):073601, 2019.
- [143] Sang A Han, Ravi Bhatia, and Sang-Woo Kim. Synthesis, properties and potential applications of two-dimensional transition metal dichalcogenides. *Nano Convergence*, 2(1):1–14, 2015.
- [144] Ibrahim Sarpkaya. Optical properties of semiconducting transition metal dichalcogenide materials. *Synthesis, Modelling and Characterization of 2D Materials and their Heterostructures*, page 57, 2020.
- [145] Manish Chhowalla and Hyeon Suk Shin. Goki eda, lain-jong li, kian ping loh, and hua zhang. *The chemistry of two-dimensional layered transition metal dichalcogenide nanosheets*, 5:263, 2013.

- [146] JI A Wilson and AD Yoffe. The transition metal dichalcogenides discussion and interpretation of the observed optical, electrical and structural properties. *Advances in Physics*, 18(73):193–335, 1969.
- [147] LF Mattheiss. Band structures of transition-metal-dichalcogenide layer compounds. *Physical Review B*, 8(8):3719, 1973.
- [148] Qing Hua Wang, Kouros Kalantar-Zadeh, Andras Kis, Jonathan N Coleman, and Michael S Strano. Electronics and optoelectronics of two-dimensional transition metal dichalcogenides. *Nature nanotechnology*, 7(11):699–712, 2012.
- [149] Lewis S Ramsdell. Studies on silicon carbide. *American Mineralogist: Journal of Earth and Planetary Materials*, 32(1-2):64–82, 1947.
- [150] H Katzke, P Tolédano, and W Depmeier. Phase transitions between polytypes and intralayer superstructures in transition metal dichalcogenides. *Physical Review B*, 69(13):134111, 2004.
- [151] JI A Wilson, FJ Di Salvo, and S Mahajan. Charge-density waves and superlattices in the metallic layered transition metal dichalcogenides. *Advances in Physics*, 24(2):117–201, 1975.
- [152] PM Williams, CB Scruby, WB Clark, and GS Parry. Charge density waves in the layered transition metal dichalcogenides. *Le Journal de Physique Colloques*, 37(C4):C4–139, 1976.
- [153] L Perfetti, A Georges, Serge Florens, S Biermann, S Mitrovic, H Berger, Y Tomm, H Höchst, and M Grioni. Spectroscopic signatures of a bandwidth-controlled mott transition at the surface of 1 t- t a s e 2. *Physical review letters*, 90(16):166401, 2003.
- [154] Stefano Colonna, Fabio Ronci, Antonio Cricenti, Luca Perfetti, Helmuth Berger, and Marco Grioni. Mott phase at the surface of 1 t- t a s e 2 observed by scanning tunneling microscopy. *Physical review letters*, 94(3):036405, 2005.
- [155] JA Wilson, FJ Di Salvo, and S Mahajan. Charge-density waves in metallic, layered, transition-metal dichalcogenides. *Physical review letters*, 32(16):882, 1974.
- [156] S Colonna, F Ronci, A Cricenti, L Perfetti, H Berger, and M Grioni. Scanning tunneling microscopy observation of a mott-insulator phase at the 1t-tase2 surface. *Japanese journal of applied physics*, 45(3S):1950, 2006.

- [157] Myung Hwan Whangbo and Enric Canadell. Analogies between the concepts of molecular chemistry and solid-state physics concerning structural instabilities. electronic origin of the structural modulations in layered transition metal dichalcogenides. *Journal of the American Chemical Society*, 114(24):9587–9600, 1992.
- [158] C Sohrt, A Stange, M Bauer, and K Rossnagel. How fast can a peierls–mott insulator be melted? *Faraday discussions*, 171:243–257, 2014.
- [159] F Boschini, EH da Silva Neto, E Razzoli, M Zonno, S Peli, RP Day, M Michiardi, M Schneider, B Zwartsenberg, P Nigge, et al. Collapse of superconductivity in cuprates via ultrafast quenching of phase coherence. *Nature materials*, 17(5):416–420, 2018.
- [160] Hamoon Hedayat, Charles J Sayers, Davide Bugini, Claudia Dallera, Daniel Wolverson, Tim Batten, Sara Karbassi, Sven Friedemann, Giulio Cerullo, Jasper van Wezel, et al. Excitonic and lattice contributions to the charge density wave in  $1t\text{-}t_2\text{-}e_2$  revealed by a phonon bottleneck. *Physical Review Research*, 1(2):023029, 2019.
- [161] Xun Shi, Wenjing You, Yingchao Zhang, Zhensheng Tao, Peter M Oppeneer, Xianxin Wu, Ronny Thomale, Kai Rossnagel, Michael Bauer, Henry Kapteyn, et al. Ultrafast electron calorimetry uncovers a new long-lived metastable state in  $1t\text{-}t_2\text{-}e_2$  mediated by mode-selective electron-phonon coupling. *Science advances*, 5(3):eaav4449, 2019.
- [162] S. E. Stoltz, H. I. Starnberg, and L. J. Holleboom. Rb intercalation of  $1t\text{-}t_2\text{-}e_2$  studied by photoelectron spectroscopy. *Phys. Rev. B*, 67:125107, Mar 2003.
- [163] R Ang, Y Miyata, E Ieki, Kosuke Nakayama, Takafumi Sato, Y Liu, WJ Lu, YP Sun, and Takashi Takahashi. Superconductivity and bandwidth-controlled mott metal-insulator transition in  $1t\text{-}t_2\text{-}e_2\text{-}x\text{-}se\text{-}x$ . *Physical Review B*, 88(11):115145, 2013.
- [164] Arlette S Ngankeu, Sanjoy K Mahatha, Kevin Guilloy, Marco Bianchi, Charlotte E Sanders, Kerstin Hanff, Kai Rossnagel, Jill A Miwa, Christina Breth Nielsen, Martin Bremholm, et al. Quasi-one-dimensional metallic band dispersion in the commensurate charge density wave of  $1t\text{-}t_2\text{-}e_2$ . *Physical Review B*, 96(19):195147, 2017.
- [165] F Levy and Y Froidevaux. Structural and electrical properties of layered transition metal selenides  $vxt_1\text{-}xse_2$  and  $taxt_1\text{-}xse_2$ . *Journal of Physics C: Solid State Physics*, 12(3):473, 1979.



- [166] FJ Di Salvo, RG Maines, JV Waszczak, and RE Schwall. Preparation and properties of 1t-tase2. *Solid State Communications*, 14(6):497–501, 1974.
- [167] M Bovet, D Popović, F Clerc, Christian Koitzsch, U Probst, E Bucher, H Berger, D Naumović, and Philipp Aebi. Pseudogapped fermi surfaces of 1 t- tas 2 and 1 t- tase 2: A charge density wave effect. *Physical Review B*, 69(12):125117, 2004.
- [168] F Clerc, M Bovet, H Berger, Laurent Despont, C Koitzsch, O Gallus, L Patthey, M Shi, J Krempasky, MG Garnier, et al. Spin–orbit splitting in the valence bands of 1t-tas2 and 1t-tase2. *Journal of Physics: Condensed Matter*, 16(18):3271, 2004.
- [169] Luca Perfetti, Panagiotis A Loukakos, Martin Lisowski, Uwe Bovensiepen, Martin Wolf, Helmuth Berger, Silke Biermann, and Antoine Georges. Femtosecond dynamics of electronic states in the mott insulator 1t-tas2 by time resolved photoelectron spectroscopy. *New Journal of Physics*, 10(5):053019, 2008.
- [170] Shaozheng Ji, Oscar Grånäs, Kai Rossnagel, and Jonas Weissenrieder. Transient three-dimensional structural dynamics in 1 t- tas e 2. *Physical Review B*, 101(9):094303, 2020.
- [171] Luca Perfetti, PA Loukakos, M Lisowski, U Bovensiepen, H Berger, S Biermann, PS Cornaglia, A Georges, and M Wolf. Time evolution of the electronic structure of 1 t- tas 2 through the insulator-metal transition. *Physical review letters*, 97(6):067402, 2006.
- [172] J Demsar, L Forró, H Berger, and D Mihailovic. Femtosecond snapshots of gap-forming charge-density-wave correlations in quasi-two-dimensional dichalcogenides 1 t- tas 2 and 2 h- tase 2. *Physical review B*, 66(4):041101, 2002.
- [173] P Fazekas and E Tosatti. Charge carrier localization in pure and doped 1t-tas2. *Physica B+ C*, 99(1-4):183–187, 1980.
- [174] Yi Chen, Wei Ruan, Meng Wu, Shujie Tang, Hyejin Ryu, Hsin-Zon Tsai, Ryan L Lee, Salman Kahn, Franklin Liou, Caihong Jia, et al. Strong correlations and orbital texture in single-layer 1t-tase2. *Nature Physics*, 16(2):218–224, 2020.
- [175] JE Smith Jr, JC Tsang, and MW Shafer. Raman spectra of several layer compounds with charge density waves. *Solid State Communications*, 19(4):283–286, 1976.

- [176] JC Tsang, JE Smith Jr, MW Shafer, and SF Meyer. Raman spectroscopy of the charge-density-wave state in  $1\text{-t-}2\text{-h-tas}$ . *Physical Review B*, 16(10):4239, 1977.
- [177] Sung-Hoon Lee, Jung Suk Goh, and Doohee Cho. Origin of the insulating phase and first-order metal-insulator transition in  $1\text{-t-}2\text{-tas}$ . *Physical review letters*, 122(10):106404, 2019.
- [178] Quirin Stahl, Maximilian Kusch, Florian Heinsch, Gaston Garbarino, Norman Kretzschmar, Kerstin Hanff, Kai Rosnagel, Jochen Geck, and Tobias Ritschel. Collapse of layer dimerization in the photo-induced hidden state of  $1\text{-t-}2\text{-tas}$ . *Nature communications*, 11(1):1–7, 2020.
- [179] Kai Sun, Shuaishuai Sun, Chunhui Zhu, Huanfang Tian, Huaixin Yang, and Jianqi Li. Hidden cdw states and insulator-to-metal transition after a pulsed femtosecond laser excitation in layered chalcogenide  $1\text{-t-}2\text{-xsex}$ . *Science advances*, 4(7):eaas9660, 2018.
- [180] Paolo Giannozzi, Stefano Baroni, Nicola Bonini, Matteo Calandra, Roberto Car, Carlo Cavazzoni, Davide Ceresoli, Guido L Chiarotti, Matteo Cococcioni, Ismaila Dabo, et al. Quantum espresso: a modular and open-source software project for quantum simulations of materials. *Journal of physics: Condensed matter*, 21(39):395502, 2009.
- [181] Paolo Giannozzi, Oliviero Andreussi, Thomas Brumme, Oana Bunau, M Buongiorno Nardelli, Matteo Calandra, Roberto Car, Carlo Cavazzoni, Davide Ceresoli, Matteo Cococcioni, et al. Advanced capabilities for materials modelling with quantum espresso. *Journal of physics: Condensed matter*, 29(46):465901, 2017.
- [182] Stefan Grimme, Jens Antony, Stephan Ehrlich, and Helge Krieg. A consistent and accurate ab initio parametrization of density functional dispersion correction (dft-d) for the 94 elements h-pu. *The Journal of chemical physics*, 132(15):154104, 2010.
- [183] R Brouwer and F Jellinek. The low-temperature superstructures of  $1\text{-t-}2\text{-ase}$  and  $2\text{-h-}2\text{-ase}$ . *Physica B+ C*, 99(1-4):51–55, 1980.
- [184] Balazs Sipos, Anna F Kusmartseva, Ana Akrap, Helmut Berger, Laszlo Forró, and Eduard Tutiš. From mott state to superconductivity in  $1\text{-t-}2\text{-tas}$ . *Nature materials*, 7(12):960–965, 2008.

## List of publications

1. H. Hedayat, A. Ceraso, G. Soavi, A. C. Ferrari, C. Dallera, G. Cerullo, E. Carpene, “Non-equilibrium Band Broadening, Gap Renormalization and Band Inversion in Black Phosphorus” *2D Materials* **8** (2021) 025020
2. C. J. Sayers, H. Hedayat, A. Ceraso, F. Museur, M. Cattelan, L. S. Hart, L. S. Farrar, S. Dal Conte, G. Cerullo, C. Dallera, E. Da Como, and E. Carpene, “Coherent phonons and the interplay between charge density wave and Mott phases in 1T-TaSe<sub>2</sub>”, *Physical Review B* **102**, 161105(R) (2021)
3. H. Hedayat, A. Ceraso, C. J. Sayers, S. Dal Conte, J. van Wezel, S. R. Clark, E. Da Como, G. Cerullo, C. Dallera, E. Carpene, “Combined ultrafast spectroscopy techniques discloses the microscopic electron lattice interplay behind charge density waves”, *Proc. SPIE 11346, Advances in Ultrafast Condensed Phase Physics II*, 113460D
4. H. Hedayat, C. J. Sayers, A. Ceraso, J. van Wezel, S. R. Clark, C. Dallera, G. Cerullo, E. Da Como and E. Carpene, “Investigation of the Non-equilibrium State of Strongly Correlated Materials by Complementary Ultrafast Spectroscopy Technique”, *New Journal of Physics* **23** (2021) 033025
5. A. Ceraso, S. Mou, A. Rubano and D. Paparo, “Coherent THz Hyper-Raman: Spectroscopy and Application in THz Detection”, *Materials* **2019**, 12(23), 3870